Majorana zero modes in condensed matter

theoretical and numerical study in one and two dimensional systems

MSc. Alejandro Garrido Hidalgo

Supervisor: Dr. Pedro Orellana Dinamarca
Dr. Alex Matos-Abiague

This thesis is submitted for the degree of
Doctor of Philosophy

May 2025

I would like to dedicate this thesis to science.

Abstract

The search for conclusive and robust Majorana Zero Modes (MZM) signatures has been of great experimental and theoretical interest due to its potential quantum computing applications. This thesis theoretically furthers this search with three investigations:

In the first work we study a system formed by a Double Quantum Dot (DQD) structure coupled to two normal leads, while each QD is independently connected to a Topological Superconducting Nanowire (TSCN) hosting MZMs at its ends. We focus on the linear conductance through the DQD, the QD's density of states, and the MZMs spectral functions, which are calculated employing the Green's functions (GFs) formalism. We focus in identifying signatures of quantum interference phenomena, emergence of bound states in the continuum (BICs), MZMs leakage into the QDs-BICs, and the interplay between MZM and BIC, by direct control of the magnetic flux over all the bound states of our setup. Our results show that both MZMs and BICs appear in high-symmetry configurations, i.e., depending on the QD-MZM coupling strength and the length of the TSCN. Also, we find a transport suppression anomaly in the linear conductance as a function of the magnetic flux. This phenomenon appears for the same symmetric configurations mentioned above. We also find that both the MZMs leaking into the QDs and the BICs can be controlled by the magnetic flux, suggesting that this external parameter will suffice for manipulating the above states.

In the second work, we examine the thermoelectric characteristics of a system consisting of two topological superconducting nanowires, each exhibiting Majorana zero modes at their ends, connected to leads within an interferometer configuration. By employing Green's function formalism, we derive the spectral properties and transport coefficients. Our findings indicate that bound states in the continuum (BICs) manifest in symmetric setups, influenced by the length of the wires and coupling parameters. Deviations of the magnetic flux from specific values transform BICs into quasi-BICs with finite width, resulting in conductance antiresonances. The existence and interplay of Majorana zero modes enhances the thermoelectric performance in asymmetric configurations. Modulating the magnetic flux induces transitions from BICs to quasi-BICs and significantly enhances the Seebeck coefficient and figure of merit, thereby suggesting a strategy for optimizing thermoelectric efficiency in systems based on Majorana zero modes.

In the third work, we study the formation and properties of edge-like and end-like Majorana States (MSs) in proximitized planar Josephson Junctions and characterize them by introducing a quantity (here referred to as the topological gap character) that contains information about the topological charge, topological gap, and the localization nature of the zero-energy states. The norm of the topological gap character determines the size of the topological gap relative to the proximity-induced superconducting gap, and its sign indicates whether the system is in a TS state with *edge*-like (positive sign) or *end*-like (negative sign) MSs. We analyze how the localization character of MSs depends on relevant system parameters such as the magnetic field strength and direction, the superconducting phase difference across the junction, the spin orbit couplig strength, and the junction crystallographic orientation. Moreover, our study reveals the possibility of inducing transitions from end-like to edge-like MSs (and vice versa) by tuning the magnetic field strength and/or the superconducting phase difference. Our findings can be used as a guide for achieving optimal MZM protection and localization when engineering TS in planar JJs and could be particularly relevant for implementing braiding operations without the need for complex non-colinear junctions.

Acknowledgements

I would like to express my deepest gratitude to all the people who have been part of this journey. Each interaction, lesson, and shared moment has contributed to my growth in invaluable ways. Whether through support, challenge, or simple kindness, everyone I've encountered has left a meaningful imprint on my life. Thank you.

Table of contents

List of figures

Chapter 1

Introduction

Topological superconductivity (TS) is a unique phase of matter distinguished by non-trivial topological invariants and the emergence of gapless, protected states at its boundaries. These states, known as Majorana zero modes (MZMs) or Majorana bound states (MBSs), have attracted intense interest due to their potential applications in fault-tolerant quantum computing and their exotic non-Abelian statistics [9–12, 5]. While MZMs were initially predicted to arise in intrinsic p-wave superconductors [13], the absence of confirmed p-wave materials has driven efforts to engineer synthetic platforms. By combining conventional s-wave superconductors with materials exhibiting strong spin-orbit coupling (SOC)—such as semiconductors or topological insulators—researchers can induce effective p-wave pairing through the proximity effect, then the time-reversal symmetry is broken by an external magnetic field.

The theoretical model proposed by Kitaev predicts that unpaired Majorana zero modes (MZMs) can localize at the ends of a spinless p-wave superconducting nanowire, with their coupling strength decaying exponentially as the wire's length increases [9]. This inspired further studies on proximitized nanowires, where a topological phase transition occurs upon tuning the Zeeman energy or chemical potential [14, 15, 10]. This transition is characterized by the closing and reopening of the superconducting gap, after which MZMs are expected to emerge at the wire ends (Fig. 1.2(a)).

The first experimental realization of this system was reported by Mourik et al. [2]. However, achieving reproducible MZMs in 1D systems remains challenging due to the stringent parameter control required, with only a few experimental groups achieving reproducible results. The experiments carried out by Aghaee et al. substantiated these findings in heterostructures, affirming thus the presence of topological superconductivity and MZMs [16]. Additionally, braiding MZMs—essential for quantum gate operations—requires complex nanowire networks [17–19], introducing fabrication hurdles. However, recent advances in

quantum computing exploit the principles of Majorana physics; notably, the Majorana-1 processor incorporates MZMs, offering a viable research pathway toward scalable quantum architectures [20].

To overcome these challenges, recent research has shifted toward planar Josephson junctions (JJs) [21, 22, 14, 3, 23–27], which offer broader parameter ranges for accessing the TS phase. These JJs typically consist of a semiconductor 2D electron gas (2DEG) with strong SOC (e.g., InAs or HgTe), partially covered by s-wave superconducting leads (e.g., Nb or Al). The uncovered region forms a normal (N) region between superconducting (S) electrodes, creating an S-N-S structure (Fig. 1.2(c)). Unlike nanowires, JJs leverage the superconducting phase difference as an additional tuning parameter, enabling more robust stabilization of MZMs [21, 22, 14]. Their geometric flexibility (e.g., T-, X-, or Y-junctions) also allows for implementing braiding protocols and multi-Majorana systems [28, 29]. Recent experiments have observed MZM-like signatures localized at the ends of the N region, though some studies report edge-localized modes extending along the entire junction, a phenomenon explored further in Chapter 4.

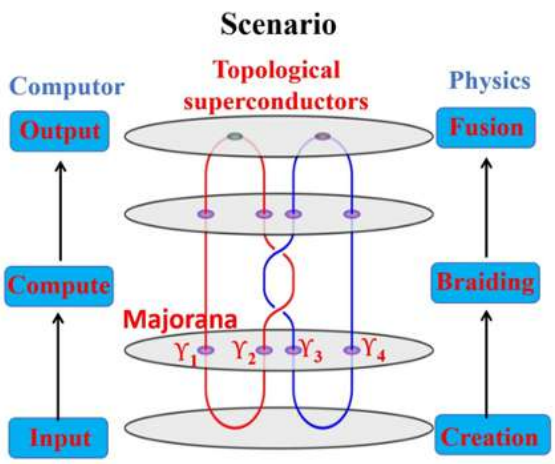

Fig. 1.1 Braiding of Majorana fermions and their physical realization: In topological quantum computing, particles are created in a $(2+1)$-dimensional space, exchanged so that their world lines form a braid, and then pairwise fused. These operations involving Majorana fermions can be encoded in the topology of their braids, enabling them to be performed in a protected way. (image from reference[1])

1.1 Experimental evidence of Majorana Zero Modes

The search for Majorana zero modes (MZM) is motivated primarily by their potential to enable fault-tolerant quantum computing. Current quantum computers face a critical

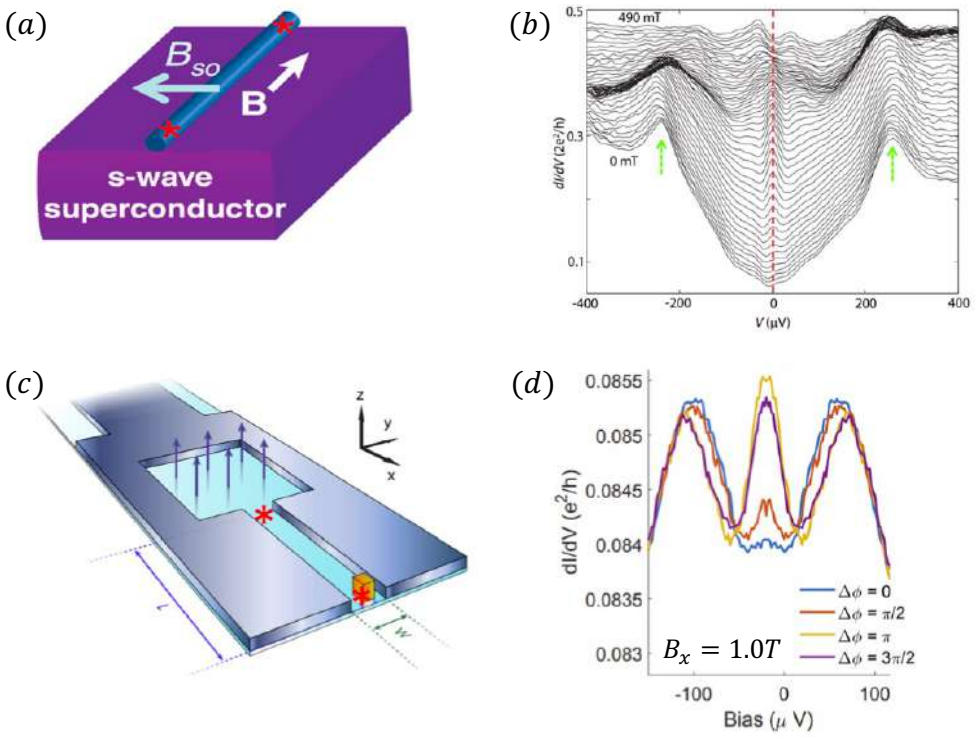

Fig. 1.2 (a) Schematic of a traditional 1D nanowire setup for topological superconductivity. (b) Experimental measurements of the conductance as a function of voltage bias along a semiconductor wire setup for multiple magnetic field strengths. The zero bias conductance peak (ZBCP) appears at 0 μV (red dashed line) as the magnetic field strength increases. (c) Schematic of a planar Josephson junction setup for creation and detection of topological superconductivity. The grey-metallic upper layer denotes a s-wave Al superconductor, and the bottom blue layer denotes a HgTe 2DEG. The red asterisks represent the localization areas of MZM. The arrows penetrating the superconducting loop denotes an external magnetic flux used to fix the phase difference between left and right superconducting leads. The yellow contact is used to probe the zero-bias conductance signature of the MZM localized underneath. (d) Differential conductance curves as a function of the bias voltage on the tunnel probe (see (c)) for four representative values of the phase difference. (Images (a) and (b) taken from [2], (c) and (d) taken from [3])

challenge: their logical qubits are highly susceptible to errors from external perturbations, necessitating extensive error-correcting qubits in order to confidently run quantum algorithms. MZMs offer a promising solution due to their topological protection against local disturbances and their suitability for logic gates via braiding operations. Crucially, the topological nature of MZMs ensures that quantum gates depend only on the braiding topology—not on specific trajectories—making them inherently robust against errors. Additionally, MZM fusion could facilitate qubit state reading/detection [See Fig. 1.1, from reference [1]]. Beyond practical applications, definitive experimental observation of MZMs' non-Abelian statistics would mark a landmark achievement in physics, as no quasiparticle with such properties has yet been conclusively demonstrated.

The first experimental evidence of topological superconductivity was observed in a proximitized nanowire [Fig. 1.2(a)], where a zero-bias conductance peak (ZBCP) was measured (See Fig. 1.2(b), from reference [2]). While ZBCPs are theoretically linked to zero-energy states (potentially MZMs), they are not unambiguous proof: phenomena like the Kondo effect or Andreev bound states can mimic this signature. Moreover, Majorana-induced ZBCPs are predicted to quantize at $2e^2/h$ (at zero temperature), yet measured peaks consistently fall short of this value. The ZBCP has also been measured in planar JJs using the experimental setup shown in Fig. 1.2(c), where the JJ is incorporated in a closed loop threaded by a magnetic flux, which fixes the superconducting phase across the junction. However, the detected ZBCP amplitude was also found to be well below the predicted universal conductance value, as shown in Fig. 1.2(d). Therefore, the measurements of a ZBCP as evidence of the existence of topological superconductivity are far from being conclusive. However, the difference in ZBPCs observed in Fig. 1.2(d) for the cases $\Delta\phi = \pi$ and $\Delta\phi = 0$, can be explained by the formation of two distinct types of MZMs: end-like and edge-like, respectively. The end-like MZM is predominantly localized at opposite ends of the junction with short localization lengths (red asterisk), while the edge-like MZM are localized at the ends of the junction but extend along the edges perpendicular to the junction. These results are thoroughly analyzed and reported in Chapter 4.

An alternative method to identify MZMs involves using thermoelectric measurements, which offer distinct advantages by exploring their unique transport signatures. Conventional thermoelectric measurement techniques, developed in the early 1990s [30, 31], have developed into potent tools for detecting chargeless MZMs. These techniques can disclose MZM signatures through thermal conductance [21, 32], voltage thermopower [33–35], or the breach of the Wiedemann-Franz law [36–38], providing complementary evidence beyond zero-bias anomalies.

1.2 Where is the Topology?

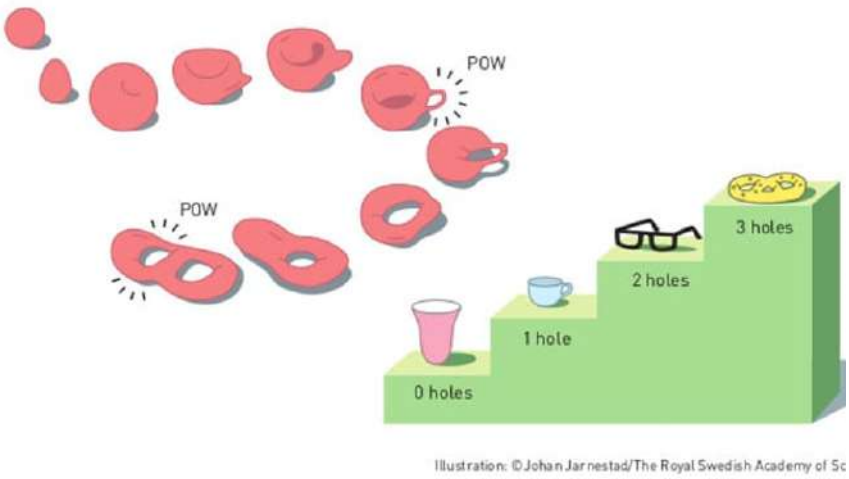

Fig. 1.3 Change in topology of an object when a hole is created (left); distinction between different topological objects characterized by number of holes (i.e., genus) (right). Topology is a branch of mathematics that describes properties that only change step-wise, like the number of holes in the above objects. Topology describes the properties that remain invariant when an object is stretched, twisted or deformed, but not if it is torn apart. Imagine a donut made of clay: by stretching and bending, you can morph it into a coffee cup (keeping the hole as the handle), proving they're topologically equivalent. Topological objects can thus contain one hole, or two, or three, or four, but this number has to be an integer. This is particularly useful for characterizing global invariants in condensed matter systems—such as the quantized electrical conductance in the quantum Hall effect, which changes only in integer multiples of the quantum conductance. (Image taken from [4])

To a mathematician, topology is the study of geometric objects under continuous transformations, focusing on properties that remain invariant during such deformations. For instance, Fig. 1.3 illustrates a continuous transformation of a 3D coffee cup into a donut [4]. Throughout this process, the number of holes (the genus g) stays constant, a key topological invariant for classifying shapes.

This invariance is quantified by the Gauss-Bonnet theorem, which links local geometry to global topology. For a closed 2D surface S, the theorem states:

$$\int_S K\,dA = 2\pi\,\chi(S), \quad \text{where } \chi(S) = 2-2g. \tag{1.1}$$

Here, K is the Gaussian curvature (positive for sphere-like regions, negative for saddle-like ones), and $\chi(S)$ is the Euler characteristic, determined by the genus g. For example:

- A coffee cup and donut (both $g = 1$) have $\chi = 0$, requiring their total curvature to vanish (balancing "hills" and "valleys").
- A sphere ($g = 0$) has $\chi = 2$, forcing $\int_S K\,dA = 4\pi$.

The theorem reveals why topology constrains geometry: continuous deformations preserve g and χ, fixing the "curvature budget" of the surface.

In condensed matter physics, topology classifies quantum phases based on global invariants that persist under smooth deformations of the system. These invariants—such as the Chern number in quantum Hall effects [39] or the $\mathbb{Z}_2$ index in topological insulators—arise from the wavefunction's structure (e.g., Berry curvature in momentum space) and dictate robust physical properties. For instance, 3D topological insulators exhibit conducting surface states immune to disorder, while magnetic skyrmions are stabilized by their winding number. Mathematically, topology distinguishes phases by equivalence classes of Hamiltonians, akin to how a donut and coffee cup share the same genus. This framework reveals profound connections between geometry, symmetry, and emergent quantum phenomena. The robustness of topologically protected states stems from the discrete nature of topological invariants. Since these invariants cannot change continuously, smooth local perturbations cannot destroy or remove such states, doing so would require altering the invariant discontinuously, which is inherently forbidden.

In this thesis, the first two works involve nanowires in their topological phase (Chapter 2 and Chapter 3), while the third work uses the calculation of topological invariants to describe the trivial or topological phase of the system (Chapter 4).

Chapter 2

MZMs and BICs in a DQD interferometer

In systems with quantum dots (QDs) connected to topological superconducting nanowires (TSCNs), there are usually more than one electronic path, which allows exploiting the quantum interference effects as a tool to predict the consequences of the presence of Majorana zero modes (MZMs) at the edges of the TSCN. In particular, we model a system where each quantum dot is embedded in one of the arms of the interferometer, using the Aharonov-Bohm phase (due to the existing magnetic flux across the interferometer) as a parameter to control emerging states in the different coupling regimes.

2.1 Kitaev chain

The most widely used model for TSCN is the Kitaev chain [9]. To understand this model and the distinction between its two phases (trivial and non-trivial topological) we begin with the Hamiltonian of a one-dimensional spinless lattice featuring superconducting pairing Δ,

$$H = \sum_j \left[\mu c_j^\dagger c_j - \frac{1}{2} \left(t c_j^\dagger c_{j+1} - \Delta e^{i\phi_{SC}} c_j c_{j+1} + h.c. \right) \right], \tag{2.1}$$

where $c_j^\dagger (c_j)$ is the creation (anihilation) fermionic operator in the j-th site of the chain, μ is the chemical potential, t is the coupling between sites, Δ is the superconducting pairing energy, and ϕ_{SC} is the superconducting phase. We can replace the fermionic operators with Majorana operators by the following definition,

$$\gamma_{2j-1} = e^{i\phi_{SC}/2} c_j + e^{-i\phi_{SC}} c_j^\dagger, \tag{2.2}$$

$$\gamma_{2j} = -ie^{i\phi_{SC}/2} c_j + ie^{-i\phi_{SC}} c_j^\dagger, \tag{2.3}$$

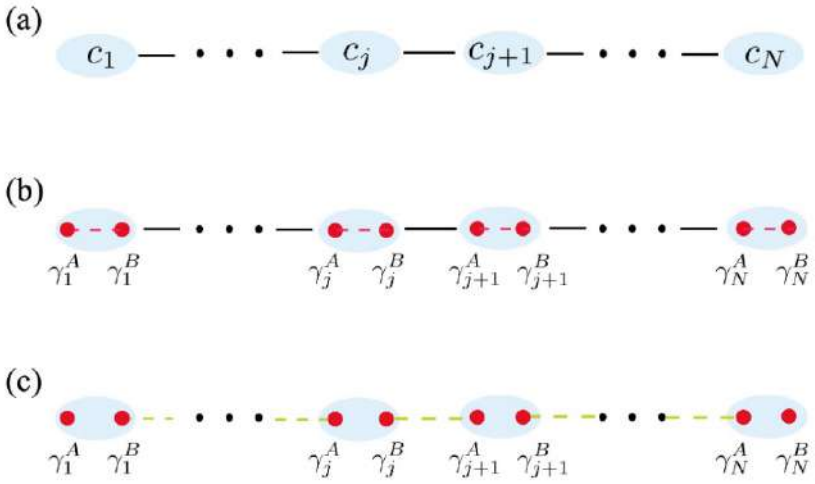

Fig. 2.1 Kitaev chain. a) One-dimensional chain of spinless fermions with tight-binding parameters as described by Eq. 2.1. b) Trivial phase of the Kitaev chain: in the Majorana representation of Eq. 2.5, the Majoranas on each site are coupled forming a standard fermion. c) Non-trivial phase: Majoranas on each site are decoupled while Majoranas on adjacent sites become coupled. This leaves two unpaired Majoranas at the ends of the chain. (Image taken from [5])

where satisfies both $\gamma_n = \gamma_n^\dagger$ and $\{\gamma_n, \gamma_{n'}\} = 2\delta_{n,n'}$. We can interpret that each fermionic operator c_j is expressed by two operators γ_{2j-1} and γ_{2j}, as schematically indicated in Fig. 2.1(b). The Hamiltonian in Majorana representation is written as,

$$H = -\frac{i}{2}\sum_j \left[\mu\gamma_{2j}\gamma_{2j-1} + \frac{1}{2}(t-\Delta)\gamma_{2j-1}\gamma_{2j+2} - \frac{1}{2}(t+\Delta)\gamma_{2j}\gamma_{2j+1}\right]. \tag{2.4}$$

We can distinguish two phases from the above Hamiltonian [see Fig. 2.1], the trivial phase, with $\mu \neq 0$ and $t = \Delta = 0$. In this case, the Hamiltonian reduces to,

$$H = -\frac{i\mu}{2}\sum_j \gamma_{2j}\gamma_{2j-1}. \tag{2.5}$$

where the Majoranas on each j-site are coupled forming a standard fermion. On the other hand, we have the non-trivial topological phase, with $t = |\Delta \neq 0$ and $\mu = 0$. For this case, the Hamiltonian reduces to

$$H = \frac{it}{2}\sum_j \gamma_{2j}\gamma_{2j+1}. \tag{2.6}$$

where Majoranas on each site are decoupled while Majoranas on adjacent sites become coupled, this leaves two unpaired Majoranas at the ends of the chain [γ_1^A and γ_N^B in Fig.

2.1(c)], and since they do not appear in the Hamiltonian, then they correspond to zero energy states [5].

This last case demonstrates the existence of Majorana bound states localized at the ends of the chain (now denoted as γ_L and γ_R). Kitaev further developed an effective model in which these edge states interact through a coupling parameter of the form,

$$H = i\varepsilon_M \gamma_L \gamma_R, \tag{2.7}$$

where $\varepsilon_M \sim e^{-L/l_0}$ with L the length of the chain and l_0 the superconducting characteristic length.

2.2 Bound states in the continuum

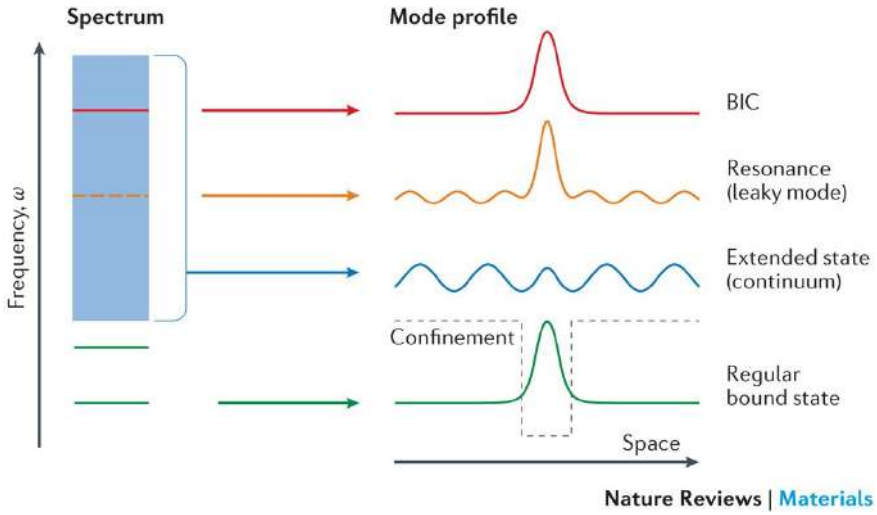

Fig. 2.2 In an open system, the frequency spectrum consists of a continuum or several continua of spatially extended states (shown in blue) and discrete levels of bound states (shown in green) that carry no outgoing flux. The purple dashed line illustrates the structure that provides confinement. States inside the continuous spectrum typically couple to the extended waves and radiate, becoming leaky resonances (shown in orange). BICs (shown in red) are special states that lie inside the continuum but remain localized with no radiation. [6]

Bound states in the continuum (BICs) were first theorized by von Neumann and Wigner[40]. They demonstrated that certain oscillatory potentials can sustain bound states embedded within the continuum spectrum, i.e., do not decay even if their energy levels are within the range of the continuum states [6], as we can apreciate in Fig. 2.2. The BICs, have been receiving great interest in photonic systems. Furthermore, given the analogous interference

phenomena in electronic and photonic systems, the presence of BICs may naturally extend to electronic systems [6, 41, 42].

These states can be detected through the density of states, where they manifest as extremely narrow resonances (approaching zero width) effectively resembling Dirac delta (δ) functions.

2.3 Interferometer and quantum dots

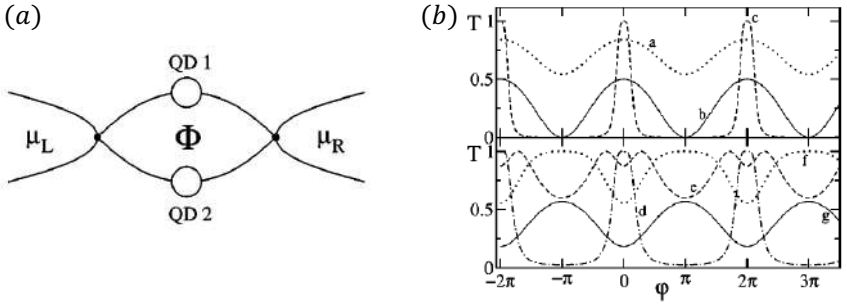

Fig. 2.3 (a) Double-dot Aharonov-Bohm interferometer. (b) Transmission between leads as a function of magnetic flux. There are signatures of a flux-dependent level attraction and an anomaly of suppressed transport. The form of AB oscillations in different regions of the parameter space, indicate the evolution of sharp peaks near the anomaly of suppressed transport and a maximum- to-minimum transition of the AB signal around $\varphi = \pi$. Regimes where constructive interference through identical dots yields a transmission that is 1, 2, or 4 times as large as that through a single quantum dot were identified. [7]

The electronic transport through quantum dots (QDs) structures has been an active research field during the past decades [43–48]. QDs are nanostructures with quantized energy levels due to the confinement of electrons, so they are usually called artificial atoms [43]. Additionally, electrons tunneling through QDs show a high coherence preservation, demonstrated in several phenomena such as the subtle Kondo effect in QD connected to leads [49–51], the Aharonov-Bohm (AB) oscillations in closed interferometers [52, 7], and Fano resonances in systems with multiple channels [53, 54, 43, 44, 52, 50, 55], among others.

In a previous work, a double QD (DQD) interferometer has shown an anomaly of suppressed transport and signatures of a flux-dependent level attraction [see Fig. 2.3], which can be manipulated by an applied magnetic flux and gate voltages [7]. Moreover, when a TSCN is coupled to the DQD, the linear conductance shows MZM signatures at zero energy while inducing the Fano effect [56].

2.4 Outline

In the following paper we study a system formed by a DQD structure coupled to two normal leads, while each QD is independently connected to a TSCN hosting MZMs at its ends. We focus on the linear conductance through the DQD, the QD's density of states, and the MZMs spectral functions, which are calculated employing the Green's functions (GFs) formalism. We focus on identifying signatures of quantum interference phenomena, MZMs leakage into the QDs-BICs, and the interplay between MZM and BIC, by directly controlling the magnetic flux over all the bound states.

Eur. Phys. J. Plus (2023) 138:663
https://doi.org/10.1140/epjp/s13360-023-04271-z

THE EUROPEAN PHYSICAL JOURNAL PLUS

Regular Article

Bound states in the continuum and Majorana zero modes in a double quantum dot interferometer: Ghost-Fano Majorana effect

A. P. Garrido[1,a], **D. Zambrano**[1], **J. P. Ramos-Andrade**[2], **P. A. Orellana**[1]

[1] Departamento de Física, Universidad Técnica Federico Santa María, Av. España 1680, Casilla 110V, Valparaiso, Chile
[2] Departamento de Física, Universidad de Antofagasta, Av. Angamos 601, Casilla 170, Antofagasta, Chile

Received: 28 January 2023 / Accepted: 7 July 2023

Abstract We investigate the transport properties through a nanostructure composed of parallel double quantum dots coupled to two normal contacts. Additionally, each quantum dot is connected to a topological superconducting nanowire, hosting Majorana zero modes at its ends. A magnetic flux threading across the area enclosed by the interferometer is considered. First, we investigate the physical quantities of the system employing Green's function formalism. We find that the emergence of bound states appears in symmetric configurations of topological superconducting nanowires, i.e., depending on their lengths and coupling energies to the quantum dots. Also, we find a transport suppression anomaly as a function of the magnetic flux in the same symmetric configurations mentioned above. Besides, we find that the magnetic flux controls both the projection of Majorana zero modes and of the bound states in the continuum into the density of states and the linear conductance, suggesting that only by switching this parameter can we manipulate both bound states.

1 Introduction

In recent years, the study of topological superconductor nanowires (TSCNs) has received a great deal of attention in condensed matter physics due to their potential for technological applications in quantum computing [1–6]. In this context, the existence of exotic fermionic quasiparticles has been predicted as quasiparticles that would be their own anti-quasiparticles [7–9], as the ones appearing localized in topological superconducting systems. Due to their resemblance with Majorana fermions they are called Majorana zero modes (MZMs).

MZMs satisfy non-Abelian statistics and they can be manipulated by braiding operations [10, 11], making them exceptional candidates for quantum computation implementations [1–3, 6, 10, 12–14]. Among others, MZMs systems are predicted to be found at the ends of a TSCN, composed of a semiconductor-superconductor nanowire with strong spin-orbit interaction in the presence of a magnetic field. This system can be seen as a setup of a Kitaev chain [1, 12, 15], in which the coupling between the two MZMs located at the wire's opposite ends decays exponentially with the wire's length [6], allowing to build of a qubit which is topologically protected from decoherence by local perturbations [6, 10, 12, 16–18].

The first physical realization of this system was achieved by Mourik and collaborators, announcing zero-bias anomalies in the conductance as a signature of the MZMs presence [19]. Later, many systems have been proposed [20–33], and several experiments based on zero-bias anomalies in transport properties through source-drain leads have been performed [19, 34–40]. But these anomalies are not always a reliable evidence of MZMs, leading to the necessity of devising custom-made experimental protocols that allow e.g. performing simultaneous tunneling and Coulomb blockade spectroscopy measurements within the same device, in order to rule out MZMs detection ambiguities [41].

On the other hand, the so-called bound states in the continuum (BICs) do not decay even if their energy levels are within the range of the continuum states [42]. The BICs, predicted by von Neumann and Wigner [43], have been receiving great interest in photonic systems. Moreover, due to the typical interference phenomena analogy between electronic and photonic systems, the inherent possibility of BICs presence in electronic systems arises [42, 44, 45]. In this context, the electronic transport through quantum dots (QDs) structures has been an active research field during the past decades [46–51]. QDs are nanostructures with quantized energy levels due to the confinement of electrons, so they are usually called artificial atoms [46]. Additionally, electrons tunneling through QDs show a high coherence preservation, demonstrated in several phenomena such as the subtle Kondo effect in QD connected to leads [35, 52, 53], the Aharonov-Bohm (AB) oscillations in closed interferometers [54, 55], and Fano resonances in systems with multiple channels [46, 47, 52, 54, 56–58], among others.

[a] e-mail: alejandro.garridoh@usm.cl (corresponding author)

In the past years, a wide range of research has been done regarding the effects of quantum interference in several configurations of the components previously explained: parallel, series, and T-shaped. In the systems of hybridized QD-TSCN, there is usually more than one electron transport path, and quantum interference effects are an efficient way to detect the existence of the MZMs formed at the ends of the TSCN [59, 60]. For instance, in a non-interacting QD-leads system with a side coupled TSCN, Liu and Baranger established a particular signature of the presence of MZMs, which is a half-integer conductance at zero-energy [61]. Later, it was shown that this zero-bias anomaly is due to MZM leaking into the QD [62], and it is robust against changes in the QD energy level, which was shortly after experimentally verified [63]. Aditionally, in QD-MZMs systems, where the interplay between MZM-BICs can take place, a theoretical encryption setup based on BICs [64] and Majorana fermion qubits readout technology [65] have been proposed.

In previous work, a double QD (DQD) interferometer has shown an anomaly of suppressed transport and signatures of a flux-dependent level attraction, which can be manipulated by an applied magnetic flux and gate voltages [55]. Moreover, when a TSCN is coupled to the DQD, the linear conductance shows MZM signatures at zero energy and then inducing the Fano effect [60].

Within this context, in the present work we study a system formed by a DQD structure coupled to two normal leads, while each QD is independently connected to a TSCN hosting MZMs at its ends. We focus on the linear conductance through the DQD, the QD's density of states, and the MZMs spectral functions, which are calculated employing the Green's functions (GFs) formalism. We focus in identifying signatures of quantum interference phenomena, MZMs leakage into the QDs-BICs, and the interplay between MZM and BIC, by direct control of the magnetic flux over all the bound states of our setup. Our results show that both MZMs and BICs appear in high-symmetry configurations, i.e., depending on the QD-MZM coupling strength and the length of the TSCN. Also, we find a transport suppression anomaly in the linear conductance as a function of the magnetic flux. This phenomenon appears for the same symmetric configurations mentioned above. We also find that both the MZMs leaking into the QDs and the BICs can be controlled by the magnetic flux, suggesting that this external parameter will suffice for manipulating the above states.

This paper is organized as follows: Sect. 2 presents the model and method used to obtain quantities of interest; Sect. 3 shows the results and discussions, and the concluding remarks are presented in Sect. 4.

2 Model and method

We consider an interferometer configuration of the DQD, where each QD is connected to the two normal leads S and D, and independently side-coupled to one of the TSCNs hosting MZMs at both ends, as we show schematically in the Fig. 1. We model the system through an effective low-energy Hamiltonian in the following form

$$H = H_{\text{dots}} + H_{\text{leads}} + H_{\text{dots-leads}} + H_{\text{M}} + H_{\text{dots-M}}, \tag{1}$$

where the first three terms on the right-hand side correspond to the regular electronic contributions, given by

$$H_{\text{dot}} = \sum_{j=1,2} \varepsilon_j d_j^\dagger d_j \,, \tag{2}$$

$$H_{\text{leads}} = \sum_{\alpha,\mathbf{k}} \varepsilon_{\alpha,\mathbf{k}} a_{\alpha,\mathbf{k}}^\dagger a_{\alpha,\mathbf{k}} \,, \tag{3}$$

$$H_{\text{dots-leads}} = \sum_{\alpha,\mathbf{k}} \sum_{j=1,2} (t_{\alpha,\mathbf{k},j}(\varphi_{\alpha,j}) a_{\alpha,\mathbf{k}}^\dagger d_j + \text{h.c.}) \,, \tag{4}$$

where $d_j^\dagger (d_j)$ is the electron's creation (annihilation) operator in the j-th QD, with single energy level ε_j. The operator $a_{\alpha,\mathbf{k}}^\dagger (a_{\alpha,\mathbf{k}})$ is the electron creation (annihilation) operator with momentum $\mathbf{k}$, and energy $\varepsilon_{\alpha,\mathbf{k}}$ in the lead $\alpha = S,\ D$. The parameter $t_{\alpha,\mathbf{k},j}(\varphi_{\alpha,j}) = t_{\alpha,\mathbf{k},j}^{(0)} \exp[i\varphi_{\alpha,j}]$ describes the QD-lead tunnel matrix element, where an Aharonov-Bohm (AB) phase is included to model the

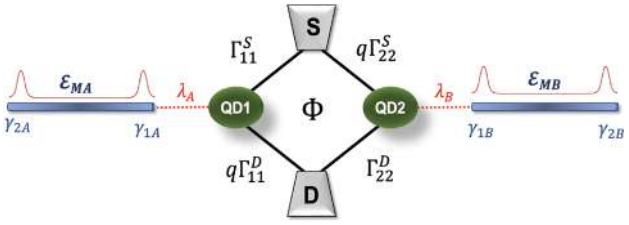

Fig. 1 Schematic view of the system under study: TSCN-DQD-TSCN. Each QD (green) is coupled to a TSCN (blue tones). The TSCN $A(B)$ is connected to the QD1(2) and hosts two MZMs, $\gamma_{1,A(B)}$ and $\gamma_{2,A(B)}$, at its ends (light blue). The DQD is coupled to two normal leads, labeled as S and D (solid gray), and an external magnetic flux Φ across the interferometer is considered. The Γ parameters are the couplings among the system's components and q is an asymmetry parameter, as later explained in the main text

magnetic flux Φ across the interferometer [55]. We choose a symmetric gauge such that $\varphi_{D,1} = -\varphi_{D,2} = -\varphi_{S,1} = \varphi_{S,2} = \phi/4$, with $\phi = 2\pi\Phi/\Phi_0$ and $\Phi_0 = h/e$ is the quantum flux, where h is the Planck's constant and e the electron's charge.

The last two terms in the Hamiltonian presented in Eq. (1) are MZMs terms, specifically MZM-MZM and MZM-QD couplings, given by

$$H_{\mathrm{M}} = \sum_{\beta} i\varepsilon_{M,\beta}\gamma_{1,\beta}\gamma_{2,\beta}, \tag{5}$$

$$H_{\text{dot-M}} = (\lambda_A d_1 - \lambda_A^* d_1^\dagger)\gamma_{1,A} + (\lambda_B d_2 - \lambda_B^* d_2^\dagger)\gamma_{1,B}, \tag{6}$$

where $\gamma_{j,\beta}$ denotes the MZM operator (with $\beta = A,\ B$), and satisfies both $\gamma_{j,\beta} = \left[\gamma_{j,\beta}\right]^\dagger$, and $\{\gamma_{j,\beta},\ \gamma_{j',\beta'}\} = \delta_{j,j'}\delta_{\beta,\beta'}$. Besides, $\lambda_{A(B)}$ is the tunneling coupling between $\gamma_{1,A(B)}$ and the $\mathrm{QD}_{1(2)}$, and $\varepsilon_{M,\beta} \propto \exp(-L_\beta/\zeta)$ is the coupling amplitude between two MZMs in the same TSCN, where L_β corresponds to the wire's length and ζ denotes the superconducting coherence length. We can evaluate the electronic transport by using a transformation as follows: by writing each MZM operator as a superposition of regular fermionic operators f_β in the form

$$\gamma_{1,\beta} = \frac{1}{\sqrt{2}}(f_\beta + f_\beta^\dagger), \tag{7a}$$

$$\gamma_{2,\beta} = -\frac{i}{\sqrt{2}}(f_\beta - f_\beta^\dagger), \tag{7b}$$

satisfying the anticommutation relations $\{f_\beta,\ f_{\beta'}\} = \{f_\beta^\dagger,\ f_{\beta'}^\dagger\} = 0$, and $\{f_\beta,\ f_{\beta'}^\dagger\} = \delta_{\beta,\beta'}$. Accordingly, the Eqs. (5) and (6) transform to

$$H_{\mathrm{M}} = \sum_{S} \varepsilon_{M,\beta}\left(f_\beta^\dagger f_\beta - \frac{1}{2}\right), \tag{8}$$

$$\begin{aligned} H_{\text{dot-M}} = &\left(\frac{1}{\sqrt{2}}\right)(\lambda_A d_1 - \lambda_A^* d_1^\dagger)(f_A + f_A^\dagger) \\ &+ \left(\frac{1}{\sqrt{2}}\right)(\lambda_B d_2 - \lambda_B^* d_2^\dagger)(f_B + f_B^\dagger). \end{aligned} \tag{9}$$

The Hamiltonian described above is spinless since only electrons with one spin projection will couple to the MZMs [66]. At low temperatures, characteristic of superconducting systems, the linear electronic conductance $\mathcal{G}$ is obtained through the transmission probability $T(\omega)$. We fixed the temperature at $\mathcal{T} = 0$, so the relation between both quantities is directly given by the Landauer formula $\mathcal{G} = (e^2/h)T(\omega = \varepsilon_{\mathrm{F}})$ [67, 68], where ε_{F} is the Fermi level's energy. The transmission probability is calculated from the expression

$$T(\omega) = \mathrm{Tr}\{\hat{G}^a(\omega)\hat{\Gamma}^D\hat{G}^r(\omega)\hat{\Gamma}^S\}, \tag{10}$$

where $\hat{G}^{a(r)}(\omega)$ is the system advanced (retarded) GF in the energy domain, and $\hat{\Gamma}^{D(S)}$ the line-width function denoting the coupling between the QDs and the leads $D(S)$, and are given by

$$\hat{\Gamma}^\alpha = \begin{pmatrix} 0 & 0 & 0 & 0 & 0 & 0 & 0 & 0 \\ 0 & 0 & 0 & 0 & 0 & 0 & 0 & 0 \\ 0 & 0 & \Gamma_{11}^\alpha & 0 & \Lambda_{12}^\alpha & 0 & 0 & 0 \\ 0 & 0 & 0 & \Gamma_{11}^\alpha & 0 & \Lambda_{12}^\alpha & 0 & 0 \\ 0 & 0 & \Lambda_{21}^\alpha & 0 & \Gamma_{22}^\alpha & 0 & 0 & 0 \\ 0 & 0 & 0 & \Lambda_{21}^\alpha & 0 & \Gamma_{22}^\alpha & 0 & 0 \\ 0 & 0 & 0 & 0 & 0 & 0 & 0 & 0 \\ 0 & 0 & 0 & 0 & 0 & 0 & 0 & 0 \end{pmatrix}, \tag{11}$$

where we have defined $\Lambda_{ij}^\alpha = \sqrt{\Gamma_{ij}^\alpha\Gamma_{ji}^\alpha}$, and $\Gamma_{ij}^\alpha = 2\pi t_{\alpha,\mathbf{k},i}(\varphi_{\alpha i})[t_{\alpha,\mathbf{k},j}(\varphi_{\alpha j})]^*\rho_\alpha$ is the tunnel-coupling strength, with ρ_α being the local density of states in the lead α. The retarded GF satisfies $\hat{G}^r(\omega) = [\hat{G}^a(\omega)]^\dagger$, and will be obtained by means of direct inversion, i. e. $\hat{G}^r(\omega) = (\hat{\omega} - \hat{H})^{-1}$, where $\hat{\omega} = \omega\hat{I}$ is the energy matrix. The procedure is presented qualitatively in the Appendix A.

We also investigate the behavior of the local density of states (LDOS) in each QD, since it is closely related to resonances in the conductance. The LDOS is expressed as

$$\mathrm{LDOS}_{1(2)}(\omega) = -\frac{1}{\pi}\mathrm{Im}\Big[G_{33(55)}^r(\omega) + G_{44(66)}^r(\omega)\Big], \tag{12}$$

where $G^r_{33(44)}\left(G^r_{55(66)}\right)$ are the diagonal terms of the full GF $\hat{G}^r(\omega)$ corresponding to the QD1(QD2). Finally, the spectral functions for the MZMs are given by

$$A_A(\omega) = -2\,\mathrm{Im}\left[\sum_{i,j=1,2} G^r_{ij}(\omega)\right], \tag{13}$$

$$A_B(\omega) = -2\,\mathrm{Im}\left[\sum_{i,j=7,8} G^r_{ij}(\omega)\right], \tag{14}$$

where $G^r_{ij}(\omega)$ in Eqs. (13) and (14) are matrix elements extracted from the full GF $\hat{G}^r(\omega)$, corresponding to the MZMs operators $\gamma_{1,A}$ and $\gamma_{1,B}$, respectively.

Moreover, the complete GF poles are closely related to the eigenvalues of the isolated TSCN-DQD-TSCN (disconnected from leads S and D), and give reliable information about the energy localization of the system's states. The eigenvalues can be written as

$$\begin{aligned} 2[\omega^{\pm}_{1(2)}]^2 = {} & \varepsilon^2_{1(2)} + \varepsilon^2_{M,A(B)} + 2\lambda^2_{A(B)} \\ & \pm \sqrt{(\varepsilon_{1(2)} + \varepsilon_{M,A(B)})^2 + 2\lambda^2_{A(B)}} \\ & \times \sqrt{(\varepsilon_{1(2)} - \varepsilon_{M,A(B)})^2 + 2\lambda^2_{A(B)}}. \end{aligned} \tag{15}$$

For the particular case of $\lambda_{A(B)} = \lambda$, $\varepsilon_{MA(B)} = \varepsilon_M$, and $\varepsilon_{1(2)} = \varepsilon = 0$, the eigenvalues $\omega^{\pm}_{1(2)} = \omega^{\pm}$ are

$$\omega^{-} = 0, \tag{16}$$

$$\omega^{+} = \pm\sqrt{\varepsilon^2_M + 2\lambda^2}, \tag{17}$$

where ω^{-} in the Eq. (16) has quadruple degeneracy and each solution for ω^{+} in the Eq. (17) has double degeneracy.

3 Results

We have considered the wide-band approximation, in which ρ_α has an approximately constant value and then Γ^α_{ii} is energy-independent. Thus, we fixed the line-width function to $\Gamma^S_{11} = \Gamma^D_{22} = \Gamma$, and $\Gamma^D_{12} = \Gamma^S_{12} = \Gamma^D_{21} = \Gamma^S_{21} = \Gamma^D_{11} = \Gamma^S_{22} = q\Gamma$, where q is a dimensionless parameter with $q = 1 (q = 0)$ corresponding to a close(open) system. Besides, the elements Γ^D_{12}, Γ^S_{12}, Γ^D_{21}, and Γ^S_{21} contain the information of the AB phase due to magnetic flux. In the following, all the energy parameters are given in units of Γ. In order to consider realistic parameters with experiments, the values for Γ can be considered from a few to hundreds of meV.

3.1 Without magnetic flux ($\phi = 0$)

First, we consider the case with both TSCNs in the long-wire limit using $\varepsilon_{MA(B)} = 0$, and we fix the QDs' energy levels at $\varepsilon_{1(2)} = 0$. Figure 2 shows the linear conductance $\mathcal{G}$, as a function of the energy ω, for the case when one or both TSCNs are coupled to the DQD with $q = 1$ ($q = 0$) corresponding to a close (open) system. Figure 2a shows a Breit-Wigner resonance centered at $\omega = 0$ for $\lambda_A = 0$ (solid red line) while for $\lambda_A \neq 0$ the linear conductance is composed of a maximum at $\omega = 0$ and two dips located at energies $\omega = \pm\lambda_A$, the latter reaching conductance values $\mathcal{G} \approx e^2/2h$. For this case of parameters, $\omega = \pm\lambda_A$ correspond to the system's eigenenergies. In Fig. 2b, a fixed $\lambda_A = 0.5\Gamma$ is used, and the two QDs are connected in a parallel configuration with asymmetrical left-right coupling such as $0 \leq q \leq 1$. The linear conductance $\mathcal{G}$ amplitude falls progressively to zero when the circuit goes from the close ($q = 1$, solid red line) to the open system ($q = 0$, dashed-dotted purple line). The latter is due to that the transmission coefficient (and then the zero-temperature conductance) is proportional to the line-width function $\hat{\Gamma}^\alpha(q)$, i.e. when q tends to zero, the matrix elements connecting the leads-QDs tend to zero. Notice the location of the antiresonances is independent of the value of q, since they are centered at system's eigenergies, that are obtained regardless q. In Fig. 2c we set the coupling strength $\lambda_A = 0.5\Gamma$ and the second TSCN is connected allowing $0 \leq \lambda_B \leq 0.5\Gamma$. The conductance exhibits two antiresonances close to the conductance value $\mathcal{G} \approx e^2/2h$, which are located at energies $\omega \approx \pm\tilde{\lambda}\sqrt{2}$, with $\tilde{\lambda} = (\lambda_A + \lambda_B)/2$ whenever $\lambda_A \neq \lambda_B$. These vanish for a symmetrical coupling strength $\lambda_A = \lambda_B = 0.5\Gamma$ due to the MZMs hybridization. Furthermore, at zero energy ($\omega = 0$) the conductance goes from its maximum value $\mathcal{G} = e^2/h$ (with one TSCN coupled) to a half-maximum value $\mathcal{G} = e^2/2h$ (when both TSCNs are coupled to the DQD). This robust behavior is independent of the coupling strength λ_A and λ_B, the latter being a MZM signature as was reported for the first time by Liu and Baranger [61]. The antiresonances line-shapes are formed by means of the interference phenomena due to the hybridization between QD's states and MZMs, recently described as the Fano-Majorana effect [40], and it is due to that both electronic paths are no longer equivalent for going from source to drain leads in the cases of non-symmetric couplings between TSCNs and QDs. Without loss of generality, we now set $q = 1$ in what follows.

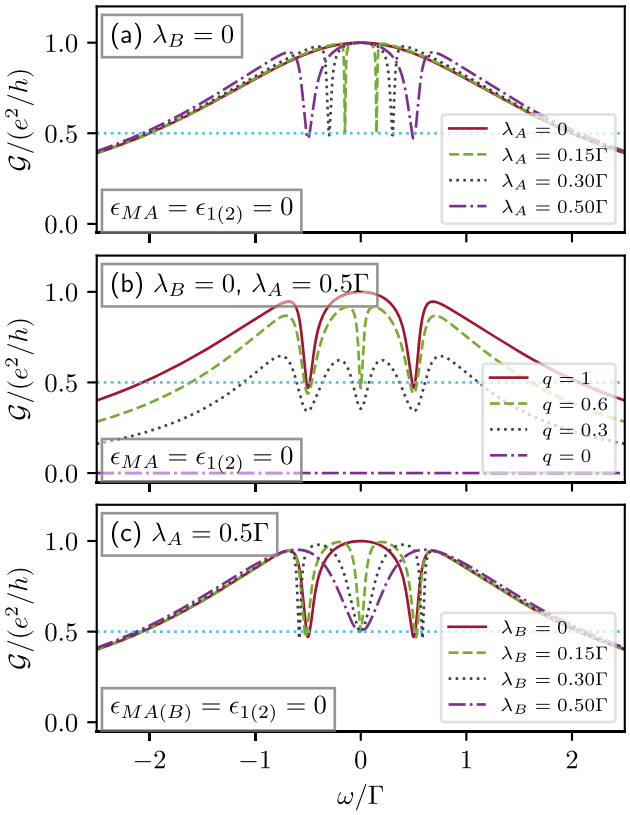

Fig. 2 Linear conductance $\mathcal{G}$ as a function of the energy ω across the DQD in the long-wire limit for both TSCNs ($\varepsilon_{MA(B)} = 0$) with $\varepsilon_{1(2)} = 0$. Panel (a) shows $\mathcal{G}$ with one TSCN coupled ($\lambda_A \neq 0$ and $\lambda_B = 0$) using symmetric coupling between contacts-QD ($q = 1$), where the solid red, dashed green, dotted black and dash-dotted purple lines correspond to $\lambda_A/\Gamma = \{0, 0.15, 0.3, 0.5\}$, respectively. Panel (b) shows $\mathcal{G}$ using fixed $\lambda_A = 0.5\Gamma$ and $\lambda_B = 0$ for the asymmetric coupling between contacts-QD ($0 \leq q \leq 1$). Panel (c) shows $\mathcal{G}$ when both TSCNs are connected ($\lambda_A = 0.5\Gamma$ and $\lambda_B \neq 0$) using $q = 1$, where the solid red, dashed green, dotted black and dash-dotted purple lines correspond to the values $\lambda_B/\Gamma = \{0, 0.15, 0.3, 0.5\}$, respectively

Figure 3 considers both TSCNs out of the long-wire limit (*i.e.* $\varepsilon_{MA(B)} = \varepsilon_M = 0.25\Gamma$) and the coupling strength of each TSCN-QD connection as $\lambda_{A(B)} = \lambda = 0.5\Gamma$. The linear conductance $\mathcal{G}$ as a function of the energy ω, is shown in Fig. 3a–c, and the spectral function $A(\omega)/2$ with the DQD's DOS is shown in Fig. 3b–d. The DOS is obtained by adding both contributions given by Eq. (12). In the case when the QDs' energy levels $\varepsilon_{1(2)} = 0$, the linear conductance $\mathcal{G}$ is composed of a maximum in $\omega = 0$ and two dips located at energies $\omega = \pm\varepsilon_M$ [Fig. 3a]. In Fig. 3b, localized states are observed in the DOS (dashed blue line) in the form of resonances with vanishing width. Since they do not have a projection in $\mathcal{G}$, these states correspond to BICs placed at energies $\omega = \omega^- = 0$ (quadruply degenerate) and $\omega = \omega^+ = \pm\sqrt{\varepsilon_M^2 + 2\lambda^2}$ (each doubly degenerate), accordingly to the eigenvalues described in Eqs. (16) and (17), respectively. Note that the side BICs observed in the DOS are related to the leaking of the lateral bound states present in the spectral function $A(\omega)$. The two symmetric broad resonances placed at energies $\omega = \pm\varepsilon_M$ in $A(\omega)$ hybridize with DQD states, giving place to the dips in the linear conductance. In this case, the spectral function of each MZM, $A_A(\omega)$ and $A_B(\omega)$, are the same and are described by the solid purple line and the dashed-dotted light-purple line.

In Fig. 3c, we introduce asymmetry in the QDs' energy levels in the form $\varepsilon_1 = -\varepsilon_2 = 0.1\Gamma$. The linear conductance $\mathcal{G}$ shows an antiresonance located at $\omega = \omega^- = 0$, and shows two asymmetric Fano-like antiresonances located at the eigenvalues $\omega = \omega^+$, given by the Eq. (15). These states observed in the spectral function and the DOS in Fig. 3d acquire a width, becoming quasi-BICs since they acquire projections on the linear conductance. The vanishing of the lateral Fano-like shapes in both the symmetrical energy and the TSCNs-coupled cases, termed as the so-called Ghost-Fano Majorana effect, is a direct consequence of the bound states uncoupling from the rest of the system, and then there is no contribution to the transmission coefficient [58].

3.1.1 With magnetic flux ($\phi \neq 0$)

We study the electronic transport in the TSCN-DQD-TSCN system in the presence of a magnetic flux across the interferometer (so $\phi \neq 0$). Figure 4 shows the color map of the linear conductance $\mathcal{G}$ as a function of the dimensionless magnetic flux ϕ and the energy ω in top panels. Each bottom panel is a linear conductance $\mathcal{G}$'s horizontal cut (of the corresponding top panel) at fixed values of the magnetic flux $\phi/\pi = \{0, 0.25, 0.5, 1\}$, presented in green, purple, orange, and blue colors, respectively. We use fixed QDs'

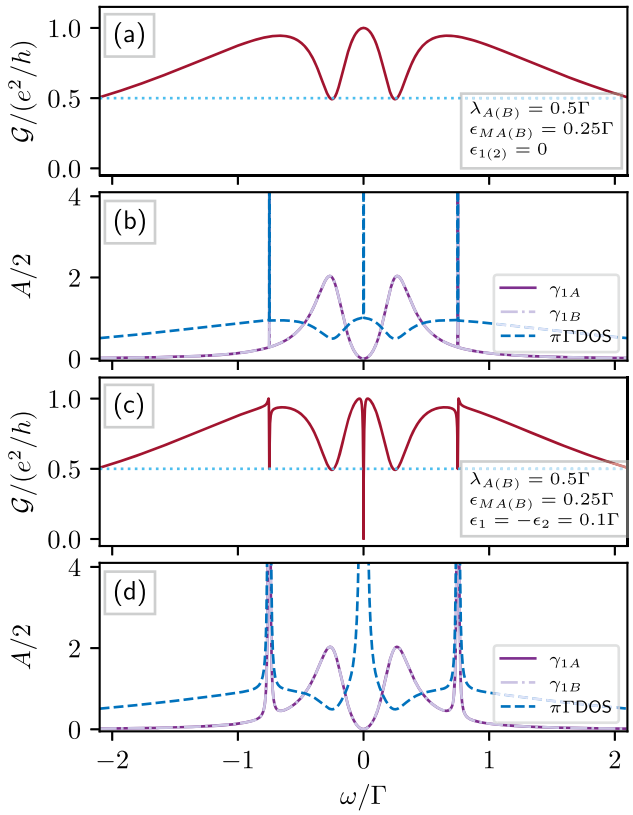

Fig. 3 Linear conductance $\mathcal{G}$, spectral function $A/2$ and DOS as a function of the energy ω across the DQD out of the long-wire limit for both TSCNs ($\lambda_{A(B)} = 0.5\Gamma$ and $\varepsilon_{MA(B)} = 0.25\Gamma$). Panels **a** and **c** show $\mathcal{G}$ with $\varepsilon_{1(2)} = 0$ and $\varepsilon_1 = -\varepsilon_2 = 0.1\Gamma$, respectively. Panels **b** and **d** show the QDs' spectral function $A/2$ and DOS for the cases described in panels **a** and **c**, respectively

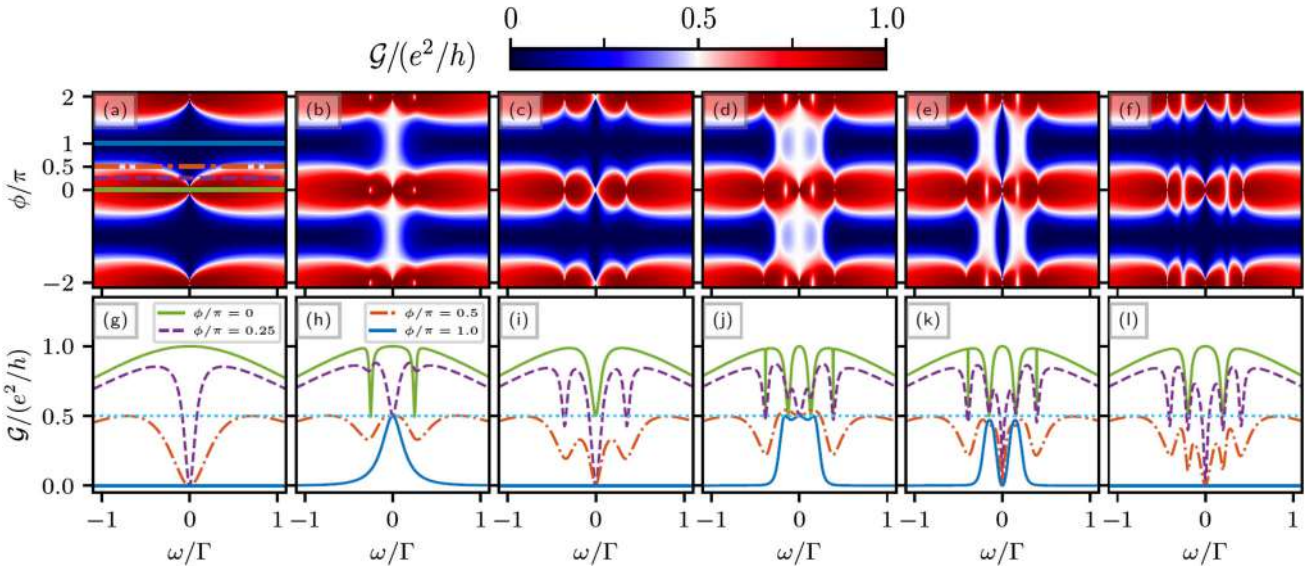

Fig. 4 Color map of the linear conductance $\mathcal{G}$ as a function of both the magnetic flux ϕ and the energy ω in upper panels **a**–**f**, where the red(blue) color represents a maximum(minimum) value. $\mathcal{G}$ as a function of the energy ω for different values of the magnetic flux in lower panels **g**–**l**, where the solid green, dashed purple, dash-dotted orange, and solid blue lines correspond to $\phi/\pi = \{0, 0.25, 0.5, 1\}$, respectively. The QDs' energy levels are $\varepsilon_{1(2)} = 0$ in all panels. In panels **a** and **g** $\lambda_{A(B)} = 0$ is used. In panels **b** and **h** $\lambda_A = 0.25\Gamma$, $\varepsilon_{MA} = 0$, and $\lambda_B = 0$ are used. In panels **c** and **i** $\lambda_{A(B)} = 0.25\Gamma$, and $\varepsilon_{MA(B)} = 0$ are used. In panels **d** and **j** $\lambda_{A(B)} = 0.25\Gamma$, $\varepsilon_{MA} = 0.2\Gamma$, and $\varepsilon_{MB} = 0$ are used. In panels **e** and **k** $\lambda_{A(B)} = 0.25\Gamma$, $\varepsilon_{MA} = 0.2\Gamma$, and $\varepsilon_{MB} = 0.1\Gamma$ are used. In panels **f** and **l** $\lambda_{A(B)} = 0.25\Gamma$, and $\varepsilon_{MA(B)} = 0.2\Gamma$ are used

energy levels $\varepsilon_{1(2)} = 0$ in all panels. Figure 4a corresponds to a DQD interferometer (without TSCNs, $\lambda_{A(B)} = 0$) where the magnetic flux induces a transport suppression for a wide range of values ($\mathcal{G} = 0$, blue color in the color maps). Kubala and König described

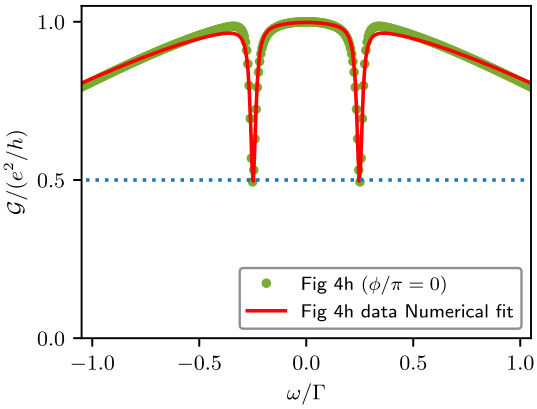

Fig. 5 Conductance $\mathcal{G}$ from Fig. 4h for $\lambda_A = 0.25\Gamma$, $\lambda_B = 0$, $\varepsilon_{MA} = 0$, and $\phi = 0$. The solid red line is a numerical fit using Eq. (18), with $\delta = 0.249$, $\xi = 0.014$, and $\eta = 2.142$ (all in energy units of Γ)

this behavior [55], where the QDs' energy levels are coupled to each other indirectly via the leads. This coupling yields signatures of a flux-dependent level attraction in the linear conductance. Besides, transport suppression occurs whenever both QD levels are close to the Fermi level of the leads. Coupling one TSCN in the long-wire limit ($\lambda_A = 0.25\Gamma$; $\varepsilon_{MA} = 0$) allows transmission around the energy $\omega = 0$, and is independent of the magnetic flux. A half-integer conductance describes this behavior in Fig. 4b, and is also shown in Fig. 4h, where the linear conductance at zero energy takes $\mathcal{G} = e^2/2h$ values when $\phi \neq 2\pi n$ (with integer n). For the case $\phi = 0$, shown in Fig. 4h, we can characterize the linear conductance by means of a convolution of a Fano and a Breit-Wigner line shapes in the form

$$F(\omega) = \frac{|\varepsilon + \tilde{q}|^2}{\varepsilon^2 + 1} \frac{\eta^2}{\omega^2 + \eta^2}, \tag{18}$$

where we have used $\varepsilon = (|\omega| - \delta)/\xi$, and the complex $\tilde{q}$-parameter $\tilde{q} = i/\sqrt{2}$. The latter can be interpreted as an evidence of the presence of a superconductor lead [69], and the particular pure imaginary value seems to be the signature of the leaking of the MZM into the QDs. The δ parameter describes the localization of the antiresonance and, in this particular case, can be identified as the coupling strength λ_A. The comparison between the exact result and the fitting using Eq. (18) is shown in Fig. 5.

By symmetrically coupling both TSCNs in the long-wire limit ($\lambda_{A(B)} = 0.25\Gamma$; $\varepsilon_{MA(B)} = 0$) we obtain a transport suppression as a function of the magnetic flux as shown in Fig. 4c, same as previously in Fig. 4a. Additionally, when $\omega = 0$ the linear conductance reaches a half-integer value ($\mathcal{G} = e^2/2h$) for magnetic flux values $\phi = 2n\pi$, as is also shown in Fig. 4i, where the linear conductance takes the value $\mathcal{G} = e^2/2h$ for $\phi = 0$ (green line), and takes the value $\mathcal{G} = 0$ for $\phi \neq 0$ (purple, orange and blue lines).

In the same way, in the Fig. 4d we coupled both TSCNs considering one of them away from the long-wire limit ($\lambda_{A(B)} = 0.25\Gamma$; $\varepsilon_{MA} = 0.2\Gamma$ and $\varepsilon_{MB} = 0$), where the linear conductance presented in the color map shows that the system allows transport around $\omega = 0$ as a function of the magnetic flux. The linear conductance as a function of the energy ω in Fig. 4j shows that, for $\omega = 0$, the maxima reached are $\mathcal{G} = e^2/2h$ for magnetic flux $\phi \neq 2n\pi$ and $\mathcal{G} = e^2/h$ for $\phi = 2n\pi$. Coupling both TSCNs away from the long-wire limit using different wires lengths ($\lambda_{A(B)} = 0.25\Gamma$; $\varepsilon_{MA} = 0.2\Gamma$ and $\varepsilon_{MB} = 0.1\Gamma$) is addressed in Fig. 4e. For this case we obtain two half-integer peaks in the linear conductance ($\mathcal{G} = e^2/2h$) for $\phi = 2n\pi$. When coupling both TSCNs with equal length ($\lambda_{A(B)} = 0.25\Gamma$ and $\varepsilon_{MA(B)} = 0.2\Gamma$) as shown in Fig. 4f, the transport suppression as a function of the energy ω is recovered as in Fig. 4a and c. For vanishing magnetic flux ($\phi = 0$), we obtain an integer maximum linear conductance $\mathcal{G} = e^2/h$ at zero energy, as well as two dips, reaching the half-integer value $\mathcal{G} = e^2/2h$, placed at energies $\omega = \varepsilon_{MA(B)} = \pm 0.2\Gamma$, as is also shown in Fig. 4l in the solid green line.

We find that the magnetic flux induces a symmetry breaking in the DQD paths, leading to a richer interference phenomena between the hybridized DQD-MZMs states, observable in conductance. This effect is described through zones of total reflection in the color map of the linear conductance (blue values of $\mathcal{G} = 0$). In addition, however, we find that the device allows electronic transport in those zones of total reflection whenever the DQD has one of the following coupling cases: by coupling only one of the TSCN is in the long wire limit [Fig. 4b]; by connecting both TSCNs with one of them in the long-wire limit [Fig. 4d]; or by coupling both TSCNs out of the long-wire limit using different lengths in each one [Fig. 4e], where the signal reaches the $\mathcal{G} = e^2/2h$ value. We interpret the latter signal as MZMs leaking into the QDs. Therefore, tuning the magnetic flux allows control of this leaking and, consequently, the possibility of manipulating the emergence of the MZMs signatures.

Figure 6 displays the density of states (DOS) as a function of the energy ω for magnetic fluxes ϕ: 0, $\pi/1000$, $\pi/100$, and $\pi/10$, in green, purple, orange, and blue colors, respectively. The calculations in panels Fig. 6a–f, use exactly the same combinations of parameters λ_A, λ_B, ε_{MA}, and ε_{MB}, as the bottom panels of Fig. 4 [Fig. 4g–l], correspondingly. In Fig. 6a, we observe a resonance localized in $\omega = 0$ for $\phi = 0$, corresponding to a BIC, which width increases with the magnetic flux. We connected one TSCN in the

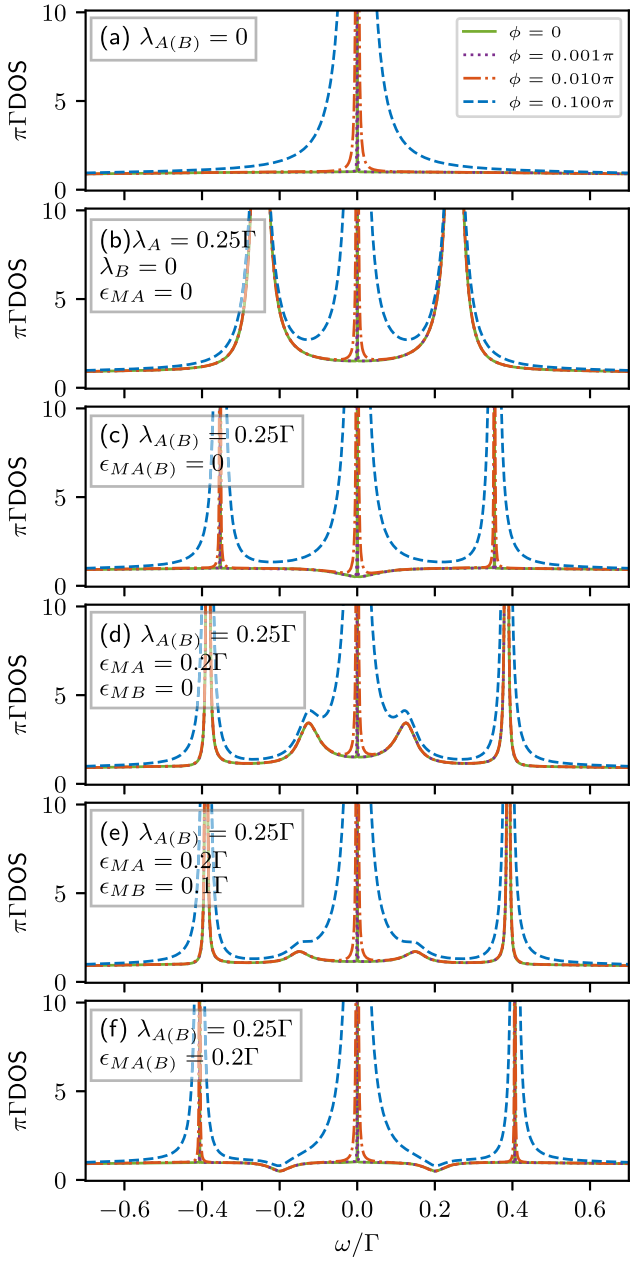

Fig. 6 Density of states (DOS) as a function of the energy ω for different values of the magnetic flux, where the green, purple, orange, and blue lines correspond $\phi = \{0, \pi/1000, \pi/100, \pi/10\}$, respectively. The QDs' energy levels are $\varepsilon_{1(2)} = 0$. In panel **a** $\lambda_{A(B)} = 0$ is used. In panel **b** $\lambda_A = 0.25\Gamma$, $\varepsilon_{MA} = 0$, and $\lambda_B = 0$ are used. In panel **c** $\lambda_{A(B)} = 0.25\Gamma$, and $\varepsilon_{MA(B)} = 0$ are used. In panel **d** $\lambda_{A(B)} = 0.25\Gamma$, $\varepsilon_{MA} = 0.2\Gamma$, and $\varepsilon_{MB} = 0$ are used. In panel **e** $\lambda_{A(B)} = 0.25\Gamma$, $\varepsilon_{MA} = 0.2\Gamma$, and $\varepsilon_{MB} = 0.1\Gamma$ are used. In panel **f** $\lambda_{A(B)} = 0.25\Gamma$, and $\varepsilon_{MA(B)} = 0.2\Gamma$ are used

long-wire limit in Fig. 6b. We can also observe the BIC localized at $\omega = 0$ for $\phi = 0$. Besides, the DOS shows two symmetric wide resonances, centered at energies $\omega = \pm\lambda_A$, due to the hybridization of the MZMs with the QD, which are precisely the position of the antiresonance projected in the linear conductance, as shown in the green curve of Fig. 4h. Figure 6c shows the DOS considering that the two TSCNs in the long-wire limit are connected. We observe the BIC placed at $\omega = 0$ for $\phi = 0$, and two symmetric BICs localized at $\omega^+ = \pm\lambda_{A(B)}\sqrt{2} = 0.25\sqrt{2}\Gamma$, which are given by taking $\varepsilon_{MA(B)} = 0$ in Eq. (17). These states correspond to the hybridized MZMs, which do not show an apparent projection in the linear conductance [see Fig. 4i]. We find that the central BIC in the DQD at zero magnetic flux without TSCNs is destroyed when only one TSCN is coupled to the system. However, it reappears when the two TSCNs are connected. The above can be explained because the symmetry is restored at zero magnetic flux with two TSCNs coupled to the DQD. In a threaded magnetic flux, the central BIC becomes a quasi-BIC. When either one TSCN is out of the long-wire limit [as $\varepsilon_{MA} = 0.2\Gamma$ and $\varepsilon_{MB} = 0$ in Fig. 6d] or when both are out of the long-wire limit and also have different lengths [as $\varepsilon_{MA} = 0.2\Gamma$ and $\varepsilon_{MB} = 0.1\Gamma$ in Fig. 6e], we can observe that the two lateral symmetrical BICs in the DOS gain a finite

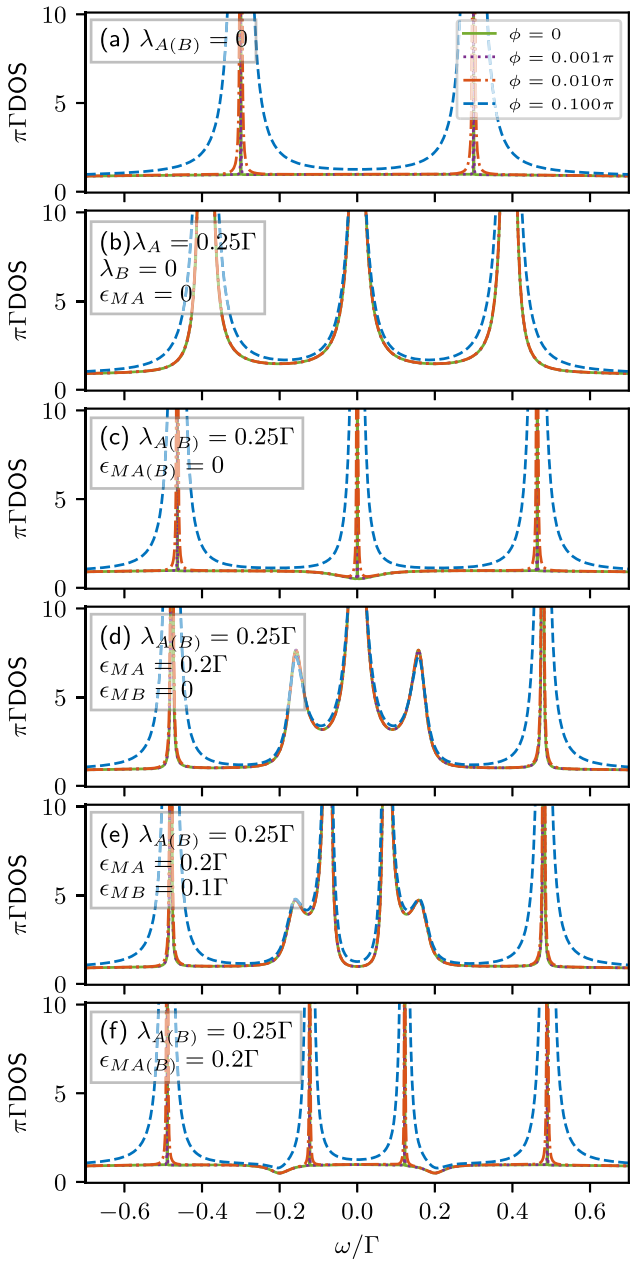

Fig. 7 Density of states (DOS) as a function of the energy ω for different values of the magnetic flux, where the green, purple, orange, and blue lines correspond to the following magnetic flux values: $\phi = \{0, \pi/1000, \pi/100, \pi/10\}$. These are the same calculations as the ones shown in Fig. 6, but now using QDs' energies $\varepsilon_{1(2)} = 0.3\Gamma$

width, hence becoming quasi-BICs. This can also be observed by projections in the linear conductance of the form of antiresonance values up to $\mathcal{G} = e^2/2h$ (Fig. 4j and k, respectively) localized at the same energy. In the case of both TSCNs with finite and equal length [Fig. 6f], we recovered the two lateral symmetrical BICs placed at $\omega^+ = \pm\sqrt{\varepsilon^2_{MA(B)} + 2\lambda^2_{A(B)}} = 0.406\Gamma$ according with Eq. (17). However, these states do not show projections in the linear conductance presented in Fig. 4l.

Figure 7 shows the DOS for the same parameters of Fig. 6, but now breaking the symmetry in the QD' levels in the form of $\varepsilon_{1(2)} = \varepsilon = 0.3\Gamma$. In the case of the DQD without TSCNs [Fig. 7a], we can see two lateral peaks, corresponding to BICs located at energies $\omega = \pm\varepsilon_{1(2)} = \pm 0.3\Gamma$. When one TSCN in the long-wire limit is connected ($\lambda_A = 0.25\Gamma$, $\varepsilon_{MA} = 0$), the DOS displays three wide resonances [Fig. 7b]. When connecting both TSCNs in the long-wire limit ($\lambda_{A(B)} = \lambda = 0.25\Gamma$, $\varepsilon_{MA(B)} = 0$) we obtain three resonances according to Eq. (15), one located at $\omega^- = 0$ (quadruply degenerate) and two laterals located at $\omega^+ = \pm\sqrt{\varepsilon^2 + 2\lambda^2} = \pm 0.464\Gamma$ (each doubly degenerate). When one of the TSCN is taken out of the long-wire limit (Fig. 7c but adding $\varepsilon_{MA} = 0.2\Gamma$), the BIC located at $\omega = 0$ becomes a resonance. Also, the lateral resonances acquire a width due

to the symmetry breaking [Fig. 7d], becoming quasi-BICs. In the same way, when both TSCNs are out of the long-wire limit ($\lambda_{A(B)} = 0.25\Gamma$, $\varepsilon_{MA} = 0.2\Gamma$, and $\varepsilon_{MB} = 0.1\Gamma$), the DOS exhibits two lateral quasi-BICs, and two broad lateral resonances located near to $\omega \approx 0$ [Fig. 7e]. In the symmetric case ($\lambda_{A(B)} = \lambda = 0.25\Gamma$, $\varepsilon_{MA(B)} = \varepsilon_M = 0.2\Gamma$), we can observe the formation of four BICs [Fig. 7f]. According to Eq. (15), they are located at energies $\omega^- = \pm 0.122\Gamma$ and $\omega^+ = \pm 0.490\Gamma$, and each resonance corresponds to a doubly degenerate state. We can interpret from the DOS that the formation of BICs occurs only in symmetric cases, as shown in Fig. 7a, c, and f. Whenever one or both TSCNs are taken out of the long-wire limit (with different lengths), the lateral BICs disappear and become quasi-BICs [Fig. 7d and e].

4 Summary

We studied a system formed by a DQD coupled to two normal leads forming an interferometer configuration. Each QD is independently side coupled to a TSCN hosting MZMs at both ends, and an external magnetic flux across the enclosed interferometer was considered. We focused on the linear conductance across the leads and the DOS of the system, obtained from both the MZMs spectral function and QDs' local density of states. The latter was obtained employing Green's function formalism. We show that the total reflection phenomenon is robust against the coupling of superconducting wires as long as the system's symmetry is maintained, for two favorable symmetric coupling cases: (i) when the system is composed by two TSCNs in the long-wire limit; and (ii) when two TSCNs conform the system out of the long-wire limit with equal length. Besides, for values of the magnetic flux $\phi = 2n\pi$, we find the formation of BICs due to the presence of the coupled MZMs, characterized through resonances of zero width in the DOS, in the same two favorable symmetric coupling cases mentioned above. However, as these states do not project in the conductance, behave as Ghost Fano Majorana anomalies. Also, we find that these BICs destroy as a function of the magnetic flux. On the other hand, whenever $\phi \neq 0$, these states acquire a finite width evolving to quasi-BICs and show a projection in the linear conductance in the form of antiresonances placed at the same energies. These results indicated we could control the bound states generated by switching this external parameter.

Acknowledgements A.P.G. is grateful for the funding of scholarship ANID-Chile No. 21210410. D.Z. acknowledges support from USM-Chile under Grant PI-LIR-2022-13, P.A.O. acknowledges support from FONDECYT grants 1201876 and 1220700.

Author contributions All authors contributed equally and significantly in writing this article. All authors read and approved the final manuscript.

Data Availability Statement This manuscript has associated data in a data repository. [Authors' comment: Data will be made available upon reasonable request to the corresponding author.]

Declarations

Conflict of interest The authors declare that they have no conflict of interest.

Appendix 1: Retarded Green function

The retarded Green's function $\hat{G}^r(\omega) = [\hat{G}^a(\omega)]^\dagger$ is obtained by means of direct inversion, i.e. $\hat{G}^r(\omega) = (\hat{\omega} - \hat{H})^{-1}$ where $\hat{\omega} = \omega\hat{I}$ is the diagonal energy and $\hat{H}$ the system Hamiltonian, both in matrix form. We obtain

$$\hat{G}^r = \begin{pmatrix} \hat{g}_{MA}^{-1} & \hat{\mathcal{H}}_{MA}^\dagger & \hat{0} & \hat{0} \\ \hat{\mathcal{H}}_{MA} & \hat{g}_1^{-1} & \hat{\Lambda} & \hat{0} \\ \hat{0} & -\hat{\Lambda}^* & \hat{g}_2^{-1} & \hat{\mathcal{H}}_{MB} \\ \hat{0} & \hat{0} & \hat{\mathcal{H}}_{MB}^\dagger & \hat{g}_{MB}^{-1} \end{pmatrix}^{-1}, \tag{19}$$

where each element in Eq. (19) corresponds to a 2 x 2 matrix, and are given by

$$\hat{g}_{MA(B)}^{-1} = \begin{pmatrix} \omega - \varepsilon_{MA(B)} & 0 \\ 0 & \omega + \varepsilon_{MA(B)} \end{pmatrix}, \tag{20}$$

for MZMs, and

$$\hat{g}_{1(2)}^{-1} = \begin{pmatrix} \omega - \varepsilon_{1(2)} + \frac{i}{2}\sum_\alpha \Gamma_{11(22)}^\alpha & 0 \\ 0 & \omega + \varepsilon_{1(2)} + \frac{i}{2}\sum_\alpha \Gamma_{11(22)}^\alpha \end{pmatrix}, \tag{21}$$

for QDs, in which the leads contribution are considered. The QD-MZM coupling matrix is

$$\hat{H}_{MA(B)} = \frac{1}{\sqrt{2}}\begin{pmatrix} \lambda^*_{A(B)} & \lambda^*_{A(B)} \\ -\lambda_{A(B)} & -\lambda_{A(B)} \end{pmatrix}, \tag{22}$$

while the inter-QDs coupling matrix is

$$\hat{\Lambda} = \begin{pmatrix} \frac{i}{2}\sum_{\alpha}\Lambda^{\alpha}_{12} & 0 \\ 0 & \frac{i}{2}\sum_{\alpha}\Lambda^{\alpha}_{12} \end{pmatrix}. \tag{23}$$

Obtaining the inversion of Eq. (19), one can identify the necessary matrix elements for the quantities under study. For the LDOS of each QD, the corresponding Green's function is located according to the first diagonal element of Eq. (21). Besides, as the MZM operators are described as a superposition of regular fermionic operators Eqs. (7a)-(7b), the Green's function for $\gamma_{j,\beta}$, $G^r_{\eta,\beta}(\omega)$, is obtained from the addition of all elements located according to Eq. (20).

Appendix 2: Full Green's function poles

We obtain the full Green's function poles from Eq. (19). For the particular case of using $\lambda_A = \lambda_B = \lambda$, $\varepsilon_{MA} = \varepsilon_{MB} = \varepsilon_M$ and $\varepsilon_1 = \varepsilon_2 = \varepsilon$, the poles are described by the roots of

$$P_0 + P_1\omega + P_2\omega^2 + P_3\omega^3 + P_4\omega^4 + P_5\omega^5 + P_6\omega^6 + P_7\omega^7 + \omega^8 = 0, \tag{24}$$

where the coefficients P_i are defined as follows

$$P_0 = \varepsilon_M^4\left[\Gamma^4\sin^4(\phi/2) + 2\varepsilon^2\Gamma^2\left(\cos^2(\phi/2)+1\right) + \varepsilon^2\right], \tag{25}$$

$$P_1 = -4i\Gamma\varepsilon_M^2\left[\varepsilon_M^2 + \lambda^2\right]\left[\varepsilon^2 + \Gamma^2\sin^2(\phi/2)\right], \tag{26}$$

$$\begin{aligned} P_2 = &-2\varepsilon_M^2\Gamma^2\left[\left(2\lambda^2+\varepsilon_M^2\right)\left(3-\cos^2(\phi/2)\right) + \Gamma^2\sin^4(\phi/2)\right] - \varepsilon^2\varepsilon_M^2\left[2\Gamma^2\left(\cos^2(\phi/2)+1\right) + \varepsilon^2 + 2\lambda^2 + \varepsilon_M^2\right] \\ &- 4\lambda^4\Gamma^2\sin^2(\phi/2), \end{aligned} \tag{27}$$

$$P_3 = 4i\Gamma\left[\left(\varepsilon_M^2+\lambda^2\right)\left(\Gamma^2\sin^2(\phi/2) + \varepsilon^2 + 2\lambda^2 + \varepsilon_M^2\right) + \varepsilon_M^2\left(\varepsilon^2 + \Gamma^2\sin^2(\phi/2)\right)\right], \tag{28}$$

$$P_4 = 4\left[\lambda^2+\varepsilon_M^2\right]\left[\lambda^2 + \varepsilon^2 + \Gamma^2\left(3-\cos^2(\phi/2)\right)\right] + \varepsilon_M^4 + \varepsilon^2\left[\varepsilon^2 + 2\Gamma^2\left(\cos^2(\phi/2)+1\right)\right] + \Gamma^4\sin^4(\phi/2), \tag{29}$$

$$P_5 = -4i\Gamma\left[\Gamma^2\sin^2(\phi/2) + \varepsilon^2 + 3\lambda^2 + 2\varepsilon_M^2\right], \tag{30}$$

$$P_6 = -2\left[\Gamma^2\left(3-\cos^2(\phi/2)\right) + \varepsilon^2 + 2\lambda^2 + \varepsilon_M^2\right], \tag{31}$$

$$P_7 = 4i\Gamma. \tag{32}$$

References

1. A.Y. Kitaev, Ann. Phys. **303**, 2 (2003)
2. C. Nayak, S.H. Simon, A. Stern, M. Freedman, S.D. Sarma, Rev. Mod. Phys. **80**, 1083 (2008). https://doi.org/10.1103/RevModPhys.80.1083
3. J.K. Pachos, *Introduction to Topological Quantum Computation* (Cambridge University Press, 2012)
4. C.W.J. Beenakker, Annu. Rev. Condens. Matter Phys. **4**, 113 (2013). https://doi.org/10.1146/annurev-conmatphys-030212-184337
5. C. Laflamme, M. Baranov, P. Zoller, C. Kraus, Phys. Rev. A **89**, 029903 (2014). https://doi.org/10.1103/PhysRevA.89.022319
6. S.M. Albrecht, A.P. Higginbotham, M. Madsen, F. Kuemmeth, T.S. Jespersen, J. Nygård, P. Krogstrup, C. Marcus, Nature **531**, 206 (2016)
7. E. Majorana, Nuovo Cimento **14**, 171 (1937). https://doi.org/10.1007/BF02961314
8. F. Wilczek, Nat. Phys. **5**, 614 (2009)
9. M. Franz, Physics **3**, 24 (2010)
10. C.V. Kraus, M. Dalmonte, M.A. Baranov, A.M. Läuchli, P. Zoller, Phys. Rev. Lett. **111**, 173004 (2013). https://doi.org/10.1103/PhysRevLett.111.173004
11. J. Alicea, Y. Oreg, G. Refael, F. Von Oppen, M. Fisher, Nat. Phys. **7**, 412 (2011)
12. A.Y. Kitaev, Phys.-Usp. **44**, 131 (2001). https://doi.org/10.1070/1063-7869/44/10S/S29/meta
13. S.B. Bravyi, A.Y. Kitaev, Ann. Phys. **298**, 210 (2002)
14. M. Leijnse, K. Flensberg, Phys. Rev. Lett. **107**, 210502 (2011). https://doi.org/10.1103/PhysRevLett.107.210502
15. J. Moore, Nat. Phys. **5**, 378 (2009)
16. B. Wu, J. Cao, Phys. Rev. B **85**, 085415 (2012). https://doi.org/10.1103/PhysRevB.85.085415
17. G. W. Semenoff, P. Sodano, Teleportation by a Majorana Medium (2006) arXiv:cond-mat/0601261
18. S. Tewari, C. Zhang, S.D. Sarma, C. Nayak, D.-H. Lee, Phys. Rev. Lett. **100**, 027001 (2008). https://doi.org/10.1103/PhysRevLett.100.027001
19. V. Mourik, K. Zuo, S.M. Frolov, S. Plissard, E.P. Bakkers, L.P. Kouwenhoven, Science **336**, 1003 (2012). https://doi.org/10.1126/science.1222360
20. C. Bolech, E. Demler, Phys. Rev. Lett. **98**, 237002 (2007). https://doi.org/10.1103/PhysRevLett.98.237002

21. J. Nilsson, A. Akhmerov, C.W.J. Beenakker, Phys. Rev. Lett. **101**, 120403 (2008). https://doi.org/10.1103/PhysRevLett.101.120403
22. K.T. Law, P.A. Lee, T.K. Ng, Phys. Rev. Lett. **103**, 237001 (2009). https://doi.org/10.1103/PhysRevLett.103.237001
23. L. Fu, C.L. Kane, Phys. Rev. B **79**, 161408(R) (2009). https://doi.org/10.1103/PhysRevB.79.161408
24. K. Flensberg, Phys. Rev. B **82**, 180516(R) (2010). https://doi.org/10.1103/PhysRevB.82.180516
25. D. Pikulin, J. Dahlhaus, M. Wimmer, H. Schomerus, C.W.J. Beenakker, New J. Phys. **14**, 125011 (2012). https://doi.org/10.1088/1367-2630/14/12/125011
26. M. Franz, Nat. Nanotechnol. **8**, 149 (2013)
27. E. Prada, P. San-Jose, R. Aguado, Phys. Rev. B **86**, 180503 (2012). https://doi.org/10.1103/PhysRevB.86.180503
28. D. Rainis, L. Trifunovic, J. Klinovaja, D. Loss, Phys. Rev. B **87**, 024515 (2013). https://doi.org/10.1103/PhysRevB.87.024515
29. A. Cook, M. Vazifeh, M. Franz, Phys. Rev. B **86**, 155431 (2012). https://doi.org/10.1103/PhysRevB.86.155431
30. X.-J. Liu, A.M. Lobos, Phys. Rev. B **87**, 060504 (2013). https://doi.org/10.1103/PhysRevB.87.060504
31. T.D. Stanescu, R.M. Lutchyn, S.D. Sarma, Phys. Rev. B **84**, 144522 (2011). https://doi.org/10.1103/PhysRevB.84.144522
32. E.J.H. Lee, X. Jiang, M. Houzet, R. Aguado, C.M. Lieber, S. De Franceschi, Nat. Nanotechnol. **9**, 79 (2014)
33. M. Wimmer, A. Akhmerov, J. Dahlhaus, C. Beenakker, New J. Phys. **13**, 053016 (2011). https://doi.org/10.1088/1367-2630/13/5/053016
34. M. Deng, C. Yu, G. Huang, M. Larsson, P. Caroff, H. Xu, Nano Lett. **12**, 6414 (2012). https://doi.org/10.1021/nl303758w
35. A. Das, Y. Ronen, Y. Most, Y. Oreg, M. Heiblum, H. Shtrikman, Nat. Phys. **8**, 887 (2012)
36. E.J.H. Lee, X. Jiang, R. Aguado, G. Katsaros, C.M. Lieber, S. De Franceschi, Phys. Rev. Lett. **109**, 186802 (2012). https://doi.org/10.1103/PhysRevLett.109.186802
37. A. Finck, D. Van Harlingen, P. Mohseni, K. Jung, X. Li, Phys. Rev. Lett. **110**, 126406 (2013). https://doi.org/10.1103/PhysRevLett.110.126406
38. H. Churchill, V. Fatemi, K. Grove-Rasmussen, M. Deng, P. Caroff, H. Xu, C.M. Marcus, Phys. Rev. B **87**, 241401 (2013)
39. D. Zambrano, J.P. Ramos-Andrade, P. Orellana, J. Phys. Condens. Matter. **30**, 375301 (2018). https://doi.org/10.1088/1361-648X/aad7ca
40. J.P. Ramos-Andrade, D. Zambrano, P.A. Orellana, Ann. Phys. **531**, 1800498 (2019). https://doi.org/10.1002/andp.201800498
41. M. Valentini, M. Borovkov, E. Prada, S. Martí-Sánchez, M. Botifoll, A. Hofmann, J. Arbiol, R. Aguado, P. San-José, G. Katsaros, Nature **612**, 442 (2022)
42. C.W. Hsu, B. Zhen, A.D. Stone, J.D. Joannopoulos, M. Soljačić, Nat. Rev. Mater. **1**, 1 (2016)
43. J. von Neumann, E.P. Wigner, Z. Phys. **30**, 465 (1929)
44. J.P. Ramos, P.A. Orellana, Phys. B Condens. Matter **455**, 66 (2014)
45. B. Grez, J. Ramos-Andrade, V. Juričić, P. Orellana, Phys. Rev. A **106**, 013719 (2022). https://doi.org/10.1103/PhysRevA.106.013719
46. W.G. Van der Wiel, S. De Franceschi, J.M. Elzerman, T. Fujisawa, S. Tarucha, L.P. Kouwenhoven, Rev. Mod. Phys. **75**, 1 (2002). https://doi.org/10.1103/RevModPhys.75.1
47. R. Hanson, L.P. Kouwenhoven, J.R. Petta, S. Tarucha, L.M. Vandersypen, Rev. Mod. Phys. **79**, 1217 (2007). https://doi.org/10.1103/RevModPhys.79.1217
48. A. Holleitner, C. Decker, H. Qin, K. Eberl, R. Blick, Phys. Rev. Lett. **87**, 256802 (2001). https://doi.org/10.1103/PhysRevLett.87.256802
49. A.W. Holleitner, R.H. Blick, A.K. Huttel, K. Eberl, J.P. Kotthaus, Science **297**, 70 (2002). https://doi.org/10.1126/science.1071215
50. W.Z. Shangguan, T.C.A. Yeung, Y.B. Yu, C.H. Kam, Phys. Rev. B **63**, 235323 (2001). https://doi.org/10.1103/PhysRevB.63.235323
51. P.A. Orellana, F. Dominguez-Adame, I. Gómez, M.L.L. De Guevara, Phys. Rev. B **67**, 085321 (2003). https://doi.org/10.1103/PhysRevB.67.085321
52. W. Hofstetter, J. König, H. Schoeller, Phys. Rev. Lett. **87**, 156803 (2001). https://doi.org/10.1103/PhysRevLett.87.156803
53. G. Górski, K. Kucab, Phys. Status Solidi B **256**, 1800492 (2019). https://doi.org/10.1002/pssb.201800492
54. F. Chi, J.-L. Liu, L.-L. Sun, J. Appl. Phys. **101**, 093704 (2007). https://doi.org/10.1063/1.2720097?casa_token=9YYOouWNqmYAAAAA
55. B. Kubala, J. König, Phys. Rev. B **65**, 245301 (2002). https://doi.org/10.1103/PhysRevB.65.245301
56. U. Fano, Phys. Rev. **124**, 1866 (1961). https://doi.org/10.1103/PhysRev.124.1866
57. A.E. Miroshnichenko, S. Flach, Y.S. Kivshar, Rev. Mod. Phys. **82**, 2257 (2010). https://doi.org/10.1103/RevModPhys.82.2257
58. M.L. Ladrón de Guevara, F. Claro, P.A. Orellana, Phys. Rev. B **67**, 195335 (2003). https://doi.org/10.1103/PhysRevB.67.195335
59. W.-J. Gong, S.-F. Zhang, Z.-C. Li, G. Yi, Y.-S. Zheng, Phys. Rev. B **89**, 245413 (2014). https://doi.org/10.1103/PhysRevB.89.245413
60. F. Chi, J. Wang, T.-Y. He, Z.-G. Fu, P. Zhang, X.-W. Zhang, L. Wang, Z. Lu, Front. Phys. **8**, 631031 (2021). https://doi.org/10.3389/fphy.2020.631031/full
61. D.E. Liu, H.U. Baranger, Phys. Rev. B **84**, 201308 (2011). https://doi.org/10.1103/PhysRevB.84.201308
62. E. Vernek, P.H. Penteado, A.C. Seridonio, J.C. Egues, Phys. Rev. B **89**, 165314 (2014). https://doi.org/10.1103/PhysRevB.89.165314
63. M. Deng, S. Vaitiekėnas, E.B. Hansen, J. Danon, M. Leijnse, K. Flensberg, J. Nygård, P. Krogstrup, C.M. Marcus, Science **354**, 1557 (2016). https://doi.org/10.1126/science.aaf3961
64. L.S. Ricco, Y. Marques, F.A. Dessotti, R.S. Machado, M. De Souza, A.C. Seridonio, Phys. Rev. B **93**, 165116 (2016). https://doi.org/10.1103/PhysRevB.93.165116
65. L.H. Guessi, F.A. Dessotti, Y. Marques, L.S. Ricco, G.M. Pereira, P. Menegasso, M. De Souza, A.C. Seridonio, Phys. Rev. B **96**, 041114(R) (2017). https://doi.org/10.1103/PhysRevB.96.041114
66. D.A. Ruiz-Tijerina, E. Vernek, L.G.G.V. Dias da Silva, J.C. Egues, Phys. Rev. B **91**, 115435 (2015). https://doi.org/10.1103/PhysRevB.91.115435
67. S. Datta, *Quantum Transport: Atom to Transistor* (Cambridge University Press, 2005)
68. Y. Meir, N.S. Wingreen, Phys. Rev. Lett. **68**, 2512 (1992). https://doi.org/10.1103/PhysRevLett.68.2512
69. A.M. Calle, M. Pacheco, P.A. Orellana, J.A. Otálora, Ann. Phys. **532**, 1900409 (2020). https://doi.org/10.1002/andp.201900409

Chapter 3

Thermoelectric transport through a MZMs-leads interferometer

An alternative method for detecting Majorana zero modes (MZMs) leverages thermoelectric measurements, which provide distinct advantages by capturing their unique transport signatures. These measurements can reveal MZM signatures through thermal conductance, thermoelectric voltage, or violations of the Wiedemann-Franz law, offering complementary evidence that goes beyond zero-bias anomalies.

3.1 Thermoelectrics quantities

The system under study are framed within the linear response regime. In this scenario, to obtain the thermoelectric quantities, we consider that there is a temperature difference ΔT between the two contacts used. With this, it is possible to express both the charge current I_{charge} and the heat current I_{heat} in terms of a potential difference ΔV as,

$$I_{\text{charge}} = -e^2 L_0 \Delta V + \frac{e}{T} L_1 \Delta T, \tag{3.1}$$

$$I_{\text{heat}} = e L_1 \Delta V - \frac{1}{T} L_2 \Delta T, \tag{3.2}$$

where the coefficients L_n correspond to the so-called kinetic integrals, which are given by,

$$L_n(\mu) = \frac{1}{h} \int \mathrm{d}\varepsilon \left(-\frac{\partial \mathscr{F}(\varepsilon, \mu)}{\partial \varepsilon} \right) (\varepsilon - \mu)^n \mathscr{T}(\varepsilon), \tag{3.3}$$

where h is Planck's constant, $\mathscr{F}(\varepsilon,\mu)$ the Fermi distribution, and $\mathscr{T}(\varepsilon)$ the transmission probability trough the device. Note that the electrical conductance $\mathscr{G}$ is defined as the ratio between the charge current and the potential difference for the limit $\Delta T \to 0$. Therefore, we obtain,

$$\mathscr{G}(\mu) = -\frac{I_{\text{charge}}}{\Delta V} = e^2 L_0, \tag{3.4}$$

Analogously to the electronic case, the thermal conductance κ is defined as the ratio between the heat current and the temperature gradient that generates it, when $I_{\text{charge}} \to 0$. Thus, we obtain,

$$\kappa(\mu) = -\frac{I_{\text{heat}}}{\Delta T} = \frac{1}{T}\left(L_2 - \frac{L_1^2}{L_0}\right). \tag{3.5}$$

The thermal conductance, in general, comprises electronic and phononic contributions. The above equation only considers the electronic contribution, as the phonon contribution is negligible at low temperatures, typically a few Kelvin, which are common in systems involving conventional superconductors.

On the other hand, one of the quantities that characterizes a system's ability to generate potential differences from a temperature gradient is the Seebeck coefficient S, also called thermopower. By definition, this corresponds to the proportionality between the temperature difference and the generated voltage for zero charge current. S is given by,

$$S(\mu) = -\frac{\Delta V}{\Delta T} = -\frac{1}{eT}\frac{L_1}{L_0}. \tag{3.6}$$

A way to quantify the efficiency of a system in thermoelectric transport, such as generating current from a temperature difference (or vice versa), is through the figure of merit ZT,

$$ZT = \frac{S^2 \mathscr{G} T}{\kappa}, \tag{3.7}$$

which is a dimensionless quantity dependent on the system's structural parameters. Values of $ZT \sim 1$ are considered evidence of an efficient system. One way to achieve efficient values is through the violation of the Wiedemann-Franz law, which states that,

$$\frac{\kappa}{\mathscr{G} T} = \text{constant} = \ell_0, \tag{3.8}$$

where $\ell_0 = (\pi^2/3)(k_B/e)^2$ is the Lorenz number. It has been shown that systems with nanostructures can achieve efficient values, $ZT \gtrsim 1$, by violating this law through electron-hole symmetry breaking and interference phenomena.

3.2 Outline

In the following paper we study a system composed of two normal leads coupled to two TSCNs, each hosting MZMs at their ends, arranged in an interferometer configuration. We focused on the electronic and thermal conductances between the leads, as well as on the spectral functions of the MZMs and thermoelectric quantities. The latter were obtained using the Green's function formalism, while thermoelectric properties were analyzed via the Sommerfeld expansion.

Thermoelectric transport through a Majorana zero modes interferometer

A. P. Garrido,[1,*] D. Zambrano,[1] J. P. Ramos-Andrade,[2] and P. A. Orellana[1]

[1] *Departamento de Física, Universidad Técnica Federico Santa María, Av. España 1680, Casilla 110V, Valparaiso, Chile.*

[2] *Departamento de Física, Universidad de Antofagasta, Av. Angamos 601, Casilla 170, Antofagasta, Chile.*

(Dated: April 9, 2025)

In this study, we examine the thermoelectric characteristics of a system consisting of two topological superconducting nanowires, each exhibiting Majorana zero modes at their ends, connected to leads within an interferometer configuration. By employing Green's function formalism, we derive the spectral properties and transport coefficients. Our findings indicate that bound states in the continuum (BICs) manifest in symmetric setups, influenced by the length of the wires and coupling parameters. Deviations of the magnetic flux from specific values transform BICs into quasi-BICs with finite width, resulting in conductance antiresonances. The existence and interplay of Majorana zero modes enhance thermoelectric performance in asymmetric configurations. Modulating the magnetic flux transitions BICs into quasi-BICs significantly enhances the Seebeck coefficient and figure of merit, thereby proposing a strategy for optimizing thermoelectric efficiency in systems based on Majorana zero modes.

I. INTRODUCTION

Recently, topological superconductor nanowires (TSCNs) have attracted significant attention in condensed matter physics for their potential in quantum computing [1–6]. Exotic fermionic quasiparticles predicted within this framework, being their own antiquasiparticles, have emerged [7–9]. These quasiparticles, known as Majorana zero modes (MZMs), are localized in topological superconductors. The MZMs exhibit non-Abelian statistics and are manipulated through braiding operations [10, 11], making them ideal for fault-tolerant quantum computation [1–3, 6, 10, 12–14]. They are predicted at the ends of a TSCN comprising a semiconductor-superconductor nanowire with strong spin-orbit interaction under a magnetic field. The aforementioned system can be viewed as a realization of a Kitaev chain [1, 12, 15], where the coupling between the two MZMs located at opposite ends of the wire decays exponentially with the wire's length [6]. This enables the construction of a qubit that is topologically protected from decoherence by local perturbations [6, 10, 12, 16–18]. Mourik and collaborators achieved the first physical realization of this system, reporting zero-bias anomalies in conductance as evidence of the presence of MZMs [19]. However, these anomalies do not always provide conclusive evidence of MZMs, highlighting the need for custom-designed experimental protocols [19–26]. An alternative method to identify MZMs involves using thermoelectric measurements, which offer distinct advantages by exploring their unique transport signatures. Conventional thermoelectric measurement techniques, developed in the early 1990s [27, 28], have developed into potent tools for detecting chargeless MZMs. These techniques can disclose MZM signatures through thermal conductance [29, 30], voltage thermopower [31–33], or the breach of the Wiedemann-Franz (WF) law [34–36], providing complementary evidence beyond zero-bias anomalies.

Contemporary protocols facilitate the identification of topological phases featuring MZMs in superconductor-semiconductor devices [37]. This is achieved through a three-terminal configuration comprising two normal leads alongside a superconducting lead, which employs nonlocal conductance measurements to observe topological transitions via variations in the energy gap. The experiments carried out by Aghaee et al. substantiated these findings in heterostructures, affirming thus the presence of topological superconductivity and MZMs [38]. Recent advances in quantum computing exploit the principles of Majorana physics; notably, the Majorana-1 processor incorporates MZMs, resulting in enhanced scalability [39]. Conversely, bound states in the continuum (BICs) remain stable even when their energy levels reside within the domain of continuum states [40]. Originally predicted by von Neumann and Wigner [41], BICs have garnered considerable interest, especially within photonic systems. Furthermore, owing to the similar interference phenomena observed in both electronic and photonic systems, the potential presence of BICs in electronic systems has been posited [25, 40, 42–44].

In this work, we study a system composed of two normal leads that interact in parallel with two TSCNs that host MZMs at their ends, forming an interferometer configuration, as illustrated in FIG. 1. Our primary focus is on the thermal and electrical conductances between the normal leads and the spectral functions of the MZMs, computed using the Green function (GF) formalism. By modulating the magnetic flux within the interferometer, we discern signatures of quantum interference phenomena and the interaction between MZMs and BICs. Our findings indicate that BICs manifest in high-symmetry

* alejandro.garridoh@usm.cl

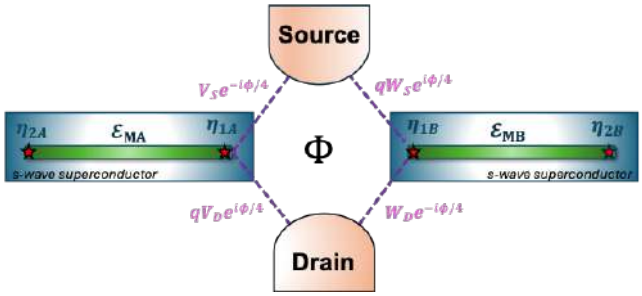

FIG. 1. Schematic representation of the system under study: The TSCN $A(B)$ is connected to the lead S(D) and hosts two MZMs, $\eta_{1,A(B)}$ and $\eta_{2,A(B)}$, at its ends, with the intracoupling Majorana term given by $\varepsilon_{MA(B)}$. An external magnetic flux Φ threading the interferometer is considered. The parameters $V_{S(D)}(W_{S(D)})$ represent the couplings among the system's components, while q is a dimensionless asymmetry parameter, where $q = 1$ ($q = 0$) corresponds to a closed (open) system, as explained later in the main text.

configurations, depending on the coupling strength between the TSCNs and the leads, as well as the lengths of the TSCNs. Moreover, we detect suppression in electronic and thermal conductance as a function of external magnetic flux, occurring within the mentioned symmetric configurations. We ascertain that the interaction between MZMs and BICs can be either triggered or inhibited by the magnetic flux, demonstrating the potential of this external parameter to effectively control these states. Finally, the annihilation of BICs by magnetic flux and/or asymmetry in couplings can enhance the response in thermopower and figure of merit and then enhance the thermoelectric efficiency of the system.

The structure of this paper is organized as follows. Section II elucidates the model along with the methodology used to derive the quantities of interest; Section III presents the results and their subsequent discussion; and Section IV offers the concluding remarks.

II. MODEL AND METHOD

We consider an interferometer configuration in which each TSCN is connected to two normal leads, S and D, and hosts MZMs at both ends, as schematically shown in Fig. 1. We model the system using an effective low-energy Hamiltonian of the following form:

$$H = H_{\text{leads}} + H_{\text{M}} + H_{\text{M-leads}}\,, \tag{1}$$

where the first term on the right-hand side corresponds to the regular electronic contribution of the leads, given by

$$H_{\text{leads}} = \sum_{\alpha,\mathbf{k}} \varepsilon_{\alpha,\mathbf{k}} a^{\dagger}_{\alpha,\mathbf{k}} a_{\alpha,\mathbf{k}}\,, \tag{2}$$

where the operator $a^{\dagger}_{\alpha,\mathbf{k}}(a_{\alpha,\mathbf{k}})$ is the electron creation (annihilation) operator with momentum $\mathbf{k}$ and energy $\varepsilon_{\alpha,\mathbf{k}}$ in lead $\alpha =$ S,D.

The middle and last terms in the Hamiltonian presented in Eq. (1) correspond to MZM-related terms, specifically MZM$_\beta$–MZM$_\beta$ and TSCN$_\beta$–lead$_\alpha$ couplings, given by

$$H_{\text{M}} = \sum_{\beta} i\varepsilon_{_{M,\beta}} \eta_{_{1,\beta}} \eta_{_{2,\beta}}\,, \tag{3}$$

$$H_{\text{M-leads}} = \sum_{\beta} \left\{ \sum_{\alpha,\mathbf{k}} (t_{\alpha,\mathbf{k},\beta} a_{\alpha,\mathbf{k}} - t^{*}_{\alpha,\mathbf{k},\beta} a^{\dagger}_{\alpha,\mathbf{k}}) \eta_{_{1,\beta}} \right\}\,, \tag{4}$$

where $\eta_{_{j,\beta}}$ denotes the MZM operator (with $j = 1, 2$ and $\beta = A, B$) and satisfies both $\eta_{_{j,\beta}} = \left[\eta_{_{j,\beta}}\right]^{\dagger}$ and $\{\eta_{_{j,\beta}}, \eta_{_{j',\beta'}}\} = \delta_{_{j,j'}}\delta_{_{\beta,\beta'}}$. Additionally, $\varepsilon_{_{M,\beta}} \propto \exp\left(-L_\beta/\zeta\right)$ represents the coupling amplitude between two MZMs in the same TSCN, where L_β corresponds to the wire's length and ζ denotes the superconducting coherence length. The parameter $t_{\alpha,\mathbf{k},\beta}(\varphi_{\alpha,\beta}) = t^{(0)}_{\alpha,\mathbf{k},\beta} \exp\left[i\varphi_{\alpha,\beta}\right]$ describes the TSCN$_\beta$–lead$_\alpha$ tunnel matrix element, where an Aharonov-Bohm (AB) phase is included to model the magnetic flux Φ across the interferometer. We adopt a symmetric gauge such that $\varphi_{_{D,A}} = -\varphi_{_{D,B}} = -\varphi_{_{S,A}} = \varphi_{_{S,B}} = \phi/4$, with $\phi = 2\pi\Phi/\Phi_0$ and $\Phi_0 = h/e$ being the quantum flux, where h is Planck's constant and e the electron charge.

The GF is obtained from $(\mathbf{G}^r)^{-1} = \mathbf{g}_0^{-1} + i\pi\boldsymbol{\Upsilon}\boldsymbol{\Upsilon}^{\dagger}$, where $\mathbf{g}_0^{-1}$ represents the Green's function of the isolated MZMs. The matrix $\boldsymbol{\Upsilon}$ describes the coupling between the scatterer (H_{M}) and the leads. Since only MZM-1β is coupled to the leads, the matrix representation of $\mathbf{g}_0^{-1}$ and $\boldsymbol{\Upsilon}$ can be expressed in the basis $\{\eta_{_{1A}}, \eta_{_{1B}}\}$, given by

$$\mathbf{g}_0^{-1} = \begin{pmatrix} \omega & -i\varepsilon_{_{MA}} & 0 & 0 \\ i\varepsilon^{*}_{_{MA}} & \omega & 0 & 0 \\ 0 & 0 & \omega & -i\varepsilon_{_{MB}} \\ 0 & 0 & i\varepsilon^{*}_{_{MB}} & \omega \end{pmatrix}\,, \tag{5}$$

and

$$\boldsymbol{\Upsilon} = \begin{pmatrix} -V_S e^{-i\phi/4} & -qV_D e^{i\phi/4} & V_S e^{i\phi/4} & qV_D e^{-i\phi/4} \\ 0 & 0 & 0 & 0 \\ -qW_S e^{i\phi/4} & -W_D e^{-i\phi/4} & qW_S e^{-i\phi/4} & W_D e^{i\phi/4} \\ 0 & 0 & 0 & 0 \end{pmatrix}\,. \tag{6}$$

The Hamiltonian described in Eq.(1) is spinless since only electrons with one spin projection will couple to the MZMs [45].

The transmission probability is calculated from the expression

$$\mathcal{T}(\omega) = \text{Tr}\{\mathbf{G}^a(\omega)\boldsymbol{\Gamma}^D\mathbf{G}^r(\omega)\boldsymbol{\Gamma}^S\}\,, \tag{7}$$

where $\mathbf{G}^{r(a)}(\omega)$ is the system retarded (advanced) GF in the energy domain, and is obtained from

$$[\mathbf{G}^r]^{-1} = \begin{pmatrix} \omega + i\sum_\alpha \Gamma_A^\alpha & -i\varepsilon_{MA} & K & 0 \\ i\varepsilon_{MA}^* & \omega & 0 & 0 \\ K & 0 & \omega + i\sum_\alpha \Gamma_B^\alpha & -i\varepsilon_{MB} \\ 0 & 0 & i\varepsilon_{MB}^* & \omega \end{pmatrix}, \tag{8}$$

where $\Gamma_A^\alpha = 2\pi|V_\alpha|^2\rho_\alpha$, $\Gamma_B^\alpha = 2\pi|W_\alpha|^2\rho_\alpha$, and we have defined the function

$$K = i\left[\sqrt{\Gamma_A^S\Gamma_B^S}e^{i\phi/2} + \sqrt{\Gamma_B^D\Gamma_A^D}e^{-i\phi/2}\right]. \tag{9}$$

The retarded GF satisfies $\mathbf{G}^r(\omega) = [\mathbf{G}^a(\omega)]^\dagger$. $\mathbf{\Gamma}^{D(S)}$ is the line-width function denoting the coupling between the MZMs and the lead−D(S), and is given by

$$\mathbf{\Gamma}^\alpha = \begin{pmatrix} \Gamma_{AA}^\alpha & 0 & \Lambda_{AB}^\alpha & 0 \\ 0 & 0 & 0 & 0 \\ \Lambda_{BA}^\alpha & 0 & \Gamma_{BB}^\alpha & 0 \\ 0 & 0 & 0 & 0 \end{pmatrix}, \tag{10}$$

where we have defined $\Lambda_{\beta\beta'}^\alpha = \sqrt{\Gamma_{\beta\beta'}^\alpha\Gamma_{\beta'\beta}^\alpha}$, and $\Gamma_{\beta\beta'}^\alpha = 2\pi t_{\alpha,\mathbf{k},\beta}(\varphi_{\alpha\beta})[t_{\alpha,\mathbf{k},\beta'}(\varphi_{\alpha\beta'})]^*\rho_\alpha$ is the tunnel-coupling strength, with ρ_α being the local density of states in the lead α.

To examine the thermoelectric properties, we consider the system in the linear response regime, characterized by a temperature difference ΔT between the two leads. In this framework, the charge and heat currents, I_{charge} and I_{heat}, can be expressed as functions of the potential difference ΔV as

$$I_{\text{charge}} = -e^2L_0\Delta V + \frac{e}{T}L_1\Delta T, \tag{11}$$

$$I_{\text{heat}} = eL_1\Delta V - \frac{1}{T}L_2\Delta T, \tag{12}$$

where the integrals L_n are obtained from,

$$L_n(\mu,T) = \frac{1}{h}\int_0^\infty \left(-\frac{\partial f(\omega,\mu)}{\partial\omega}\right)(\omega-\mu)^n\mathcal{T}(\omega)\,\mathrm{d}\omega, \tag{13}$$

where $f(\omega,\mu) = [\exp\{(\omega-\mu)/k_\mathrm{B}T\}+1]^{-1}$ is the Fermi distribution function and k_B the Boltzmann constant. The Seebeck coefficient S, also known as thermopower, describes the relationship between the temperature difference ΔT and the resulting potential difference ΔV induced when the charge current vanishes,

$$S(\mu) = -\frac{\Delta V}{\Delta T} = -\frac{1}{eT}\frac{L_1}{L_0}. \tag{14}$$

The electrical conductance $\mathcal{G}(\mu)$ is defined as the ratio of the charge current to the potential difference when the temperature difference ΔT is zero. Similarly, the thermal conductance $\kappa(\mu)$ is defined as the ratio of the heat current to the temperature gradient when the charge current is zero. Based on Eqs. (11) and (12), both conductances can be expressed as:

$$\mathcal{G}(\mu) = -\frac{I_{\text{charge}}}{\Delta V} = e^2L_0, \tag{15}$$

$$\kappa(\mu) = -\frac{I_{\text{heat}}}{\Delta T} = \frac{1}{T}\left(L_2 - \frac{L_1^2}{L_0}\right). \tag{16}$$

Note that Eq. (16) accounts only for the electronic contribution to the thermal conductance, assuming that the phononic contribution is negligible in the low-temperature regime (a few kelvins) typical of these systems.

To quantify the efficiency of our MZM thermoelectric setups, we calculate the dimensionless figure of merit ZT, defined as

$$ZT = \frac{S^2\mathcal{G}T}{\kappa}. \tag{17}$$

An means to improve the ZT factor involves exceeding the constraints imposed by the Wiedemann-Franz (WF) law, which dictates the ratio $\kappa/\mathcal{G}T = \mathcal{L}_0 \equiv$ *constant* across all systems, where $\mathcal{L}_0 = (\pi^2/3)(k_B/e)^2$ represents the Lorenz number. Although macroscopic materials typically adhere to the WF law, nanostructured systems have demonstrated exceptional capability as thermoconverters, effectively transcending this restriction [46]. The four quantities defined above, $\mathcal{G}$, κ, S, and ZT, can be obtained using the Sommerfeld expansion in the integrals L_n, yielding the following:

$$L_0 = \frac{1}{h}\left[\mathcal{T}^{(0)} + \frac{\pi^2}{6}\mathcal{T}^{(2)}\xi^2 + \frac{7\pi^4}{360}\mathcal{T}^{(4)}\xi^4 + \mathcal{O}(\xi^6)\right], \tag{18}$$

$$L_1 = \frac{1}{h}\left[\frac{\pi^2}{3}\mathcal{T}^{(1)}\xi^2 + \frac{7\pi^4}{90}\mathcal{T}^{(3)}\xi^4 + \mathcal{O}(\xi^6)\right], \tag{19}$$

$$L_2 = \frac{1}{h}\left[\frac{\pi^2}{3}\mathcal{T}^{(0)}\xi^2 + \frac{7\pi^4}{30}\mathcal{T}^{(2)}\xi^4 + \mathcal{O}(\xi^6)\right], \tag{20}$$

where $\mathcal{T}^{(n)}(\mu) = (d^n\mathcal{T}/d\omega^n)(\mu)$, and $\xi = k_B T$.

We also investigated the behavior of the spectral function, since it is closely related to resonances in the conductance. The spectral function is expressed as

$$\mathrm{A}(\omega) = -\frac{1}{\pi}\mathrm{Im}\left[\mathrm{Tr}\{\mathbf{G}^r(\omega)\}\right], \tag{21}$$

and the spectral function for each TSCN are expressed as

$$\mathrm{A}_{jA}(\omega) = -\frac{1}{\pi}\mathrm{Im}\{\mathbf{G}^r_{jj}(\omega)\}, \tag{22}$$

$$\mathrm{A}_{jB}(\omega) = -\frac{1}{\pi}\mathrm{Im}\{\mathbf{G}^r_{j+2,j+2}(\omega)\}, \tag{23}$$

where $j = 1, 2$. Moreover, the complete GF poles are closely related to the eigenvalues of the isolated TSCN-TSCN (disconnected from leads), and give reliable information about the energy localization of the system's states. The eigenvalues equation can be written as

$$\omega^4 - \varepsilon^2_{MA}\varepsilon^2_{MB} = 0. \tag{24}$$

obtaining 2-degenerate solutions in the form

$$\omega_{[\pm]} = \pm\sqrt{\varepsilon_{MA}\varepsilon_{MB}}. \tag{25}$$

For instance, in the particular case of long wire limit for both TSCN ($\varepsilon_{MA} = \varepsilon_{MB} = 0$),

$$\omega_{[\pm]} = 0. \tag{26}$$

III. RESULTS

We have considered the wide-band approximation, in which ρ_α has an approximately constant value, and then Γ^α_B and Γ^α_B are energy independent. Thus, we fixed the values $\Gamma^S_A = \Gamma^D_A = \Gamma^S_B = \Gamma^D_B = \Gamma$, and q is a dimensionless parameter with $q = 1(q = 0)$ corresponding to a close(open) system. In the following, all energy parameters are given in units of Γ. In order to consider realistic parameters with experiments, the values of Γ can be considered from a few to hundreds of meV. We assume a background temperature of $T = 1\,\mathrm{K}$, well below typical superconductor critical temperatures [47].

First, we analyze the electronic transport in the system by considering three scenarios: only one, both, or neither TSCN in the long-wire limit. In this regime, the MZMs in each TSCN can interfere in the transmission process

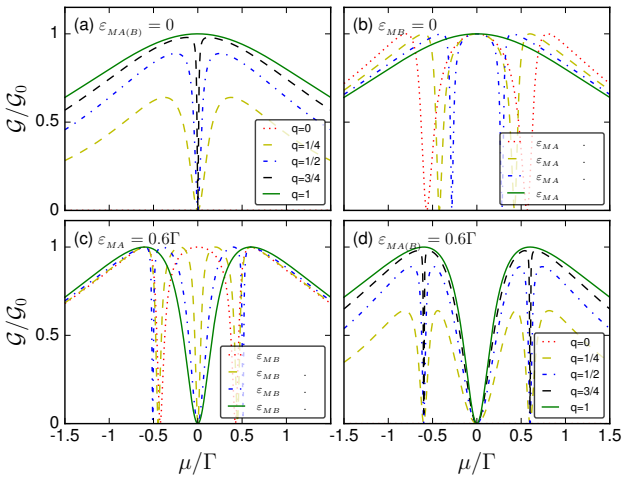

FIG. 2. Electronic conductance $\mathcal{G}$ as a function of chemical potential μ without magnetic flux ($\phi = 0$), we show the cases (a) $\varepsilon_{MA(B)} = 0$ (long wire limit) with $q \in [0, 1]$, (b) $\varepsilon_{MB} = 0$ with $\varepsilon_{MA}/\Gamma = \{0, 0.4, 0.6, 0.8\}$, (c) $\varepsilon_{MA} = 0.6\Gamma$ with $\varepsilon_{MB}/\Gamma = \{0, 0.2, 0.4, 0.6\}$, and (d) $\varepsilon_{MA(B)} = 0.6\Gamma$ with $q \in [0, 1]$. The dimensionless asymmetry parameter q corresponds to a close(open) system for $q = 1(q = 0)$, respectively.

depending on whether they are coupled ($\varepsilon_{M\beta} \neq 0$) or decoupled ($\varepsilon_{M\beta} = 0$). The electronic conductance $\mathcal{G}$ as a function of the chemical potential μ is shown in Fig. 2. Panel (a) corresponds to the case where both TSCNs are in the long wire limit ($\varepsilon_{MA(B)} = 0$), ensuring that the MZMs are decoupled from the external ends of each TSCN. The dimensionless asymmetry parameter q characterizes the openness of the system: $q = 1$ corresponds to a closed system, while $q = 0$ corresponds to an open one. We obtain a Breit–Wigner resonance centered at $\mu = 0$ for $q = 1$, while an antiresonance at $\mu = 0$ appears for $q \neq 1$. We also show that the electronic conductance progressively decreases to zero as the circuit transitions from a closed system ($q = 1$, solid green line) to an open system ($q = 0$, dotted red line). This behavior arises because the transmission coefficient is proportional to the line width function $\Gamma^\alpha(q)$; that is, as q tends to zero, the matrix elements connecting the leads and the TSCNs also tend to zero. Panel (b) corresponds to a closed system ($q = 1$), where one TSCN is in the long wire limit ($\varepsilon_{MB} = 0$), while in the other TSCN, the MZM coupling $\varepsilon_{MA} \geq 0$ is varied. This results in a Breit–Wigner resonance centered on $\mu = 0$, reaching the value $\mathcal{G} = e^2/h$. When $\varepsilon_{MA} \neq 0$, the electronic conductance consists of a central Breit–Wigner resonance and two lateral antiresonances located at $\mu = \pm\varepsilon_{MA}/\sqrt{2}$. In panel (c), we fix the MZM coupling $\varepsilon_{MA} = 0.6\Gamma$ and vary the coupling ε_{MB}. The electronic conductance exhibits an antiresonance at $\mu = 0$ and two lateral antiresonances at energies $\mu = \pm(\varepsilon_{MA} + \varepsilon_{MB})/2$ when $\varepsilon_{MB} \neq 0$, except in the symmetric case $\varepsilon_{MA(B)} = 0.6\Gamma$ (solid green line), where the two lateral antiresonances evolve into resonances at

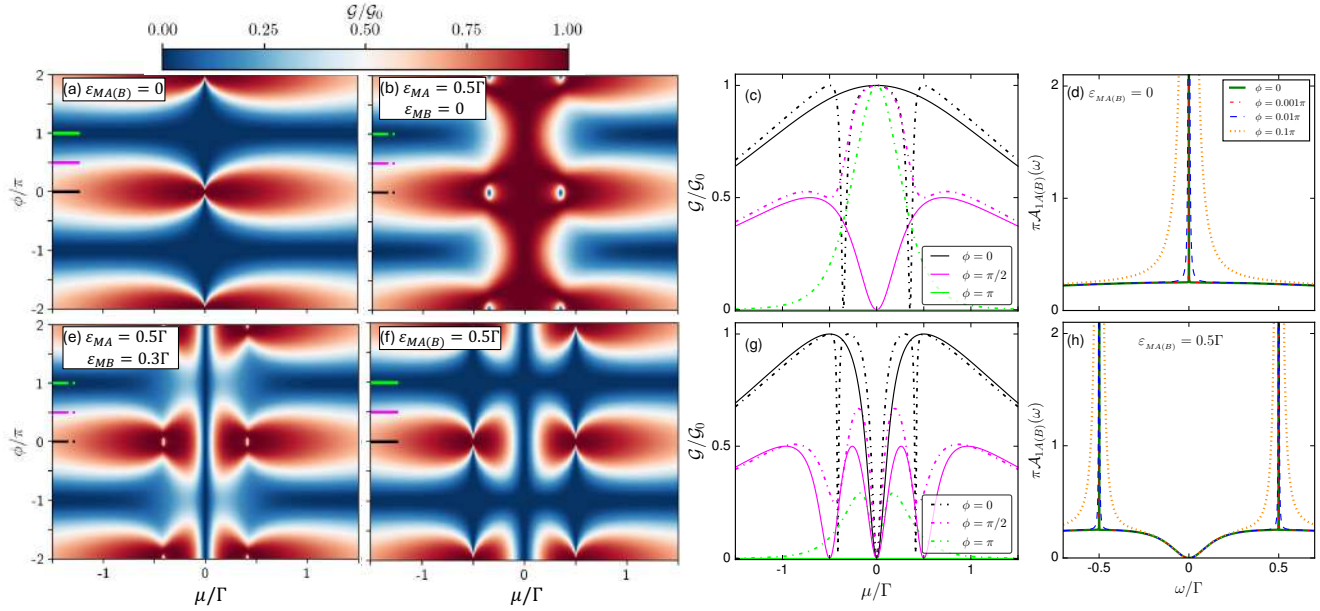

FIG. 3. Colormap of the electronic conductance $\mathcal{G}$ as a function of both the magnetic flux ϕ and the chemical potential μ, where red (blue) represents maximum (minimum) value for (a) $\varepsilon_{MA(B)} = 0$, (b) $\varepsilon_{MA} = 0.5\Gamma$ and $\varepsilon_{MB} = 0$, (e) $\varepsilon_{MA} = 0.5\Gamma$ and $\varepsilon_{MB} = 0.3\Gamma$, and (f) $\varepsilon_{MA(B)} = 0.5\Gamma$. In panel (c) and (g) we show the electronic conductance $\mathcal{G}$, as a function of the chemical potential μ, for specific values of the magnetic flux $\phi = \{0, \pi/2, \pi\}$ in black, magenta, and light green color, respectively. The solid (dash-dotted) line correspond to symmetrical (asymmetrical) configuration of the length of both TSCN, where $\varepsilon_{MA(B)} = 0$ ($\varepsilon_{MA(B)} = 0.5\Gamma$) and $\varepsilon_{MA} = 0.5\Gamma$ with $\varepsilon_{MB} = 0$ ($\varepsilon_{MA} = 0.5\Gamma$ with $\varepsilon_{MB} = 0.3\Gamma$), are shown in the top (bottom) panel. The spectral function $\mathcal{A}_{1A(B)}$ as a function of energy ω is shown in the panel (d) $\varepsilon_{MA(B)} = 0$ and (h) $\varepsilon_{MA(B)} = 0.5\Gamma$. We use specific values of the magnetic flux $\phi = \{0, 0.001\pi, 0.01\pi, 0.1\pi\}$ in solid green, dash-doted red, dashed blue, and dotted orange line, respectively.

$\mu = \pm 0.6\Gamma$. In panel (d), we show that the symmetric MZM-coupling configuration ($\varepsilon_{MA(B)} = 0.6\Gamma$), shown as the solid green line, gives rise to antiresonances at $\mu = \pm 0.6\Gamma$ when $q \neq 1$. We note that the position of these antiresonances is independent of the value of q, as they are centered at the system's eigenenergies, which are determined independently of q, as can be seen in Eq. (25).

We study the electronic transport in a closed system ($q = 1$) in the presence of a magnetic flux across the interferometer (i.e., $\phi \neq 0$). Figure 3 shows a colormap of the electronic conductance $\mathcal{G}$ as a function of the dimensionless magnetic flux ϕ and μ. In FIG. 3(a), we consider the long-wire limit for both TSCNs ($\varepsilon_{MA(B)} = 0$). At zero energy, the electronic conductance is $\mathcal{G} = e^2/h$ for $\phi = 2n\pi$ ($n \in \mathbf{Z}$), and drops to zero for $\phi \neq 2n\pi$, where the magnetic flux induces transport suppression over a wide range of values, reaching total reflection at $\phi = (2n-1)\pi$. Figure 3(b) shows the case with $\varepsilon_{MA} = 0.5\Gamma$ and $\varepsilon_{MB} = 0$. At zero energy, the electronic conductance remains $\mathcal{G} = e^2/h$ and is invariant under symmetry-breaking induced by the magnetic flux. Figure 3(e) shows $\mathcal{G}$ as a function of μ and ϕ for the case where both TSCNs are outside the long-wire limit, but with different lengths, i.e., $\varepsilon_{MA} = 0.5\Gamma$ and $\varepsilon_{MB} = 0.3\Gamma$. We observe that, regardless of the magnetic flux, the linear conductance exhibits an antiresonance at zero energy. For the particular case $\phi = 2n\pi$, two lateral antiresonances appear at $\mu = \pm(\varepsilon_{MA} + \varepsilon_{MB})/2$. Figure 3(f) shows the electronic conductance $\mathcal{G}$ for the case where both TSCNs are outside the long-wire limit, i.e., $\varepsilon_{MA} = \varepsilon_{MB} = 0.5\Gamma$. Again, the linear conductance displays an antiresonance at zero energy, independent of the magnetic flux. The suppression of transport as a function of μ is recovered—similar to the behavior in Fig. 3(a)—for values $\phi = (2n-1)\pi$. This behavior appears only for symmetric configurations of the MZM couplings, i.e., when $\varepsilon_{MA} = \varepsilon_{MB}$. Figures 3(c) and 3(g) show the electronic conductance $\mathcal{G}$ as a function of μ for fixed values of the magnetic flux: $\phi = 0$, $\phi = \pi/2$, and $\phi = \pi$, represented by black, magenta, and light green lines, respectively. The solid (dash-dotted) lines correspond to symmetric (asymmetric) configurations of the MZMs couplings. We observe the phenomenon of total reflection ($\mathcal{G} = 0$) in the symmetric case $\varepsilon_{MA} = \varepsilon_{MB}$ for $\phi = \pi$ (solid light green line in both panels), which is an energy-independent behavior. Figures 3(d) and 3(h) display the spectral functions $\mathcal{A}_{1\beta}$ as a function of the energy ω for magnetic flux values $\phi = 0$, $\pi/1000$, $\pi/100$, and $\pi/10$, shown in green (solid line), red (dash-dotted line), blue (dashed line), and orange (dotted line), respectively. For a symmetric configuration of the MZMs coupling ($\varepsilon_{MA} = \varepsilon_{MB}$), we find $\mathcal{A}_{1A} = \mathcal{A}_{1B}$, with parameters [panel (d)] $\varepsilon_{MA(B)} = 0$

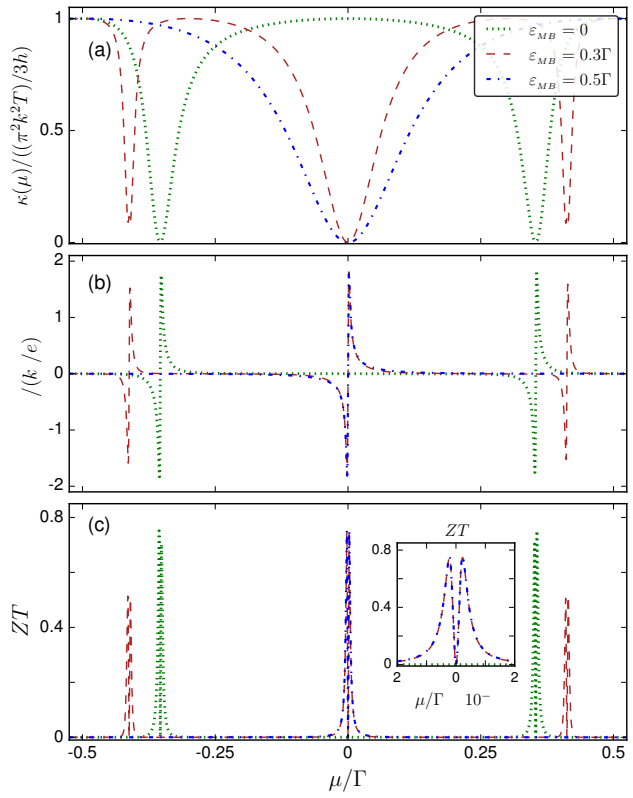

FIG. 4. Thermal quantities as a function of chemical potential μ. We show the (a) thermal conductance κ, (b) Seebeck coefficient S, and (c) figure of merit ZT, for the cases $\varepsilon_{MB} = 0$ (dotted green line), $\varepsilon_{MB} = 0.3\Gamma$ (dashed red line), and $\varepsilon_{MB} = 0.5\Gamma$ (dash-dotted blue line), with $\varepsilon_{MA} = 0.5\Gamma$ and $\phi = 0$ for all panels.

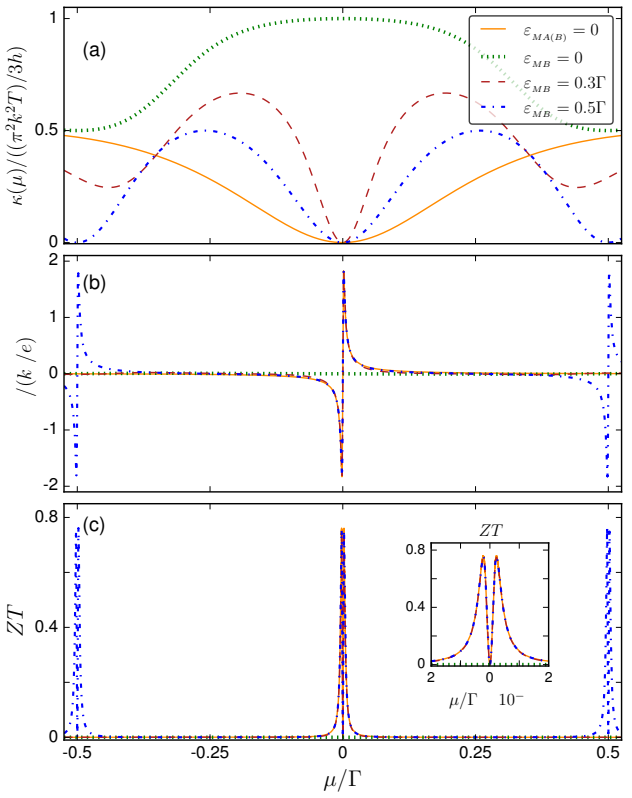

FIG. 5. Thermal quantities as a function of chemical potential μ. We show the (a) thermal conductance κ, (b) Seebeck coefficient S, and (c) figure of merit ZT, for the cases $\varepsilon_{MA(B)} = 0$ (solid orange line), $\varepsilon_{MB} = 0$ (dotted green line), $\varepsilon_{MB} = 0.3\Gamma$ (dashed red line), and $\varepsilon_{MB} = 0.5\Gamma$ (dash-dotted blue line), with $\varepsilon_{MA} = 0.5\Gamma$ for (b)-(d), and magnetic flux $\phi = \pi/2$ in all panels.

and [panel (h)] $\varepsilon_{MA(B)} = 0.5\Gamma$. In the long-wire limit ($\varepsilon_{MA(B)} = 0$), shown in Fig. 3(d), we observe a zero-width resonance localized at $\omega = 0$ for $\phi = 0$ (solid green line), corresponding to a true BIC, since these states do not contribute to the electronic conductance $\mathcal{G}$. These states acquire a finite width as the magnetic flux increases ($\phi \neq 0$), becoming quasi-BICs and contributing to the transmission in the form of antiresonances. In Fig. 3(h), we consider the case where both TSCNs have finite and equal lengths ($\varepsilon_{MA(B)} = 0.5\Gamma$). For $\phi = 0$, we obtain two symmetric lateral BICs located at $\omega = \pm\varepsilon_{MA(B)} = \pm 0.5\Gamma$, in agreement with Eq. (25). These states do not have projections in the electronic conductance, as shown in Fig. 3(g) for $\phi = 0$. When $\phi \neq 0$, the two symmetric lateral BICs in the spectral function acquire a finite width, thus becoming quasi-BICs.

We now focus our attention on the thermoelectric properties of the system. Figure 4 shows the [panel (a)] thermal conductance κ, [panel (b)] Seebeck coefficient S, and [panel (c)] figure of merit ZT as functions of μ, in the absence of magnetic flux ($\phi = 0$). We fix $\varepsilon_{MA} = 0.5\Gamma$, and the second TSCN takes the values $\varepsilon_{MB} = 0$ (dotted green line), $\varepsilon_{MB} = 0.3\Gamma$ (dashed red line), and $\varepsilon_{MB} = 0.5\Gamma$ (dash-dotted blue line). The thermal conductance in Fig. 4(a) exhibits a behavior similar to that of the electronic conductance (see, for instance, Fig. 3), where resonances and antiresonances depend on the MZM couplings of each TSCN. The cases with $\varepsilon_{MB} = 0$, $\varepsilon_{MB} = 0.3\Gamma$, and $\varepsilon_{MB} = 0.5\Gamma$ correspond to the dash-dotted black line in Fig. 3(c), the dash-dotted black line in Fig. 3(g), and the solid black line in Fig. 3(g), respectively. The Seebeck coefficient is shown in Fig. 4(b), and is an odd function of μ. The changes in S, from minimum to maximum, are centered at $\mu = \pm\varepsilon_{MA}/\sqrt{2}$ (dotted green line), $\mu = 0$ and $\mu = \pm(\varepsilon_{MA} + \varepsilon_{MB})/2$ (dashed red line), and $\mu = 0$ (dash-dotted blue line), which coincide with the positions of antiresonances in the thermal conductance shown in Fig. 4(a). The thermoelectric efficiency is characterized by the extrema of the figure of merit, ZT, shown in Fig. 4(c). We observe that the maxima of ZT appear in pairs and are centered at the same energies as those found in the thermopower and thermal conductance. In the inset, we show a zoomed view where the maxima of ZT exhibit a symmetric behavior centered at $\mu = 0$.

At this point, we can express that the thermoelectric properties of the system are strongly influenced by the coupling between the MZMs in each TSCN. The location of resonances and antiresonances in the electronic and thermal conductances correlates with features in the Seebeck coefficient and thermoelectric efficiency. In particular, symmetric configurations of MZM couplings lead to well-defined antiresonances and enhanced thermoelectric response.

Figure 5 shows the [panel (a)] thermal conductance κ, [panel (b)] Seebeck coefficient S, and [panel (c)] figure of merit ZT as functions of μ, in the presence of magnetic flux ($\phi = \pi/2$). We first present the case $\varepsilon_{MA(B)} = 0$ (solid orange line). Then, we fix $\varepsilon_{MA} = 0.5\Gamma$ and vary the second TSCN coupling as $\varepsilon_{MB} = 0$ (dotted green line), $\varepsilon_{MB} = 0.3\Gamma$ (dashed red line), and $\varepsilon_{MB} = 0.5\Gamma$ (dash-dotted blue line). The thermal conductance in Fig. 5(a) exhibits behavior similar and proportional to that of the electronic conductance. We observe this correspondence in Figs. 3(c) and 3(g), where the solid and dash-dotted magenta lines represent symmetric and asymmetric MZM-coupling configurations, respectively. As before, the positions of resonances and antiresonances depend on the MZMs couplings of each TSCN. The Seebeck coefficient is shown in Fig. 5(b), and is an odd function of the chemical potential μ. The variations in S, from minimum to maximum, are centered at $\mu = \pm\varepsilon_{MA(B)}$ and $\mu = 0$ (dash-dotted blue line), and at $\mu = 0$ for the solid orange and dashed red lines. These positions coincide with the locations of antiresonances in the thermal conductance shown in Fig. 5(a). The maxima of ZT appear in pairs [Fig. 5(c)], and are centered at the same energies as those observed in the thermopower and thermal conductance. In the inset, a zoomed view reveals that the maxima of ZT exhibit a symmetric behavior centered at $\mu = 0$. We observe that the BICs present in the system for $\phi = 0$ do not affect the thermoelectric quantities. However, when $\phi \neq 0$, these BICs are destroyed and become quasi-BICs, which enhance the thermoelectric efficiency. This effect is particularly evident in Fig. 5(c) for the cases $\varepsilon_{MA(B)} = 0$ (solid orange line) and $\varepsilon_{MA(B)} = 0.5\Gamma$ (dash-dotted blue line).

In Fig. 6 we study the fulfillment of the WF law by plotting the Lorenz ratio $\mathcal{L}$ in units of the Lorenz number $\mathcal{L}_0$, as a function of chemical potential μ. The panel 6(a) shows the cases $\varepsilon_{MB} = 0$ (dotted green line), $\varepsilon_{MB} = 0.3\Gamma$ (dashed red line) and $\varepsilon_{MB} = 0.5\Gamma$ (dashed-dotted blue line), with $\varepsilon_{MA} = 0.5\Gamma$ and $\phi = 0$. The Lorenz ratio $\mathcal{L} = \kappa/\mathcal{G}T = \mathcal{L}_0$ for almost all values of μ, however $\mathcal{L}$ deviates from $\mathcal{L}_0$ around $\mu = \{0, \pm\varepsilon_{MA}/\sqrt{2}, \pm(\varepsilon_{MA} + \varepsilon_{MB})/2\}$, where $\mathcal{L}$ reaches the maximum $\mathcal{L}_{max} = 4.19\mathcal{L}_0$. Fig. 6(b) is a zoom of Fig. 6(a) centered at $\mu = 0$. We can observe from Eq. (19), that the expansion for the integral L_1 contains only odd derivatives of the transmission $\mathcal{T}$, which is dominated by the term proportional to $\mathcal{T}^{(1)}$, which vanishes at the antiresonance energy. As a result of this, the thermal conductance has a small peak in the antiresonance region due to the term L_1^2/L_0, in Eq. (16), it

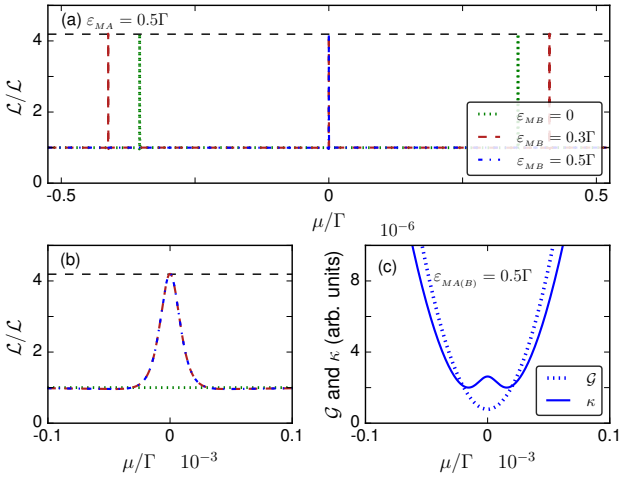

FIG. 6. We show (a) Lorenz ratio $\mathcal{L}$ as a function of μ, for the cases $\varepsilon_{MB} = 0$ (dotted green line), $\varepsilon_{MB} = 0.3\Gamma$ (dashed red line), and $\varepsilon_{MB} = 0.5\Gamma$ (dash-dotted blue line), with $\varepsilon_{MA} = 0.5\Gamma$ and $\phi = 0$ for all panels. The horizontal dashed black line corresponds to the universal maximum value of $4.19\mathcal{L}_0$. In panel (b) we show a zoom of panel (a) centered at $\mu = 0$. In panel (c) we plot both conductances ($\mathcal{G}$ and κ, in arbitrary units) for the case $\varepsilon_{MA(B)} = 0.5\Gamma$, in the same energy range that in panel (b).

falls to zero, while the electronic conductance $\mathcal{G}$ presents a single minimum, as can be seen in panel 6(c). Both curves present different shapes in a small region around the antiresonance energy, which results in the violation of the WF law.

IV. SUMMARY

We studied a system composed of two normal leads coupled to two TSCNs, each hosting MZMs at their ends, arranged in an interferometer configuration. We focused on the electronic and thermal conductances between the leads, as well as on the spectral functions of the MZMs and thermoelectric quantities. The latter were obtained using the GF formalism, while thermoelectric properties were calculated via the Sommerfeld expansion. We reported the phenomenon of total reflection at magnetic flux values $\phi = (2n-1)\pi$ for symmetric MZM-coupling configurations, that is, when both TSCNs have the same length. In addition, for magnetic flux values $\phi = 2n\pi$, we identified the formation of BICs, characterized by zero-width resonances in the spectral functions. These states also emerge under symmetric MZM coupling and behave as ghost Fano-Majorana anomalies, since they do not contribute to the electronic conductance. We also found that these BICs are destroyed as the magnetic flux deviates from $\phi = 2n\pi$. For $\phi \neq 0$, the BICs acquire a finite width, becoming quasi-BICs, and manifest themselves as antiresonances in both electronic and thermal conduc-

tances at the same characteristic energies. These results demonstrate that BICs in the system can be controlled via the external magnetic flux, and their transformation into quasi-BICs leads to enhancements in thermopower S and thermoelectric figure of merit ZT, by means of a violation of the WF law.

ACKNOWLEDGMENTS

A.P.G. is grateful for the funding of scholarship ANID-Chile No. 21210410 and FONDECYT grant 1201876. D.Z. acknowledges support from USM-Chile under Grant PI-LIR-2022-13. J.P.R.-A is grateful for the financial support of FONDECYT Iniciación grant No. 11240637. P.A.O. acknowledges support from FONDECYT grants 1201876 and 1220700.

DATA AVAILABILITY STATEMENT

Data will be made available on reasonable request.

CONFLICTS OF INTEREST

The authors decl are that they have no conflict of interest.

AUTHOR CONTRIBUTION STATEMENT

All authors contributed equally and significantly in writing this article. All authors read and approved the final manuscript.

Appendix A: Green function

The full Green function is obtained from Eq. (8), in the form

$$\mathbf{G}^r = \frac{1}{D}\begin{pmatrix} G_{11} & G_{12} & -K\omega^2 & -iK\varepsilon_{_{MB}}\omega \\ G_{21} & G_{22} & iK\varepsilon_{_{MA}}\omega & -K\varepsilon_{_{MA}}\varepsilon_{_{MB}} \\ -K\omega^2 & -iK\varepsilon_{_{MA}}\omega & G_{33} & G_{34} \\ iK\varepsilon_{_{MB}}\omega & -K\varepsilon_{_{MA}}\varepsilon_{_{MB}} & G_{43} & G_{44} \end{pmatrix}, \tag{A1}$$

with the matricial elements

$$G_{11(33)} = -\omega\left[\varepsilon^2_{_{MB(A)}} - i\left[\sum_\alpha \Gamma^\alpha_{B(A)}\right]\omega - \omega^2\right], \tag{A2}$$

$$G_{22(44)} = -\varepsilon^2_{_{MB(A)}}\left[i\sum_\alpha \Gamma^\alpha_{A(B)} + \omega\right] - \omega K^2 + \omega\left[i\sum_\alpha \Gamma^\alpha_{A} + \omega\right]\left[i\sum_\alpha \Gamma^\alpha_{B} + \omega\right], \tag{A3}$$

$$G_{12} = -G_{21} = -i\varepsilon_{_{MA}}\left[\varepsilon^2_{_{MB}} - i\sum_\alpha \Gamma^\alpha_B\omega - \omega^2\right], \tag{A4}$$

$$G_{34} = -G_{43} = -i\varepsilon_{_{MB}}\left[\varepsilon^2_{_{MA}} - i\sum_\alpha \Gamma^\alpha_A\omega - \omega^2\right], \tag{A5}$$

and the denominator D,

$$D = \left[\varepsilon^2_{_{MA}} - i\sum_\alpha \Gamma^\alpha_A + \omega\right]\left[\varepsilon^2_{_{MB}} - i\sum_\alpha \Gamma^\alpha_B + \omega\right] - K^2\omega^2\,. \tag{A6}$$

[1] A. Y. Kitaev, Ann. Phys. **303**, 2 (2003).
[2] C. Nayak, S. H. Simon, A. Stern, M. Freedman, and S. D. Sarma, Rev. Mod. Phys. **80**, 1083 (2008).
[3] J. K. Pachos, *Introduction to topological quantum com-*

putation (Cambridge University Press, 2012).
[4] C. W. J. Beenakker, Annu. Rev. Condens. Matter Phys. **4**, 113 (2013).
[5] C. Laflamme, M. Baranov, P. Zoller, and C. Kraus, Phys. Rev. A **89**, 029903 (2014).
[6] S. M. Albrecht, A. P. Higginbotham, M. Madsen, F. Kuemmeth, T. S. Jespersen, J. Nygård, P. Krogstrup, and C. Marcus, Nature **531**, 206 (2016).
[7] E. Majorana, Nuovo Cimento **14**, 171 (1937).
[8] F. Wilczek, Nat. Phys. **5**, 614 (2009).
[9] M. Franz, Physics **3**, 24 (2010).
[10] C. V. Kraus, M. Dalmonte, M. A. Baranov, A. M. Läuchli, and P. Zoller, Phys. Rev. Lett. **111**, 173004 (2013).
[11] J. Alicea, Y. Oreg, G. Refael, F. Von Oppen, and M. Fisher, Nat. Phys. **7**, 412 (2011).
[12] A. Y. Kitaev, Phys.-usp. **44**, 131 (2001).
[13] S. B. Bravyi and A. Y. Kitaev, Ann. Phys. **298**, 210 (2002).
[14] M. Leijnse and K. Flensberg, Phys. Rev. Lett. **107**, 210502 (2011).
[15] J. Moore, Nat. Phys. **5**, 378 (2009).
[16] B. Wu and J. Cao, Phys. Rev. B **85**, 085415 (2012).
[17] G. W. Semenoff and P. Sodano, arXiv:cond-mat/0601261 (2006).
[18] S. Tewari, C. Zhang, S. D. Sarma, C. Nayak, and D.-H. Lee, Phys. Rev. lett. **100**, 027001 (2008).
[19] V. Mourik, K. Zuo, S. M. Frolov, S. Plissard, E. P. Bakkers, and L. P. Kouwenhoven, Science **336**, 1003 (2012).
[20] M. Deng, C. Yu, G. Huang, M. Larsson, P. Caroff, and H. Xu, Nano lett. **12**, 6414 (2012).
[21] A. Das, Y. Ronen, Y. Most, Y. Oreg, M. Heiblum, and H. Shtrikman, Nat. Phys. **8**, 887 (2012).
[22] E. J. H. Lee, X. Jiang, R. Aguado, G. Katsaros, C. M. Lieber, and S. De Franceschi, Phys. Rev. lett. **109**, 186802 (2012).
[23] A. Finck, D. Van Harlingen, P. Mohseni, K. Jung, and X. Li, Phys. Rev. Lett. **110**, 126406 (2013).
[24] H. Churchill, V. Fatemi, K. Grove-Rasmussen, M. Deng, P. Caroff, H. Xu, and C. M. Marcus, Phys. Rev. B **87**, 241401 (2013).
[25] D. Zambrano, J. P. Ramos-Andrade, and P. Orellana, J. Phys. Condens. Matter **30**, 375301 (2018).
[26] J. P. Ramos-Andrade, D. Zambrano, and P. A. Orellana, Ann. Phys. (Berlin) **531**, 1800498 (2019).
[27] L. W. Molenkamp, T. Gravier, H. van Houten, O. J. A. Buijk, M. A. A. Mabesoone, and C. T. Foxon, Phys. Rev. Lett. **68**, 3765 (1992).
[28] H. van Houten, L. W. Molenkamp, C. W. J. Beenakker, and C. T. Foxon, Semiconductor Science and Technology **7**, B215 (1992).
[29] L. Fu and C. L. Kane, Phys. Rev. Lett. **100**, 096407 (2008).
[30] A. G. Bauer, B. Scharf, L. W. Molenkamp, E. M. Hankiewicz, and B. Sothmann, Phys. Rev. B **104**, L201410 (2021).
[31] P. E. Dolgirev, M. S. Kalenkov, and A. D. Zaikin, physica status solidi (RRL)–Rapid Research Letters **13**, 1800252 (2019).
[32] C.-Y. Hou, K. Shtengel, and G. Refael, Phys. Rev. B **88**, 075304 (2013).
[33] E. Sela, Y. Oreg, S. Plugge, N. Hartman, S. Lüscher, and J. Folk, Phys. Rev. Lett. **123**, 147702 (2019).
[34] D. Giuliano, A. Nava, R. Egger, P. Sodano, and F. Buccheri, Phys. Rev. B **105**, 035419 (2022).
[35] F. Buccheri, A. Nava, R. Egger, P. Sodano, and D. Giuliano, Phys. Rev. B **105**, L081403 (2022).
[36] C. Benjamin and R. Das, Europhysics Letters **146**, 16006 (2024).
[37] D. I. Pikulin, B. van Heck, T. Karzig, E. A. Martinez, B. Nijholt, T. Laeven, G. W. Winkler, J. D. Watson, S. Heedt, M. Temurhan, *et al.*, arXiv preprint arXiv:2103.12217 (2021).
[38] M. Aghaee, A. Akkala, Z. Alam, R. Ali, A. Alcaraz Ramirez, M. Andrzejczuk, A. E. Antipov, P. Aseev, M. Astafev, B. Bauer, *et al.*, Physical Review B **107**, 245423 (2023).
[39] D. Aasen, M. Aghaee, Z. Alam, M. Andrzejczuk, A. Antipov, M. Astafev, L. Avilovas, A. Barzegar, B. Bauer, J. Becker, *et al.*, arXiv preprint arXiv:2502.12252 (2025).
[40] C. W. Hsu, B. Zhen, A. D. Stone, J. D. Joannopoulos, and M. Soljačić, Nat. Rev. Mater. **1**, 1 (2016).
[41] J. von Neumann and E. P. Wigner, Z. Phys. **30**, 465 (1929).
[42] J. P. Ramos and P. A. Orellana, Phys. B: Condens. Matter **455**, 66 (2014).
[43] B. Grez, J. Ramos-Andrade, V. Juričić, and P. Orellana, Phys. Rev. A **106**, 013719 (2022).
[44] A. Garrido, D. Zambrano, J. Ramos-Andrade, and P. Orellana, The European Physical Journal Plus **138**, 1 (2023).
[45] D. A. Ruiz-Tijerina, E. Vernek, L. G. G. V. Dias da Silva, and J. C. Egues, Phys. Rev. B **91**, 115435 (2015).
[46] C. J. Vineis, A. Shakouri, A. Majumdar, and M. G. Kanatzidis, Advanced materials **22**, 3970 (2010).
[47] J. Nagamatsu, N. Nakagawa, T. Muranaka, Y. Zenitani, and J. Akimitsu, nature **410**, 63 (2001).

Chapter 4

Majorana edge and end states in planar Josephson junctions

Proximitized planar Josephson Junctions (JJs) have recently emerged as promising platforms for creating and manipulating Majorana states (MSs) [57, 23, 58, 27, 59–62, 3, 29, 63–70, 28, 71–78]. In addition to the experimental advances in building such structures, proximitized planar JJs have also been shown to possess an enhanced parameter space supporting the topological superconducting state [23, 79].

4.1 BdG Hamiltonian

The Bogoliubov-de Gennes (BdG) Hamiltonian provides the fundamental framework for describing quasiparticle excitations in superconductors within the Bardeen-Cooper-Schrieffer (BCS) theory. This matrix Hamiltonian takes the general form,

$$\hat{H}_{\mathrm{BdG}} = \begin{pmatrix} \hat{H}_0 & \Delta e^{i\phi_{\mathrm{SC}}} \\ \Delta e^{-i\phi_{\mathrm{SC}}} & -\hat{T}^{-1}\hat{H}_0\hat{T} \end{pmatrix}, \tag{4.1}$$

where $\hat{H}_0$ represents the single-particle electron Hamiltonian, Δ denotes the superconducting gap parameter originating from the BCS mean-field approximation, $-\hat{T}^{-1}\hat{H}_0\hat{T}$ corresponds to the time-reversed hole sector, and ϕ_{SC} describe the superconducting phase difference across the junction.

The realization of topological superconductivity (TS) in JJs requires three essential physical ingredients encoded in the BdG Hamiltonian:

- Proximity-induced superconductivity manifests through the off-diagonal pairing terms $\Delta e^{\pm i\phi_{\mathrm{SC}}}$, which couple the electron and hole sectors.

				δ							
Class	T	C	S	0	1	2	3	4	5	6	7
A	0	0	0	$\mathbb{Z}$	0	$\mathbb{Z}$	0	$\mathbb{Z}$	0	$\mathbb{Z}$	0
AIII	0	0	1	0	$\mathbb{Z}$	0	$\mathbb{Z}$	0	$\mathbb{Z}$	0	$\mathbb{Z}$
AI	+	0	0	$\mathbb{Z}$	0	0	0	$2\mathbb{Z}$	0	$\mathbb{Z}_2$	$\mathbb{Z}_2$
BDI	+	+	1	$\mathbb{Z}_2$	$\mathbb{Z}$	0	0	0	$2\mathbb{Z}$	0	$\mathbb{Z}_2$
D	0	+	0	$\mathbb{Z}_2$	$\mathbb{Z}_2$	$\mathbb{Z}$	0	0	0	$2\mathbb{Z}$	0
DIII	−	+	1	0	$\mathbb{Z}_2$	$\mathbb{Z}_2$	$\mathbb{Z}$	0	0	0	$2\mathbb{Z}$
AII	−	0	0	$2\mathbb{Z}$	0	$\mathbb{Z}_2$	$\mathbb{Z}_2$	$\mathbb{Z}$	0	0	0
CII	−	−	1	0	$2\mathbb{Z}$	0	$\mathbb{Z}_2$	$\mathbb{Z}_2$	$\mathbb{Z}$	0	0
C	0	−	0	0	0	$2\mathbb{Z}$	0	$\mathbb{Z}_2$	$\mathbb{Z}_2$	$\mathbb{Z}$	0
CI	+	−	1	0	0	0	$2\mathbb{Z}$	0	$\mathbb{Z}_2$	$\mathbb{Z}_2$	$\mathbb{Z}$

Fig. 4.1 Periodic table of topological insulators and superconductors: $\delta = d - D$, where d is the space dimension and $D+1$ is the codimension of defects; The leftmost column (A, AIII, ..., C, CI) enumerates the symmetry classes of fermionic Hamiltonians, classified by the presence or absence of time-reversal (T), particle-hole (C), and chiral (S) symmetries. These symmetries are encoded numerically: a nonzero value ($+1$ or -1) indicates the presence of a symmetry, with the sign corresponding to the square of its operator (e.g., $T^2 = +1$ in the BDI class), while 0 denotes its absence. The entries—$\mathbb{Z}$, $\mathbb{Z}_2$, $2\mathbb{Z}$, and 0—classify the distinct topological phases possible within each symmetry class and dimension. A nonzero entry ($\mathbb{Z}$, $\mathbb{Z}_2$, or $2\mathbb{Z}$) indicates the existence of nontrivial topological insulators, superconductors, or defects, with the algebraic structure denoting the type of invariant (integer, binary, or even integer, respectively), and 0 corresponds to a trivial classification. The case of $D = 0$ (i.e., $\delta = d$) corresponds to the tenflod classification of gapped bulk topological insulators and superconductors. [8]

- Zeeman splitting induced by an external magnetic field.
- Spin-orbit coupling (SOC) introduces the necessary spin-momentum locking that, when combined with the other components, can effectively emulate p-wave pairing.

These ingredients creates the conditions for TS, by opening a gap in the energy spectrum. The interplay between these elements leads to the formation of Majorana zero modes (MZMs) at the opposite ends of the junction.

To solve the BdG-Hamiltonian in Eq. 4.1, we employ numerical techniques described in Appendix A (finite-difference method, and Tight-Binding approximation).

4.2 Symmetry classes and topological phases

The classification of a system's topological phases is determined by identifying its topological invariants, which depend crucially on the presence or absence of three fundamental symmetries: time-reversal (T), charge-conjugation (C), and chiral symmetry (S) [8]. Each symmetry class is uniquely defined by (1) which of these symmetries the system preserves, and (2) their symmetry operator (O) properties, specifically, their operators' square values (i.e., $O^2 = \pm 1$) [See Fig. 4.1].

For this work, the BDI and D symmetry classes (for $\delta = 1$) are the main focus. Because symmetries are linked to conserved properties (such as parity and momentum) of a system, the symmetry classification can be used as a guide for identifying the appropriate topological invariant. For the D symmetry class, the topological invariant turns out to be the $\mathbb{Z}_2$ index, also called the topological charge Q, this can take the values 1 and -1 for trivial and topological states, respectively. The topological invariant for the BDI class is the $\mathbb{Z}$ invariant, which can take integer values. The topological charge (or $\mathbb{Z}_2$ index) of the D class, is simply the parity of the BDI $\mathbb{Z}$ index.

4.3 Outline

In the following paper, we investigated the formation and properties of edge-like and end-like MSs in proximitized planar JJs subjected to an in-plane magnetic field, considering the effects of Rashba and/or Dresselhaus SOCs. The end-like MSs are primarily localized at opposite ends of the normal region within the junction. In contrast, the edge-like MSs extend along the system's edges, perpendicular to the junction. To characterize the nature and protection of the MSs we introduced a quantity called the topological gap character. This quantity simultaneously characterizes three key properties: (1) the existence of a topological superconducting phase, (2) the magnitude of the topological gap, and (3) the spatial nature of Majorana zero modes (end-like or edge-like).

Majorana edge and end states in planar Josephson junctions

A. P. Garrido,[1,2,*] P. A. Orellana,[1] and A. Matos-Abiague[2]

[1] *Department of Physics, Technical University Federico Santa María, Valparaiso, Valparaiso 2390123, Chile.*
[2] *Department of Physics and Astronomy, Wayne State University, Detroit, Michigan 48201, USA.*

(Dated: February 25, 2025)

We theoretically investigate the localization properties of Majorana states (MSs) in proximitized, planar Josephson Junctions (JJs) oriented along different crystallographic orientations and in the presence of an in-plane magnetic field and Rashba and Dresselhaus spin-orbit couplings. We show that two types of MSs may emerge when the junction transits into the topological superconducting state. In one case, referred to as end-like MSs, the Majorana quasiparticles are mainly localized inside the normal region at the opposite ends of the junction. In contrast, edge-like MSs extend along the opposite edges of the system, perpendicular to the junction channel. We show how the MSs can transit from end-like to edge-like and vice versa by tuning the magnetic field strength and/or the superconducting phase difference across the junction. In the case of phase-unbiased JJs the transition may occur as the ground state phase difference self-adjusts its value when the Zeeman field is varied.

I. INTRODUCTION

Majorana states (MSs) are zero-energy quasiparticle excitations predicted to appear localized at the boundaries of topological superconductors (TSCs) [1–6]. The MSs obey a non-Abelian exchange statistic, which makes them promising candidates for realizing robust qubits with potential applications in fault-tolerant quantum computing [7–10].

Topological superconductivity (TS) can be engineered by using semiconductor nanowires with large spin-orbit coupling (SOC) and proximitized by s-wave superconductors [11–21], proximitized systems exposed to magnetic textures [22–32], and magnetic chains on s-wave superconductors [33–38]. Proximitized planar JJs have recently emerged as promising platforms for creating and manipulating MSs [39–65]. In addition to the experimental advances in building such structures, proximitized planar JJs have also been shown to possess an enhanced parameter space supporting the topological superconducting state [40, 66].

Magnetic and crystalline anisotropic effects have been predicted to appear in the Josephson junction with noncentrosymmetric materials [67–70]. In particular, it has been shown that in the presence of SOC the Zeeman interaction yields a strong dependence of the system properties on the magnetic field direction. Furthermore, in systems with Rashba [71] and Dresselhaus [72] SOCs the crystallographic orientation can affect the topological superconducting state, its robustness, and signatures [67, 68, 73].

Most previous investigations of TS in planar JJs have focused on *end* MSs, i.e., MSs that localize at the opposite ends of the junction with short localization lengths both along the junction ($\hat{y}$ direction, as shown in Fig. 1) and along the system edges perpendicular to the junction ($\hat{x}$ direction, as shown in Fig. 1) [53, 57, 67, 68, 74]. However, theoretical evidence of the existence of *edge* MSs (i.e., MSs that are localized along the junction direction but spread along the entire system edges perpendicular to the junction) has been provided in previous works [46, 67, 75]. The formation of MSs exhibiting anomalous multilocality in three-terminal Josephson junctions has also been proposed [76]. Besides JJs, Majorana edge states can also emerge in hybrid superconductor/ferromagnet structures with helical magnetic textures [77]. Moreover, two-dimensional structures, typically associated with quantum anomalous Hall systems coupled to superconductors, have been shown to support chiral Majorana edge states [78–80] flowing around the sample edges in opposite directions and Majorana corner modes localized at vertices [81–83].

In this work, we study the formation and properties of edge-like and end-like MSs in proximitized planar JJs and characterize them by introducing a quantity (here referred to as the topological gap character) that contains information about the topological charge, topological gap, and the localization nature of the zero-energy states. The norm of the topological gap character determines the size of the topological gap relative to the proximity-induced superconducting gap, and its sign indicates whether the system is in a TS state with *edge*-like (positive sign) or *end*-like (negative sign) MSs. We analyze how the localization character of MSs depends on relevant system parameters such as the magnetic field strength and direction, the superconducting phase difference across the junction, the SOC strength, and the junction crystallographic orientation. Moreover, our study reveals the possibility of inducing transitions from end-like to edge-like MSs (and vice versa) by tuning the magnetic field strength and/or the superconducting phase difference. In phase-unbiased JJs, the transition between end-like and edge-like MSs may occur as the ground state phase difference self-adjusts its value when the Zeeman field is varied. The paper is organized as follows. Section II presents the theoretical model and an overview of the relevant quantities used for characterizing the systems

* alejandro.garridoh@usm.cl

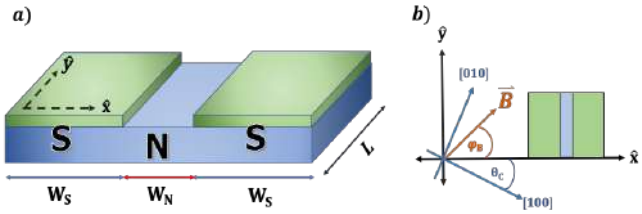

FIG. 1. (a) Schematic of a JJ consisting of a noncentrosymmetric semiconductor 2DEG (blue) in contact with two superconducting (S) leads (green). The $\hat{x}$ and $\hat{y}$ axes define the coordinate system in the junction's reference frame. A top gate (not shown) over the normal (N) region can be used to modulate the Rashba SOC strength [48, 84]. (b) Relevant angles in the junction coordinate system: φ_B defines the direction of the in-plane magnetic field ($\mathbf{B}$) with respect to the $\hat{x}$ axis, while θ_c determines the orientation of the junction reference frame with respect to the semiconductor's [100] crystallographic axis.

and the MSs. The numerical simulations and main results are discussed in Sec. III, while concluding remarks are given in Sec. IV.

II. THEORETICAL MODEL

We consider a planar JJ composed of a 2D electron gas (2DEG) formed in a noncentrosymmetric semiconductor and subject to an in-plane magnetic field B. The superconducting (S) regions are induced in the 2DEG by proximity to the superconducting cover layers, while the uncovered region remains in the normal (N) state [Fig. 1(a)]. Excitations in the JJ are described by the Bogoliubov-de Gennes (BdG) Hamiltonian,

$$H = \tau_z \otimes H_0 + \tau_0 \otimes \mathbf{E}_z \cdot \boldsymbol{\sigma} + \Delta(x)\tau_+ + \Delta^*(x)\tau_- \,, \quad (1)$$

where

$$H_0 = \left[\frac{\mathbf{p^2}}{2m^*} + V(x) - (\mu_S - \varepsilon)\right]\sigma_0 + \frac{\alpha}{\hbar}(p_y\sigma_x - p_x\sigma_y) + \frac{\beta}{\hbar}\left[(p_x\sigma_x - p_y\sigma_y)\cos 2\theta_c - (p_x\sigma_y + p_y\sigma_x)\sin 2\theta_c\right]. \quad (2)$$

Here σ_0 and τ_0 are unit matrices, $\sigma_{x,y,z}$ and $\tau_{x,y,z}$ denote the Pauli matrices in particle-hole and spin spaces, respectively. The linear momentum is represented by $\mathbf{p}$, m^* is the electron effective mass, $\tau_\pm = (\tau_x \pm i\tau_y)\otimes\sigma_0/2$, and $V(x) = (\mu_S - \mu_N)\Theta(W_N/2 - |x|)$ describes the difference between the chemical potentials in the N (μ_N) and S (μ_S) regions. The Rashba and Dresselhaus SOC strengths are represented by α and β, respectively. The angle θ_c characterizes the orientation of the junction with respect to the crystallographic direction [100] of the semiconductor [Fig. 1-(b)]. The chemical potentials are measured with respect to the minimum of the single-particle energies, $\varepsilon = m^*\lambda^2(1 + |\sin 2\theta_c|)/2\hbar^2$. Here we use the SOC parametrization,

$$\alpha = \lambda\cos\theta_{so},\ \beta = \lambda\sin\theta_{so},\ \lambda = \sqrt{\alpha^2+\beta^2}\,, \quad (3)$$

where λ represents the overall strength of the combined Rashba and Dresselhaus SOCs, while the spin-orbit angle,

$$\theta_{so} = \mathrm{arccot}(\alpha/\beta)\,. \quad (4)$$

characterizes the relative strength between them.

The second term in Eq. (1) corresponds to the Zeeman interaction and is determined by the vector,

$$\mathbf{E}_z = -\frac{g^*\mu_B B}{2}\,(\cos\varphi_B,\ \sin\varphi_B,\ 0)^T\,. \quad (5)$$

with g^*, μ_B, B, and φ_B representing the effective g-factor, the Bohr magneton, the magnetic field strength, and the magnetic field direction, respectively. In what follows, we use $E_Z = g^*\mu_B B/2$ to denote the amplitude of the Zeeman energy. The spatial dependence of the superconducting gap is,

$$\Delta(x) = \Delta_0\, e^{i\,\mathrm{sgn}(x)\phi/2}\Theta(|x| - W_N/2)\,, \quad (6)$$

where ϕ is the phase difference across the JJ and Δ_0 is the magnitude of the proximity-induced superconducting gap.

A. Topological charge

To identify the topological regions we investigate how different sets of system parameters affect the topological invariants characterizing the junction. The presence of the magnetic field breaks the time-reversal invariance and the system generically belongs to the D class, characterized by the topological charge (i.e., the $\mathbb{Z}_2$ topological index),

$$Q = \mathrm{sgn}\left[\frac{\mathrm{Pf}\{H(k_y=\pi)\tau_y\otimes\sigma_y\}}{\mathrm{Pf}\{H(k_y=0)\tau_y\otimes\sigma_y\}}\right], \quad (7)$$

where Pf{...} denotes the Pfaffian [85–88]. The topological charge determines whether a system belonging to the D class is in a trivial ($Q = 1$) or topological ($Q = -1$) phase [89–94].

It is worth noting that under some conditions determined by the SOC field, the magnetic field direction, and the junction crystallographic orientation, symmetric junctions may effectively belong to the BDI class [67].

In such cases, the topological phases are characterized by the $\mathbb{Z}$ topological invariant of the BDI class. Since the topological charge Q is determined by the parity of the $\mathbb{Z}$ index, the topologically non-trivial regions of the BDI class consist of non-trivial D-class regions (composed of odd $\mathbb{Z}$ index subregions) enhanced by regions with even $\mathbb{Z}$ index [40, 43]. We found that the topological gap in BDI class regions with multiple pairs of MSs is relatively small in the systems considered here. Therefore, our investigation focuses on regions that support only a single pair of MSs. The extent of these regions can be determined by examining how the topological charge Q depends on the system parameters.

B. Topological gap

As the system transits into the topological state, MSs emerge as pairs of degenerate zero-energy states which are isolated from the rest of the excitation spectrum by the energy gap, Δ_{top}, referred to as the topological gap and defined as,

$$\Delta_{top} = (E_1 - E_0)\,. \tag{8}$$

Here E_0 and E_1 are the two lowest-energy states on the positive branch of the energy spectrum, respectively. Due to finite-size effects, the MSs localized at opposite ends (or edges) may overlap, so their energy ($\pm E_0$) may slightly deviate from zero. Note that Eq. (8) can only be interpreted as the topological gap when the system is in the TS state.

In the topological superconducting (TS) state, the topological gap protects the Majorana bound states (MS) from smooth local perturbations. However, the degree of protection depends on the size of the topological gap, as the information stored in the MS can be compromised if the perturbation energy approaches or exceeds Δ_{top}. Thus, large values of Δ_{top} are desirable for designing robust MSs suitable for constructing fault-tolerant qubits.

The magnitude of Δ_{top} has been shown to strongly depend on the junction's crystallographic orientation (θ_c), the spin-orbit angle (θ_{so}) and the in-plane magnetic field orientation (φ_B), being optimal when the following relation is fulfilled [67, 68],

$$\tan\varphi_B = \cot\theta_{so}\sec 2\theta_c - \tan 2\theta_c. \tag{9}$$

Therefore, it is crucial to investigate how the topological gap protecting the end-like and edge-like MSs depends on the superconducting phase difference and magnetic field strength in junctions subjected to the constraint imposed by Eq. (9).

C. End-like vs. edge-like Majorana states

As briefly discussed in the Introduction, end-like MSs are localized at the opposite ends of the junction channel, with short localization lengths both along the junction and along the system's edges perpendicular to it. In contrast, edge-like MSs are localized solely along the junction direction but extend across the full length of the system's edges perpendicular to the junction. We want to emphasize that the edge-like MSs examined here differ from both chiral Majorana states commonly associated with quantum anomalous Hall systems coupled to superconductors [78–80] and unidirectional Majorana edge states in noncentrosymmetric superconductors [95].

To understand the origin of the extended nature of edge-like MSs, consider a simplified model of a junction sufficiently long such that the overlap between Majorana states at opposite edges is negligible. In this scenario, we can focus solely on one Majorana state, for instance, the one localized at the bottom edge ($y = 0$). Assuming the S regions are infinitely wide ($W_S \to \infty$), the scattering states in the left S region can be expressed as [67, 73],

$$\Psi(\mathbf{r}) = e^{-\kappa y}\sum_{s=\pm}[C_{e,s}\chi_{e,s}e^{-iq_{e,s}x} + C_{hs}\chi_{h,s}e^{iq_{h,s}x}], \tag{10}$$

where κ describes the localization of the Majorana state along the junction y-direction, the subindexes e and h refer to electron-like and hole-like states, respectively, $s = \pm$ characterizes the spin, and $q_{e,s}$ ($q_{h,s}$) is the wave vector of the electron-like (hole-like) state with spinor $\chi_{e,s}$ ($\chi_{h,s}$) and spin s.
At $\phi = 0$, the coefficients $C_{e,s}$ and $C_{h,s}$ become phase-independent, and the asymptotic behavior of $\Psi(x, y)$ along the edge is entirely determined by the wave vectors. By combining Eqs. (1) and (10) and requiring the energy to vanish, we obtain the following quartic equation for q^2,

$$\left(|\mathbf{E}_Z|^2 + \mathbf{w}\cdot\mathbf{w} + |\Delta_0|^2 + \xi^2\right)^2 - 4\left[|\mathbf{E}_Z|^2(|\Delta_0|^2 + \xi^2) + (\mathbf{w}\cdot\mathbf{w})\xi^2 + (\mathbf{E}_z\cdot\mathbf{w})^2\right] = 0, \tag{11}$$

where,

$$\mathbf{w} = \begin{pmatrix} q\beta\cos 2\theta_c + i\kappa(\alpha - \beta\sin 2\theta_c) \\ -q(\alpha + \beta\sin 2\theta_c) - i\kappa\beta\cos 2\theta_c \\ 0 \end{pmatrix}, \tag{12}$$

is the spin-orbit field and $\xi = \hbar^2 q^2/(2m^*) - \mu_S + \epsilon$.
The solutions to the quartic equation [Eq. (11)] represent the wave vectors $q_{j,s}$ ($j = e, h$). At $\phi = 0$, the Majorana state's character is determined by the nature of these wave vectors. Specifically, each scattering mode $\{j, s\}$

contributing to the Majorana state in the S region decays within a characteristic length,

$$l_{j,s} \sim \frac{1}{\mathrm{Im}[q_{j,s}]} \,. \tag{13}$$

The overall localization length of the Majorana state along the edge is given by the largest of the $l_{j,s}$. Hence, at $\phi = 0$, end-like Majorana states appear when all wave vectors are complex. Conversely, if at least one wave vector is purely real, the corresponding scattering mode represents a propagating wave, leading to an edge-like MS.

The coefficients of the quartic equation [Eq. (11)] are generally complex, yielding complex solutions for all wave vectors and resulting in end-like MSs. However, if the conditions,

$$\alpha^2 \sin 2\varphi_B + \beta^2 \sin(2\varphi_B + 4\theta_c) = \alpha\beta \cos 2\theta_c = 0, \tag{14}$$

are satisfied, all coefficients of the quartic equation become real. This allows for purely real wave vectors, enabling the emergence of edge-like MSs if the system parameters are appropriately tuned. All the configurations considered in the numerical analysis presented in Sec. III are chosen in such a way that Eq. (14) and the condition for optimal topological gap [Eq. (9) are simultaneously fulfilled.

In general, we can anticipate three scenarios: i) four real wave vectors, leading to edge-like MSs composed of the superposition of four propagating modes; ii) two real and two complex wave vectors, resulting in edge-like MSs formed by two propagating and two localized modes; and iii) four complex wave vectors, corresponding to localized end-like MSs. By appropriately tuning the system parameters, the system can be driven into any of these scenarios, enabling controlled transitions between end-like and edge-like behaviors. Furthermore, at finite superconducting phase differences, the coefficients $C_{e,s}$ and $C_{h,s}$ in Eq. (10) become ϕ-dependent. This dependence governs the interference between the four scattering modes, thereby modulating the localization characteristics of the Majorana states (MSs).

To capture the topological character of the state, the magnitude of the topological gap, and the extension of the MSs along the edges perpendicular to the junction, we introduce the quantity,

$$\tilde{\Delta} = \frac{(1-Q)\Delta_{top}}{2\Delta_0} \,\mathrm{sgn}(\xi) \tag{15}$$

where ξ s a parameter that characterizes the nature of the MSs, taking positive values for edge-like MSs and negative values for end-like MSs.

In what follows, we refer to $\tilde{\Delta}$ as the *topological gap character*. Its magnitude represents the topological gap normalized to the proximity-induced superconducting gap, while its sign indicates the nature of the Majorana states: positive for edge-like MSs, negative for end-like MSs, and zero when the system is in the trivial state (or in the BDI-class TS with an even number of Majorana pairs), i.e.,

$$\tilde{\Delta} = \begin{cases} +\Delta_{top}/\Delta_0 & \text{for D-class TS with edge-like MSs} \\ 0 & \text{for trivial phase with no MSs} \\ 0 & \text{for even BDI-class TS phase} \\ -\Delta_{top}/\Delta_0 & \text{for D-Class with end-like MSs} \end{cases} . \tag{16}$$

Although we limit our analysis to MSs within the D class, the topological character defined in Eq. (15) can easily be generalized to account for the BDI-class TS by using the winding number (the $\mathbb{Z}$ topological invariant) instead of the topological charge.

For the junctions studied here, the probability density of edge-like MSs displays an oscillatory behavior along the edge, with multiple local maxima of comparable amplitudes. In contrast, the probability density oscillations of end-like MSs decay rapidly, featuring a large maximum at the middle of the junction edge, followed by a few significantly smaller maxima. Therefore, the localization nature of the MSs can be captured by the parametrization $\xi = n - n_0 - 1/2$, where n is the number of probability density local maxima with comparable amplitudes. Since the typical number of local maxima for end-like MSs is smaller than 3, we set $n_0 = 3$ in the numerical simulations of Eq.(16) discussed below. For higher chemical potentials and/or larger W_N and W_S one may need to increase n_0 accordingly.

D. Phase-biased and phase-unbiased JJs

The eigenenergies E_n can be used to compute the phase-dependent part of the junction's free energy,

$$F = -\sum_{E_n>0} [E_n + 2k_B T \ln(1 + e^{-E_n/k_B T})]. \tag{17}$$

In the phase-biased case, the JJ is incorporated in a closed loop threaded by a magnetic flux Φ, which fixes the superconducting phase across the junction to $\phi = 2\pi\Phi/\Phi_0$, where Φ_0 is the magnetic flux quantum.

In the absence of the magnetic flux, the junction is phase unbiased, and the phase difference is self-adjusted in such a way that the free energy of the system is minimized. The ground-state phase (ϕ_{GS}) is the superconducting phase difference that minimizes the free energy of the system, i.e.,

$$F(\phi_{GS}) = \min_{\phi} F(\phi). \tag{18}$$

Since the free energy also depends on the Zeeman energy, ϕ_{GS} is generally a function of the magnetic field. This offers a mechanism for indirectly controlling the superconducting phase difference using an in-plane magnetic field, without relying on a magnetic flux.

III. RESULTS

We consider two types of junctions: (i) Al/HgTe Josephson junctions (JJs), where Rashba spin-orbit coupling (SOC) is the dominant effect, and (ii) Al/InSb JJs, where both Rashba and Dresselhaus SOC may be significant. The system parameters used in our calculations are provided in Appendix A. The numerical simulations were carried out by discretizing Eq. (1) on a mesh with a lattice constant of $a = 10$ nm. Using the finite-difference approximation, we constructed the tight-binding (TB) form of the BdG Hamiltonian with the Kwant package [96]. The energy spectrum and wave functions were obtained by numerically diagonalizing the TB BdG Hamiltonian on a finite lattice. The energy spectrum was then used to compute the topological gap [Eq. (8)], the phase-dependent part of the free energy [Eq. (16)], and the ground-state phase [Eq. (16)]. The topological charge [see Eq. (7)] was computed by using the system TB BdG Hamiltonian with imposed translational invariance along the junction direction.

A. Effects of Rashba SOC

In Al/HgTe Josephson junctions (JJs), where Rashba SOC is the dominant and Dresselhaus SOC is negligibly small (i.e., $\beta \approx 0$), the spin-orbit angle $\theta_{so} \approx 0$ and $\lambda \approx \alpha$ [see Eqs. (3) and (4)]. In this scenario, the system exhibits magneto anisotropyy (i.e., its properties depend on the in-plane magnetic field orientation, φ_B), while crystalline anisotropy is absent (i.e., the system properties are independent of the junction's crystallographic direction, θ_c) [66–68]. For the calculations presented in this subsection, the in-plane magnetic field was aligned with the junction direction (i.e., $\varphi_B = \pi/2$), which, as discussed in Ref. [67], yields the optimal topological gap for this configuration.

Figure 2(a) shows the behavior of the topological gap character ($\tilde{\Delta}$), as a function of the Zeeman field (E_Z) and the superconducting phase difference (ϕ) in a phase-biased JJ. Gray areas correspond to $\tilde{\Delta} = 0$, indicating topologically trivial (with respect to the D classification) regions with topological charge $Q = 1$. Note, however, that the gray zone may still contain regions of BDI-class TS with an even number of MS pairs. As previously mentioned here we disregard those regions, as they exhibit a relatively small topological gap. Blue (red) areas indicate regions where $\tilde{\Delta} < 0$ ($\tilde{\Delta} > 0$) correspond to a D-class TS phase that supports the formation of end-like (edge-like) MSs. The figure reveals that in junctions where only Rashba SOC is significant, the formation of end-like MSs with a sizable topological gap is favored for ϕ-values near π. In contrast, less robust edge-like MSs with smaller topological gaps emerge when the system is in the TS state, and ϕ is near 0 or 2π.

The effect of the superconducting phase difference on

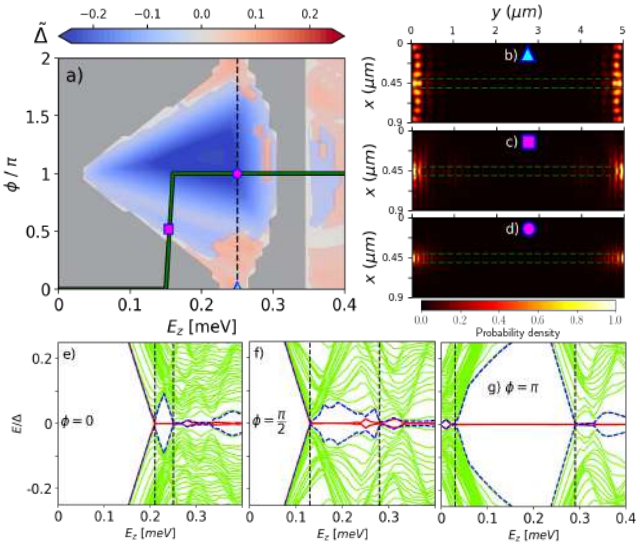

FIG. 2. (a) Topological gap character ($\tilde{\Delta}$) as a function of the Zeeman energy E_Z and the superconducting phase difference (ϕ) across an Al/HgTe JJ with only Rashba SOC ($\theta_{so} = 0$). The junction and magnetic field orientations are set to $\theta_c = 0$ and $\varphi_B = \pi/2$, respectively. The green solid line represents the path of the ground-state phase (ϕ_{GS}) as the Zeeman energy is varied. The vertical dashed line marks a possible transition between a TS state supporting a zero-phase edge-like MS (cyan triangle) and one supporting an end-like MS (magenta dot) during which E_Z is kept constant, while ϕ is tuned. (b)-(d) Probability density (normalized to its maximum value) of the MSs corresponding to the E_Z and ϕ values marked in (a) by the cyan triangle (edge-like MS), magenta square (end-like MS), and magenta dot (end-like MS), respectively. (e)-(g) Energy spectra as a function of the Zeeman energy for $\phi = 0$, $\phi = \pi/2$, and $\phi = \pi$, respectively. Red-solid and dashed-blue lines represent states that evolve into MSs as E_Z is varied. Vertical dashed lines indicate the boundaries of the first topological region in which only a single pair of MSs (red solid lines) exists.

the localization nature of the MSs can be qualitatively understood by noting that the phase factor of the superconducting pairing potential appearing in the antidiagonal blocks of the BdG Hamiltonian can be gauged away by a position-dependent unitary transformation (see details in Appendix B). As a result, the BdG Hamiltonian of a junction with a superconducting phase difference ϕ is transformed into a BdG Hamiltonian of a junction with zero phase difference, but in the presence of a position-dependent gauge potential with strength proportional to ϕ. The edge-like MSs at zero phase transit to end-like MSs when the ϕ-dependent gauge field is strong enough.

Considering a junction with infinitely wide S regions (i.e., $W_S \to \infty$) and a Zeeman field along the junction direction and much larger than the Rashba SOC splitting, we can write the approximate solutions of Eq. (11)

as,

$$q_{j,s} = \sqrt{\left[\frac{\sqrt{2m^*\left(\mu_S + j\sqrt{E_Z^2 - \Delta_0^2}\right)}}{\hbar} + s\, k_{so}\right]^2 + \kappa^2} \tag{19}$$

where $j = e = 1$ ($j = h = -1$) for electron-like (hole-like) states, $E_Z = |\mathbf{E}_Z|$, and $k_{so} = m^*\alpha/\hbar^2$. This indicates that zero-phase edge-like MSs of junctions with only Rashba SOC and magnetic field along the junction direction appear when the system is in the TS state and the following conditions are fulfilled,

$$E_Z \geq \Delta_0 \text{ and } \mu_S \geq \sqrt{E_Z^2 - \Delta_0^2}. \tag{20}$$

Indeed, in such a situation, all the wave vectors are purely real (i.e. $\mathrm{Im}[q_{j,s}] = 0$) and the the MS localization length, $l_{j,s} \to \infty$.

When the second inequality in Eq.(20) is satisfied (as it is for the parameters used in the numerical simulations), the emergence of edge-like MSs at $\phi = 0$ in the limit $W_S \to \infty$ is governed by the condition $E_Z \geq \Delta_0$. However, since the numerical simulations account for superconducting regions of finite width, the results shown in Fig. 2(a) —where zero-phase edge-like MSs appear at Zeeman energies slightly below Δ_0 —exhibit a small deviation from the condition $E_Z \geq \Delta_0$. The impact of finite-size effects on the topological phase diagram of planar JJs has been explored in Ref.[66].

In phase-unbiased junctions, the system's state evolves according to the trajectory of the ground-state phase [see green solid line in Fig. 2(a)] as the Zeeman field is varied. During the $0-\pi$ ground-state jump at $E_Z \approx 0.14$ meV, the junction undergoes a transition from the trivial to a TS phase with end-like MSs. A self-tuning mechanism, where edge-like MSs transition into end-like MSs (and/or vice versa) as the Zeeman field varies, appears impractical in phase-unbiased junctions with only Rashba SOC. However, a topologically protected transition in which end- and edge-like MSs can be transformed into each other without exiting the TS state seems feasible by tuning the magnetic flux in phase-biased Josephson junctions (JJs). Since the system remains in the same TS state the topological gap does not close during the process, providing topological protection to the transition. This is illustrated in Fig. 2(a), where an edge-like MS (cyan triangle) can evolve into an end-like MS (magenta dot) by adjusting the Zeeman field (at the value indicated by the vertical dashed line) and varying the phase from 0 to π.

To visualize the spatial extension of the edge-like MSs along the sample edges perpendicular to the junction, Fig. 2(b) shows the probability density (normalized to its maximum value) of the edge-like MS corresponding to the cyan triangle in Fig. 2(a) at $\phi = 0$. The probability density exhibits an oscillatory behavior with multiple maxima of comparable amplitude. Note that the edge-like MSs consistently spread along the entire edge extension, regardless of the width W_S of the S regions (see Appendix C). In contrast, the probability density of the end-like MSs corresponding to the magenta square and magenta dot in Fig. 2(a) [see Figs. 2(c) and (d), respectively] is localized at the opposite ends of the junction with wave functions that decay both along and perpendicular to the junction's direction.

The energy spectrum as a function of E_Z is shown in Figs. 2(e)-(g) for $\phi = 0, \pi/2, \pi$, respectively. The red solid and blue dotted lines represent the states with energies closest to zero, which evolve into MS as the junction transitions into the TS phase. The vertical lines mark the Zeeman energy boundaries of the first topological region, characterized by the $\mathbb{Z}_2$ invariant of the D class, where the topological charge is $Q = -1$ [see Eq. (7)]. Within this region, the absolute value of the $\mathbb{Z}$ invariant of the BDI class equals 1, indicating the presence of a single pair of MSs, as shown by the red lines in Figs. 2(e)-(g). Additionally, regions where a second pair of MSs emerge (blue dashed lines) can also be observed. In these regions, the system remains in the BDI class and supports two pairs of MSs, corresponding to an absolute value of 2 for the $\mathbb{Z}$ invariant of the BDI class. However, it is important to note that the topological gap in regions with multiple pairs of MSs is significantly smaller than in regions where only a single pair of MSs exists [this is particularly clear in Fig. 2(g)]. For this reason, our analysis of edge-like and end-like MSs is focused on topological regions containing only a single pair of MSs.

B. Effects of Dresselhaus SOC

We now focus on JJs where only the Dresselhaus SOC plays a significant role. In this scenario, with $\alpha = 0$ and $\lambda = \beta \neq 0$, we can assume $\theta_{so} = \pi/2$ without loss of generality. Unlike linear Rashba SOC, the Dresselhaus spin-orbit field is not rotationally invariant about the axis normal to the junction plane, leading to the emergence of both magneto-anisotropy and crystalline anisotropy in the system. Therefore, to optimize the topological gap, it is essential to carefully align both the in-plane magnetic field angle φ_B and the crystallographic orientation of the junction θ_c. For numerical simulations, we use the values $\theta_c = \varphi_B = 0$, which together with $\theta_{so} = \pi/2$, satisfy the condition in Eq. (9).

The character of the topological gap $\tilde{\Delta}$, depicted in Fig. 3(a) as a function of E_Z and ϕ, exhibits an overall behavior similar to that shown in Fig. 2(a). Specifically, edge and end-like MSs emerge at phase values near 0 and π, respectively. Notably, edge-like MSs are better protected by a larger topological gap in JJs dominated by Dresselhaus SOC compared to those where Rashba SOC is predominant.

The ground-state phase trajectory [green line in Fig. 2(a)] in phase-unbiased JJs undergoes a $0-\pi$ transition, enabling the system to enter the TS state at a lower Zeeman energy compared to when the phase is fixed at

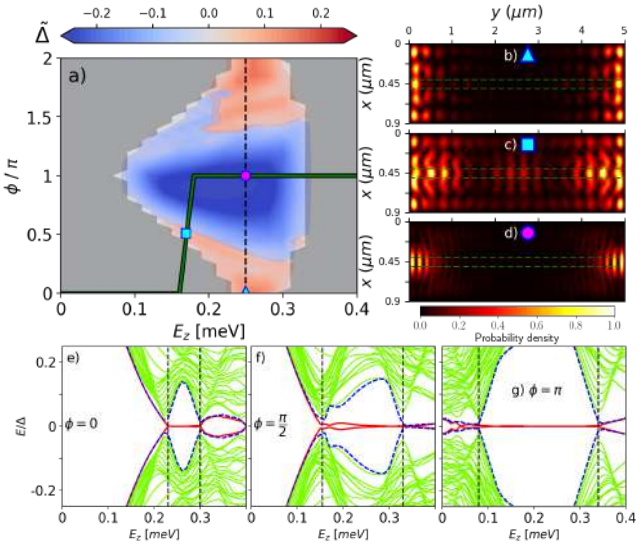

FIG. 3. (a) Topological gap character ($\tilde{\Delta}$) as a function of the Zeeman energy E_Z and the superconducting phase difference (ϕ) across an Al/InSb JJ, where the Rashba SOC has been tuned to a negligibly small value and only Dresselhaus SOC is relevant ($\theta_{so} = \pi/2$). The junction and magnetic field orientations are set to $\theta_c = 0 = \varphi_B = 0$. The green solid line represents the path of the ground-state phase (ϕ_{GS}) as the Zeeman energy is varied. The vertical dashed line marks a possible transition between a TS state supporting a zero-phase edge-like MS (cyan triangle) and one supporting an end-like Majorana state (magenta dot) during which E_Z is kept constant, while ϕ is tuned. (b)-(d) Probability density (normalized to its maximum value) of the MSs corresponding to the E_Z and ϕ values marked in (a) by the cyan triangle (edge-like MS), cyan square (edge-like MS), and magenta dot (end-like MS), respectively. (e)-(g) Energy spectra as a function of the Zeeman energy for $\phi = 0$, $\phi = \pi/2$, and $\phi = \pi$, respectively. Red-solid and dashed-blue lines represent states that evolve into MSs as E_Z is varied. Vertical dashed lines indicate the boundaries of the first topological region in which only a single pair of MSs (red solid lines) exists. The deviation of the edge-like MS energies (red solid lines) from zero in (f) results from the wavefunction overlap between edge-like MSs on opposite edges [see (c)].

zero. However, as in the case of Rashba SOC, a self-tuned transition from end-like to edge-like MSs appears unfeasible in JJs with only Dresselhaus SOC. Nonetheless, the end-to-edge transition can still be achieved with external control of the superconducting phase difference. For example, as indicated by the vertical dotted line in Fig. 3(a), fixing the in-plane magnetic field to a value corresponding to $E_Z \approx 0.25$ meV and tuning ϕ from 0 to π would induce a transition from edge to end-like MSs.

The probability density of MSs corresponding to the values of E_Z and ϕ marked by the cyan triangle, cyan square, and magenta dot in Fig. 3(a) are shown in Figs. 3(b)-(d), respectively. Additionally, the dependence of the energy spectra on E_Z for $\phi = 0, \pi/2, \pi$ is depicted in Figs. 3(e)-(g), respectively. Compared to the edge-like MS illustrated in Fig. 2(b), the zero-phase edge-like MSs in Fig. 3(b) are protected by a larger topological gap [see Figs. 2(e) and 3(e)]. However, MSs in junctions with only Rashba SOC exhibit stronger localization along the junction, implying that JJs with dominant Dresselhaus SOC would need to be longer to effectively prevent the overlap between MSs localized at opposite ends (or edges). The overlap between MSs from opposite edges, particularly evident in Fig. 3(c), causes their energies to deviate from zero [seen in Fig. 3(f)].

C. Effects of combined Rashba and Dresselhaus SOCs

In systems like Al/InSb-based junctions, the coexistence of significant Rashba and Dresselhaus SOC generates a two-fold symmetric spin-orbit field. This, combined with the Zeeman interaction, results in nontrivial magneto anisotropic and crystalline anisotropic effects. The relative strength of Rashba (α) and Dresselhaus (β) SOCs can be tuned by adjusting the Rashba SOC via a gate placed on top of the junction [48]. A particularly interesting regime arises when the Rashba and Dresselhaus SOCs are equally strong. Based on the parametrization introduced in Eqs. (3) and (4), the condition $\alpha = \beta$ corresponds to the SOC angle $\theta_{so} = \pi/4$.

The character of the topological gap ($\tilde{\Delta}$) is shown in Fig. 4(a) as a function of E_Z and ϕ, with $\theta_{so} = \pi/4$. The crystallographic and magnetic field orientations were chosen as $\theta_c = 3\pi/4$ and $\varphi_B = \pi/2$, respectively, ensuring that the condition in Eq. (9) is satisfied. A distinctive feature of this regime is that, unlike the previously discussed cases, edge-like MSs can emerge at superconducting phase differences close to π. Additionally, the coexistence of Rashba and Dresselhaus SOCs leads to an overall enhancement of the topological gap.

As in the cases discussed in the previous subsections, in phase-biased JJs with both Rashba and Dresselhaus SOC transitions between edge and end-like MSs can also be induced by tuning the magnetic field while keeping the phase fixed at an appropriate value [e.g., following the dotted line from the cyan dot to the magenta square in Fig. 4(a)] or by fixing the magnetic field and tuning the phase difference [e.g, following the dotted line from the cyan triangle to the magenta square in Fig. 4(a)]. Remarkably, the coexistence of Rashba and Dresselhaus SOC allows for transitions between edge and end-like MSs in phase-unbiased junctions, something not observed in systems with only Rashba or only Dresselhaus SOC. As shown in Fig. 4(a), the self-tuning of the ground-state phase (green solid line) as the Zeeman energy varies creates a transition pathway between (red) regions hosting edge-like MSs and (blue) regions hosting end-like MSs. For instance, along the ground-state trajectory, the edge-like MSs at the cyan dot can transition into the end-like MSs at the magenta cross.

For completeness, the probability densities of the MSs

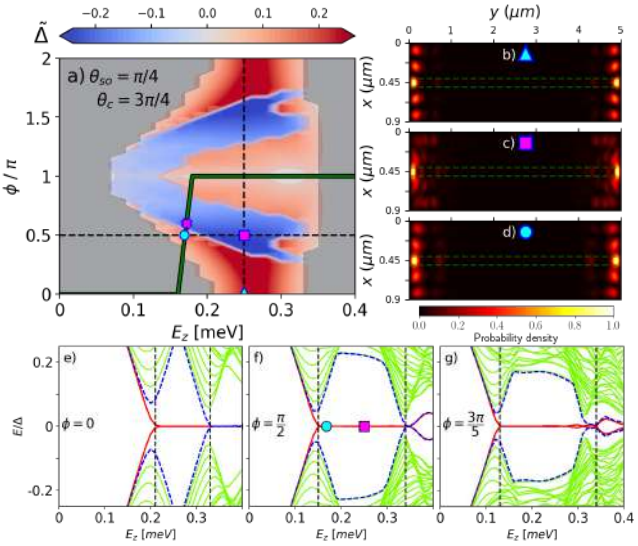

FIG. 4. (a) Topological gap character ($\tilde{\Delta}$) as a function of the Zeeman energy E_Z and the superconducting phase difference (ϕ) across an Al/InSb JJ, with equal Rashba and Dresselhaus SOC strengths ($\theta_{so} = \pi/4$). The junction and magnetic field orientations are set to $\theta_c = 3\pi/4$ and $\varphi_B = \pi/2$, respectively. The green solid line represents the path of the ground-state phase (ϕ_{GS}) as the Zeeman energy is varied. The vertical (horizontal) dashed line marks a possible transition between a TS state supporting a zero-phase edge-like MS (cyan triangle/dot) and one supporting an end Majorana state (magenta square) during which E_Z (ϕ) is kept constant while ϕ (E_Z) is tuned. A transition between edge-like (e.g., cyan dot) and end-like (e.g., magenta cross) MSs can also be achieved by solely tuning E_Z, as the value of ϕ self-adjusts and follows the path of the ground-state phase (green solid line). (b)-(d) Probability density (normalized to its maximum value) of the MSs corresponding to the E_Z and ϕ values marked in (a) by the cyan triangle (edge-like MS), magenta square (end-like MS), and cyan dot (edge-like MS), respectively. (e)-(g) Energy spectra as a function of the Zeeman energy for $\phi = 0$, $\phi = \pi/2$, and $\phi = 3\pi/5$, respectively. Red-solid and dashed-blue lines represent states that evolve into MSs as E_Z is varied. Vertical dashed lines indicate the boundaries of the first topological region in which only a single pair of MSs (red solid lines) exists.

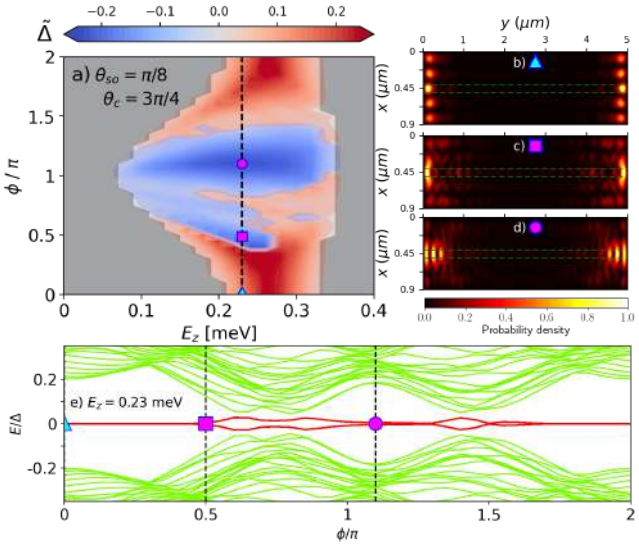

FIG. 5. (a) Topological gap character ($\tilde{\Delta}$) as a function of the Zeeman energy E_Z and the superconducting phase difference (ϕ) across an Al/InSb JJ, with Rashba SOC strength about 2.4 times greater than the Dresselhaus SOC strength ($\theta_{so} = \pi/8$). The junction and magnetic field orientations are set to $\theta_c = 3\pi/4$ and $\varphi_B = \pi/2$, respectively. (b)-(d) Probability density (normalized to its maximum value) of the MSs corresponding to the E_Z and ϕ values marked in (a) by the cyan triangle (edge-like MS), magenta square (end-like MS), and magenta dot (end-like MS), respectively. (e) Energy spectrum along the path indicated by the vertical dashed line in (a), where $E_Z = 0.23$ meV and ϕ is varied from 0 to 2π. The symbols in (e) indicated the energy of the MSs whose probability densities are plotted in (b)-(d).

corresponding to the E_Z and ϕ values indicated by the cyan triangle, magenta square, and cyan dot in Fig. 4 are shown in Figs. 4(b)-(d), respectively. Both the edge-like MSs [Figs. 4(b) and (d)] and the end-like MSs [Fig. 4(c)] exhibit strong localization along the junction direction, resulting in very stable MSs within the first topological region, which contains a single pair of MSs. This stability is evident in the energy spectra presented in Figs. 4(e)-(g) for $\phi = 0, \pi/2, 3\pi/5$, where very flat zero-energy MSs (red lines) with an enhanced topological gap, compared to the cases with only Rashba SOC [see Figs. 2(e)-(g)] or only Dresselhaus SOC [see Figs. 3(e)-(g)], are clearly visible. Notably, the transition between edge-like (cyan dot) and end-like (magenta square) MSs induced by varying E_Z while keeping $\phi = \pi/2$ is very robust, with MSs maintaining their zero energy and protected by a sizable topological gap, as can be appreciated in Figs. 4(f).

In junctions where the strengths of Rashba and Dresselhaus SOC are equal (e.g., $\theta_{so} = \pi/4$), the topological gap exhibits mirror symmetry with respect to $\phi = \pi$, as shown in Fig. 4(a). However, this symmetry is broken when the Rashba and Dresselhaus SOC strengths are no longer equal, as illustrated in Fig. 5(a), where the topological gap character is plotted as a function of E_Z and ϕ for the case of a JJ with $\theta_{so} = \pi/8$ (i.e., $\alpha/\beta \approx 2.4$), $\theta_c = 3\pi/4$, and $\varphi = \pi/2$. The vertical dashed line highlights a path along which the JJ transitions between end and edge-like MSs as ϕ is varied while keeping E_Z constant. The probability densities of an edge-like MS (cyan triangle) and two end-like MSs (magenta square and magenta dot) are shown in Figs. 5(b)-(d), where their localization properties are illustrated.

The evolution of the energy spectrum along the path marked with the dashed line in Fig. 5(a) is displayed in Fig. 5(e). Red lines represent the energies of the MSs. As the superconducting phase difference is varied, the junction undergoes multiple transitions between end and edge-like MSs. Since all the transitions occur within the

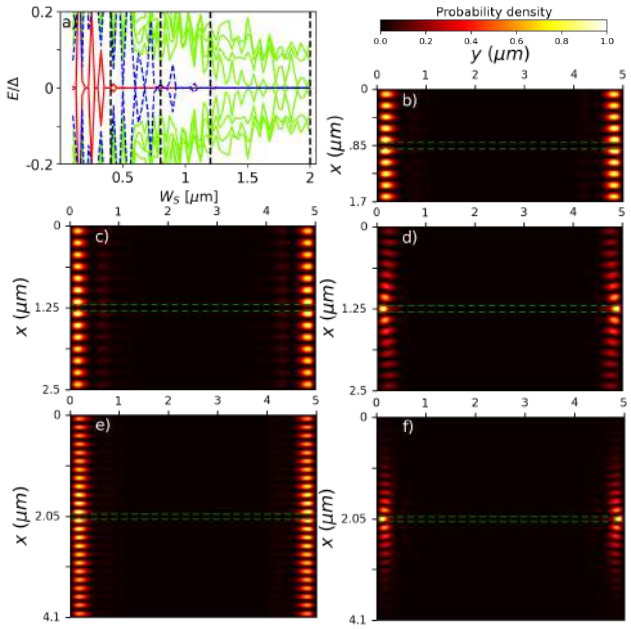

FIG. 6. (a) Energy spectrum as a function of W_S for $\phi = 0$ and $E_Z = 0.25$ meV. The other system parameters were taken as in Fig. 4. Red-solid and dashed-blue lines represent states that evolve into MSs as W_S is varied. Vertical dashed lines indicate W_S-values of 0.4 μm, 0.8 μm, 1.2 μm, and 2 μm. (b)-(f) Probability density (normalized to its maximum value) for JJs with (b) $W_S = 0.8$ μm, (c) and (d) $W_S = 1.2$ μm, and (e) and (f) $W_S = 2$ μm. The edge-like Majorana pair in (b) evolves into the one shown in (c) (when W_S increases from $W_S = 0.8$ μm to $W_S = 1.2$ μm) and then into the edge-like pair shown in (e) when $W_S = 2$ μm. A second Majorana pair [shown in (d)] exists when $W_S = 1.2$ μm and eventually evolves into the end-like MS displayed in (f).

TS state, they occur in a protected way, i.e., without gap closings. This is also true for the transitions indicated in Figs. 2(a), 3(a), and 4(a). It is important to note, however, that for practical applications, the transition path may need to be further optimized with respect to variations in E_Z, ϕ, and system size in order to identify the path between end-like and edge-like MSs that maximizes the topological gap.

To illustrate the behavior of the MSs as the size of the S regions increases, we show in Fig. 6 the energy spectrum as a function of W_S for $\phi = 0$ and $E_Z = 0.25$ meV, with all other system parameters as in Fig. 4. For clarity, only the 12 states with energies closest to zero are shown. Red-solid and blue-dashed lines indicate states that evolve into MSs as W_S increases. In regions where multiple Majorana pairs coexist, some energy lines may be indistinguishable, as they overlap. Vertical dashed-lines mark the values $W_S = 0.4,\ 0.8,\ 1.2,\ 2$ μm.

The probability density (normalized to its maximum value) of the edge-like MSs in a JJ with $W_S = 0.4$ μm [see Fig. 4(b)] transforms into the edge-like MSs shown in Figs. 6(b), (c), and (e) as W_S increases to 0.8 μm, 1.2 μm, and 2 μm, respectively. A second Majorana pair appears at $W_S = 1.2$ μm [see Fig. 6(d)] and eventually transitions into the end-like Majorana pair displayed in Fig. 6(f) as the extent of the S regions increase to 2 μm. Although not depicted in Fig. 6, a third pair of MSs exists at $W_S = 2$ μm.

It is important to note that as long as the chemical potential μ is larger than the other characteristic energy scales of the system (Δ_0, E_Z, and the spin-orbit coupling energy splitting), its specific value has no direct impact on the emergence of edge-like Majorana states (MSs), as suggested by Eq. (19). Thus, our calculations for $\mu = 1$ meV (a value larger than the other relevant energy scales) are expected to remain qualitatively accurate even for higher chemical potentials. However, the chemical potential still plays a crucial role, as it affects the extent of the topological region in the $\phi - E_Z$ parameter space. For MSs to emerge, the system must first be driven into the topological superconducting (TS) state. Once in the TS state, the primary effect of the chemical potential is to modulate the oscillations of the edge-like MSs.

As indicated by Eq. (19), when the wave vectors are real, they increase with the chemical potential, leading to shorter wavelengths for the propagating modes and faster oscillations in the probability density of the edge-like MSs. This behavior is evident in Figs. 7(a)–(d), which display the probability density for junctions with chemical potentials of 4 meV, 6 meV, 12 meV, and 15 meV, respectively.

Due to their distinct localization characteristics, end-like and edge-like MSs can yield different experimental outcomes. Understanding the behavior and properties of these states is, therefore, crucial for correctly interpreting their experimental detection. For instance, the sharp contrast in the zero-bias conductance peak (ZBCP) observed in Josephson junctions (JJs) when the superconducting phase is changed from $\phi = 0$ to $\phi = \pi$ [49] could be related to a transition between edge-like and end-like MSs. At $\phi = 0$, edge-like MSs exhibit reduced probability density beneath the contact, leading to a smaller ZBCP amplitude. Conversely, at $\phi = \pi$, end-like MSs have a larger probability density below the contact, resulting in a more prominent ZBCP amplitude. Moreover, because edge-like MSs extend along the entire junction edges, they could act as global interconnects, enabling coupling between distant MSs. This coupling can be controlled by switching between edge-like and end-like MSs, offering a potential mechanism for modulating interactions in topological quantum devices.

IV. SUMMARY

We investigated the formation and properties of edge-like and end-like MSs in proximitized planar JJs subjected to an in-plane magnetic field, considering the effects of Rashba and/or Dresselhaus SOCs. The end-like MSs are primarily localized at opposite ends of the nor-

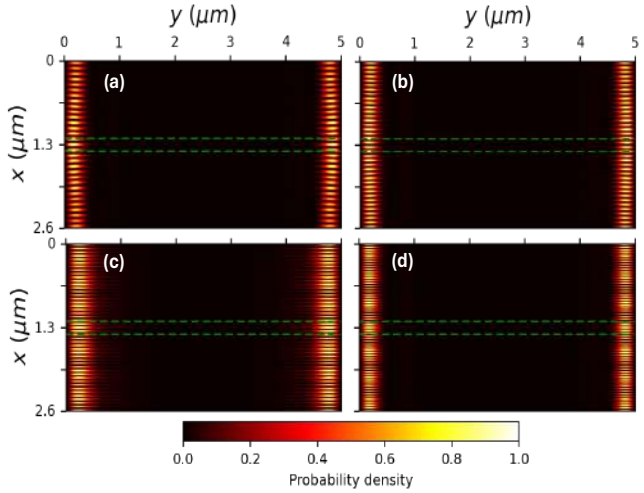

FIG. 7. Probability density (normalized to its maximum value) for JJs with $W_S = 1.2$ μm, $W_N = 0.2$ μm, $E_z = 0.25$ meV, and chemical potential (a) $\mu_{S(N)} = 4$ meV, (b) $\mu_{S(N)} = 6$ meV, (c) $\mu_{S(N)} = 12$ meV, and (d) $\mu_{S(N)} = 15$ meV. The other parameters were taken as in Fig. 4(a), namely, $\theta_{so} = \pi/4$, $\theta_c = 3\pi/4$, $\phi = 0$, and $\varphi_B = \pi/2$.

mal region within the junction. In contrast, the edge-like MSs extend along the system's edges, perpendicular to the junction. To characterize the nature and protection of the MSs we introduced a quantity called the *topological gap character*. This quantity provides insight into whether the system is in the D-class (or BDI-class with $\mathbb{Z}_2$ index equal to ± 1) TS state, the size of the topological gap, and whether the MSs are end-like or edge-like. Through numerical simulations of the topological gap character as a function of the magnetic field strength and the superconducting phase difference (ϕ) across the junction, we found that when the system is in the TS state, and either Rashba or Dresselhaus SOC dominates, edge-like and end-like MSs, protected by a sizable topological gap, typically emerge near ϕ values of 0 and π, respectively. However, when the Rashba and Dresselhaus SOC strengths are comparable, and the junction and magnetic field are properly oriented, protected edge-like MSs can also emerge at phases near π. Our results reveal the possibility of inducing topologically protected transitions between edge-like and end-like MSs in phase-biased JJs by tuning the superconducting phase difference and the magnetic field strength. Furthermore, in phase-unbiased junctions with comparable Rashba and Dresselhaus SOC strengths, protected transitions between end and edge-like MSs can be achieved by solely adjusting the magnetic field strength, as the superconducting phase self-tunes to minimize the system's free energy. Controlled transitions between edge-like and end-like MSs could function as switchable global interconnects, enabling or disabling the coupling between distant MSs.

ACKNOWLEDGMENTS

A.P.G. is grateful for the funding of PhD scholarship ANID-Chile No. 21210410. P.A.O. acknowledges support from FONDECYT grants 1230933 and 1220700 and USM-Chile under grant PI-LIR-24-10. A.M.-A. acknowledges support from USM-Chile under grant MEC-USM/2023.

Appendix A

The system parameters used in the numerical simulations are listed in Table I. The values of the hopping parameter $t = \hbar^2/(2m^*a^2)$ are also included.

parameter	Al/HgTe [73]	Al/InSb [84]
Δ_0	0.23 meV	0.21 meV
μ_S	1 meV	1 meV
μ_N	1 meV	1 meV
m^*	$0.038m_o$	$0.013m_o$
λ	16 meV nm	15 meV nm
W_N	100 nm	100 nm
W_S	400 nm	400 nm
L	5000 nm	5000 nm
a	10 nm	10 nm
t	10.0 meV	29.3 meV

TABLE I. Material parameters used in the numerical simulations of proximitized planars JJs reported in this work. The proximity-induced superconducting gap is represented by Δ_0, μ_S (μ_N) denotes the chemical potential in the S (N) region, m^* is the electron effective mass (with m_0 as the bare mass of the electron), $\lambda = \sqrt{\alpha^2 + \beta^2}$ characterizes the combined strength of Rashba (α) and Dresselhaus (β) SOCs, W_N (W_S) is the width of the N (S) region, L is the length of the junction, a is the TB lattice constant, and t the TB hopping parameter.

Appendix B

To get qualitative insight into the role of the superconducting phase difference in the formation of edge-like and end-like MSs, we assume, without loss of generality that $0 \leq \phi \leq \pi$, consider the BdG Hamiltonian in Eq. (1), and apply the unitary transformation,

$$\begin{aligned} U &= (\tau_0 \otimes \sigma_0)\cos[\mathrm{sgn}(x)\phi/2] \\ &+ i(\tau_z \otimes \sigma_0)\sin[\mathrm{sgn}(x)\phi/2] \end{aligned} \tag{B1}$$

which eliminates the phase dependence of superconducting pairing potential at the expense of adding a phase-dependent gauge field to the x component of the momentum. The transformed Hamiltonian,

$$H' = U^\dagger H U, \tag{B2}$$

has the same form as H but with the original pairing potential in Eq. (6) replaced by the zero-phase pairing,

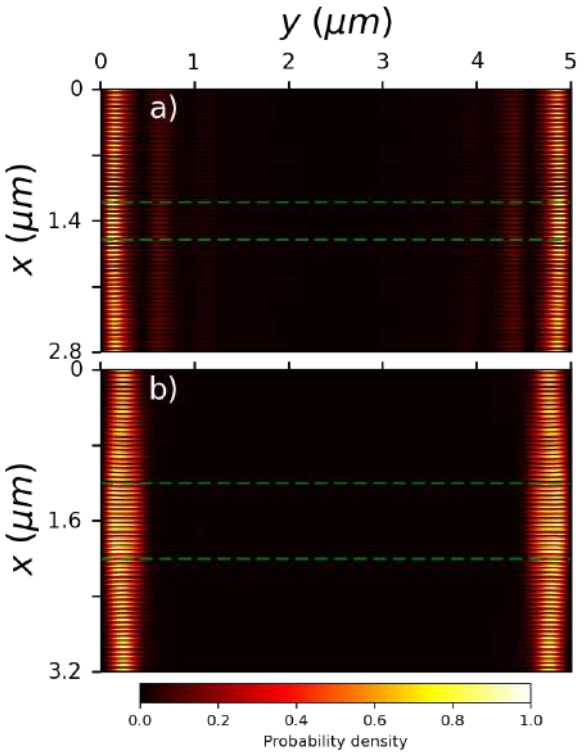

FIG. 8. Probability density (normalized to its maximum value) for JJs with (a) $W_N = 0.4$ μm and (b) $W_N = 0.8$ μm. The other parameters were taken as in Fig. 7(c), namely, $W_S = 1.2$ μm, $E_Z = 0.25$ meV, $\theta_{so} = \pi/4$, $\theta_c = 3\pi/4$, $\phi = 0$, and $\varphi_B = \pi/2$.

$\Delta' = \Delta_0\,\Theta(|x| - W_N/2)$, and the momentum component along the x-axis replaced by, $p'_x = p_x \pm (\phi/2)\delta(x)$ in the particle-like (+) and hole-like (-) blocks of the Hamiltonian, respectively. In other words, a JJ with superconducting phase difference ϕ is equivalent to a JJ with zero phase ($\phi = 0$), but with the Dirac function gauge potentials $A_x = \pm \pm (\phi/2)\delta(x)$ acting on the particle-like and hole-like components of the wavefunction. In the case of a JJ with only Rashba SOC, the gauge potential behaves as an attractive potential in the x-direction. Since it is centered in the middle of the normal (N) region, this potential contributes to the localization of the MSs near the ends of the junction. Conversely, when the gauge potential vanishes for $\phi = 0$, the MSs extend along the edges perpendicular to the junction.

Let's now analyze the case in which the Zeeman field dominates the SOC and the spin is approximately conserved. In such a case one can make the approximation $(\mathbf{w}\cdot\mathbf{E}_z)^2 \approx (\mathbf{w}\cdot\mathbf{w})^2|\mathbf{E}_z|^2$ in Eq. (11) and find approximate analytical solutions for the wave vectors.

1. Magnetic field along the junction ($\mathbf{E}_Z \parallel \hat{\mathbf{y}}$)

Consider a magnetic field aligned along the junction, together with the absence of Dresselhaus SOC ($\beta = 0$) or a junction orientation at an odd multiple of $\pi/4$ with respect to the [100] crystallographic direction of the host semiconductor.
The wave vectors at $\phi = 0$ of zero-energy states are given by,

$$q_{j,\pm} = \sqrt{\left[\frac{\sqrt{2m^*\left(\mu_S + j\sqrt{E_Z^2 - \Delta_0^2}\right)}}{\hbar} \pm k_{so}\right]^2 + \kappa^2} \tag{B3}$$

where $j = e = 1$ ($j = h = -1$) for electron-like (hole-like) states, $E_Z = |\mathbf{E}_Z|$, and

$$k_{so} = \frac{m^*(\alpha + \beta \sin 2\theta_c)}{\hbar^2}. \tag{B4}$$

From Eq. (B3,) one finds that the wave vectors are real if,

$$E_Z \geq \Delta_0 \;\text{ and }\; \mu_S \geq \sqrt{E_Z^2 - \Delta_0^2}. \tag{B5}$$

Hence, edge-like MSs emerge when the system is in the TS state and the conditions in Eq. (B5) are met. Note that, in principle, for the wavefunction to be delocalized, it is sufficient only one, not all, of the wave vectors to be real. In this case, only the first inequality in Eq. (B5) is required. However, when all the wave vectors are real, the wavefunction is guaranteed to be strongly delocalized.

2. Magnetic field perpendicular to the junction ($\mathbf{E}_Z \perp \hat{\mathbf{y}}$)

In this case, the wave vectors of zero-energy states at $\phi = 0$ are found to have the same form as in Eq. (B3) but with,

$$k_{so} = -\frac{m^*\beta \cos 2\theta_c}{\hbar^2}. \tag{B6}$$

We then conclude that in this case, edge-like MSs emerge when the system is in the TS state and the conditions in Eq. (B5) are met.

Appendix C

In Sec. III we focused our discussion on narrow junctions with $W_N = 0.1$ μm [Figs. 3-6] and $W_N = 0.2$ μm. However, the existence of edge-like MSs is also supported in wider junctions as evidenced by Fig. 8, where the probability density (normalized to its maximum value) is shown for (a) $W_N = 0.4$ μm and (b) $W_N = 0.8$ μm. The other system parameters were taken as in Fig. 7(c).

[1] A. Y. Kitaev, Physics-uspekhi **44**, 131 (2001).
[2] A. Y. Kitaev, Annals of physics **303**, 2 (2003).
[3] X.-L. Qi and S.-C. Zhang, Reviews of Modern Physics **83**, 1057 (2011).
[4] M. Leijnse and K. Flensberg, Semiconductor Science and Technology **27**, 124003 (2012).
[5] C. Beenakker, Annu. Rev. Condens. Matter Phys. **4**, 113 (2013).
[6] R. Aguado, La Rivista del Nuovo Cimento **40**, 523 (2017).
[7] D. A. Ivanov, Physical review letters **86**, 268 (2001).
[8] C. Nayak, S. H. Simon, A. Stern, M. Freedman, and S. D. Sarma, Reviews of Modern Physics **80**, 1083 (2008).
[9] J. Alicea, Y. Oreg, G. Refael, F. Von Oppen, and M. P. Fisher, Nature Physics **7**, 412 (2011).
[10] D. Aasen, M. Hell, R. V. Mishmash, A. Higginbotham, J. Danon, M. Leijnse, T. S. Jespersen, J. A. Folk, C. M. Marcus, K. Flensberg, *et al.*, Physical Review X **6**, 031016 (2016).
[11] Y. Oreg, G. Refael, and F. von Oppen, Phys. Rev. Lett. **105**, 177002 (2010).
[12] J. D. Sau, S. Tewari, R. M. Lutchyn, T. D. Stanescu, and S. Das Sarma, Phys. Rev. B **82**, 214509 (2010).
[13] J. D. Sau, R. M. Lutchyn, S. Tewari, and S. Das Sarma, Phys. Rev. Lett. **104**, 040502 (2010).
[14] R. M. Lutchyn, J. D. Sau, and S. Das Sarma, Phys. Rev. Lett. **105**, 077001 (2010).
[15] L. P. Rokhinson, X. Liu, and J. K. Furdyna, Nature Physics **8**, 795 (2012).
[16] F. Pientka, G. Kells, A. Romito, P. W. Brouwer, and F. von Oppen, Phys. Rev. Lett. **109**, 227006 (2012).
[17] V. Mourik, K. Zuo, S. M. Frolov, S. Plissard, E. P. Bakkers, and L. P. Kouwenhoven, Science **336**, 1003 (2012).
[18] A. Das, Y. Ronen, Y. Most, Y. Oreg, M. Heiblum, and H. Shtrikman, Nature Physics **8**, 887 (2012).
[19] M. Deng, C. Yu, G. Huang, M. Larsson, P. Caroff, and H. Xu, Nano letters **12**, 6414 (2012).
[20] M. Deng, S. Vaitiekėnas, E. B. Hansen, J. Danon, M. Leijnse, K. Flensberg, J. Nygård, P. Krogstrup, and C. M. Marcus, Science **354**, 1557 (2016).
[21] S. Manna, P. Wei, Y. Xie, K. T. Law, P. A. Lee, and J. S. Moodera, Proceedings of the National Academy of Sciences **117**, 8775 (2020).
[22] J. Klinovaja, P. Stano, and D. Loss, Phys. Rev. Lett. **109**, 236801 (2012).
[23] M. Kjaergaard, K. Wölms, and K. Flensberg, Phys. Rev. B **85**, 020503 (2012).
[24] G. L. Fatin, A. Matos-Abiague, B. Scharf, and I. Žutić, Phys. Rev. Lett. **117**, 077002 (2016).
[25] A. Matos-Abiague, J. Shabani, A. D. Kent, G. L. Fatin, B. Scharf, and I. Žutić, Solid State Communications **262**, 1 (2017).
[26] N. Mohanta, T. Zhou, J.-W. Xu, J. E. Han, A. D. Kent, J. Shabani, I. Žutić, and A. Matos-Abiague, Phys. Rev. Appl. **12**, 034048 (2019).
[27] T. Zhou, N. Mohanta, J. E. Han, A. Matos-Abiague, and I. Žutić, Phys. Rev. B **99**, 134505 (2019).
[28] P. Marra and M. Cuoco, Phys. Rev. B **95**, 140504 (2017).
[29] M. Desjardins, L. Contamin, M. Delbecq, M. Dartiailh, L. Bruhat, T. Cubaynes, J. Viennot, F. Mallet, S. Rohart, A. Thiaville, *et al.*, Nature materials **18**, 1060 (2019).
[30] D. Steffensen, B. M. Andersen, and P. Kotetes, Phys. Rev. B **104**, 174502 (2021).
[31] P. Marra, Journal of Applied Physics **132**, 231101 (2022).
[32] U. Güngördü and A. A. Kovalev, Journal of Applied Physics **132**, 041101 (2022).
[33] T.-P. Choy, J. M. Edge, A. R. Akhmerov, and C. W. J. Beenakker, Phys. Rev. B **84**, 195442 (2011).
[34] I. Martin and A. F. Morpurgo, Phys. Rev. B **85**, 144505 (2012).
[35] F. Pientka, L. I. Glazman, and F. von Oppen, Phys. Rev. B **88**, 155420 (2013).
[36] S. Nadj-Perge, I. K. Drozdov, B. A. Bernevig, and A. Yazdani, Phys. Rev. B **88**, 020407 (2013).
[37] S. Nadj-Perge, I. K. Drozdov, J. Li, H. Chen, S. Jeon, J. Seo, A. H. MacDonald, B. A. Bernevig, and A. Yazdani, Science **346**, 602 (2014).
[38] R. Pawlak, M. Kisiel, J. Klinovaja, T. Meier, S. Kawai, T. Glatzel, D. Loss, and E. Meyer, npj Quantum Information **2**, 1 (2016).
[39] T. Kontos, M. Aprili, J. Lesueur, F. Genêt, B. Stephanidis, and R. Boursier, Phys. Rev. Lett. **89**, 137007 (2002).
[40] F. Pientka, A. Keselman, E. Berg, A. Yacoby, A. Stern, and B. I. Halperin, Phys. Rev. X **7**, 021032 (2017).
[41] D. Pekker, C.-Y. Hou, V. E. Manucharyan, and E. Demler, Phys. Rev. Lett. **111**, 107007 (2013).
[42] M. Hell, M. Leijnse, and K. Flensberg, Phys. Rev. Lett. **118**, 107701 (2017).
[43] F. Setiawan, A. Stern, and E. Berg, Phys. Rev. B **99**, 220506 (2019).
[44] F. Setiawan, C.-T. Wu, and K. Levin, Phys. Rev. B **99**, 174511 (2019).
[45] T. Yokoyama, M. Eto, and Y. V. Nazarov, Phys. Rev. B **89**, 195407 (2014).
[46] A. Fornieri, A. M. Whiticar, F. Setiawan, E. Portolés, A. C. Drachmann, A. Keselman, S. Gronin, C. Thomas, T. Wang, R. Kallaher, *et al.*, Nature **569**, 89 (2019).
[47] H. Ren, F. Pientka, S. Hart, A. T. Pierce, M. Kosowsky, L. Lunczer, R. Schlereth, B. Scharf, E. M. Hankiewicz, L. W. Molenkamp, *et al.*, Nature **569**, 93 (2019).
[48] M. C. Dartiailh, W. Mayer, J. Yuan, K. S. Wickramasinghe, A. Matos-Abiague, I. Žutić, and J. Shabani, Phys. Rev. Lett. **126**, 036802 (2021).
[49] S. Hart, H. Ren, T. Wagner, P. Leubner, M. Mühlbauer, C. Brüne, H. Buhmann, L. W. Molenkamp, and A. Yacoby, Nature Physics **10**, 638 (2014).
[50] T. Laeven, B. Nijholt, M. Wimmer, and A. R. Akhmerov, Phys. Rev. Lett. **125**, 086802 (2020).
[51] A. E. Svetogorov, D. Loss, and J. Klinovaja, Phys. Rev. B **103**, L180505 (2021).
[52] O. Lesser, A. Saydjari, M. Wesson, A. Yacoby, and Y. Oreg, Proceedings of the National Academy of Sciences **118**, e2107377118 (2021).
[53] T. Zhou, M. C. Dartiailh, K. Sardashti, J. E. Han, A. Matos-Abiague, J. Shabani, and I. Žutić, Nature Communications **13**, 1738 (2022).
[54] J. P. T. Stenger, M. Hatridge, S. M. Frolov, and D. Pekker, Phys. Rev. B **99**, 035307 (2019).
[55] J. Cayao, P. San-Jose, A. M. Black-Schaffer, R. Aguado, and E. Prada, Phys. Rev. B **96**, 205425 (2017).

[56] B. Scharf, F. Pientka, H. Ren, A. Yacoby, and E. M. Hankiewicz, Phys. Rev. B **99**, 214503 (2019).
[57] T. Zhou, M. C. Dartiailh, W. Mayer, J. E. Han, A. Matos-Abiague, J. Shabani, and I. Žutić, Phys. Rev. Lett. **124**, 137001 (2020).
[58] Y. Zhang, K. Guo, and J. Liu, Phys. Rev. B **102**, 245403 (2020).
[59] B. D. Woods and T. D. Stanescu, Phys. Rev. B **101**, 195435 (2020).
[60] P. P. Paudel, T. Cole, B. D. Woods, and T. D. Stanescu, Phys. Rev. B **104**, 155428 (2021).
[61] S. Salimian, M. Carrega, I. Verma, V. Zannier, M. P. Nowak, F. Beltram, L. Sorba, and S. Heun, Applied Physics Letters **119** (2021).
[62] F. Setiawan, W. S. Cole, J. D. Sau, and S. Das Sarma, Phys. Rev. B **95**, 174515 (2017).
[63] F. Setiawan and J. Hofmann, Phys. Rev. Res. **4**, 043087 (2022).
[64] A. Banerjee, O. Lesser, M. A. Rahman, H.-R. Wang, M.-R. Li, A. Kringhøj, A. M. Whiticar, A. C. C. Drachmann, C. Thomas, T. Wang, M. J. Manfra, E. Berg, Y. Oreg, A. Stern, and C. M. Marcus, Phys. Rev. B **107**, 245304 (2023).
[65] B. Pekerten, D. Brandão, B. H. Elfeky, T. Zhou, J. E. Han, J. Shabani, and I. Žutić, Phys. Rev. B **110**, L060513 (2024).
[66] B. Pekerten, D. S. Brandão, B. Bussiere, D. Monroe, T. Zhou, J. E. Han, J. Shabani, A. Matos-Abiague, and I. Žutić, Appl. Phys. Lett. **124**, 252602 (2024).
[67] J. D. Pakizer, B. Scharf, and A. Matos-Abiague, Phys. Rev. Res. **3**, 013198 (2021).
[68] B. Pekerten, J. D. Pakizer, B. Hawn, and A. Matos-Abiague, Phys. Rev. B **105**, 054504 (2022).
[69] Y. Tanaka and S. Kashiwaya, Phys. Rev. B **56**, 892 (1997).
[70] Y. Tanaka, Y. Mizuno, T. Yokoyama, K. Yada, and M. Sato, Phys. Rev. Lett. **105**, 097002 (2010).
[71] Y. A. Bychkov and E. I. Rashba, Journal of physics C: Solid state physics **17**, 6039 (1984).
[72] G. Dresselhaus, Physical Review **100**, 580 (1955).
[73] B. Scharf, F. Pientka, H. Ren, A. Yacoby, and E. M. Hankiewicz, Phys. Rev. B **99**, 214503 (2019).
[74] M. Luethi, K. Laubscher, S. Bosco, D. Loss, and J. Klinovaja, Phys. Rev. B **107**, 035435 (2023).
[75] J. D. Sau, R. M. Lutchyn, S. Tewari, and S. Das Sarma, Phys. Rev. Lett. **104**, 040502 (2010).
[76] Y. Nagae, A. P. Schnyder, Y. Tanaka, Y. Asano, and S. Ikegaya, Phys. Rev. B **110**, L041110 (2024).
[77] C.-T. Wu, B. M. Anderson, W.-H. Hsiao, and K. Levin, Physical Review B **95**, 014519 (2017).
[78] B. Lian, X.-Q. Sun, A. Vaezi, X.-L. Qi, and S.-C. Zhang, Proceedings of the National Academy of Sciences **115**, 10938 (2018).
[79] G. C. Ménard, A. Mesaros, C. Brun, F. Debontridder, D. Roditchev, P. Simon, and T. Cren, Nature communications **10**, 2587 (2019).
[80] C. W. J. Beenakker and D. Oriekhov, SciPost Physics (2020).
[81] X. Zhu, Phys. Rev. B **97**, 205134 (2018).
[82] L. Liu, C. Miao, H. Tang, Y.-T. Zhang, and Z. Qiao, Phys. Rev. B **109**, 115413 (2024).
[83] A. Winblad and H. Chen, Phys. Rev. B **109**, 205158 (2024).
[84] W. Mayer, M. C. Dartiailh, J. Yuan, K. S. Wickramasinghe, E. Rossi, and J. Shabani, Nature communications **11**, 212 (2020).
[85] A. P. Schnyder, S. Ryu, A. Furusaki, and A. W. Ludwig, Physical Review B **78**, 195125 (2008).
[86] S. Ryu, A. P. Schnyder, A. Furusaki, and A. W. Ludwig, New Journal of Physics **12**, 065010 (2010).
[87] P. Ghosh, J. D. Sau, S. Tewari, and S. D. Sarma, Physical Review B **82**, 184525 (2010).
[88] S. Tewari and J. D. Sau, Phys. Rev. Lett. **109**, 150408 (2012).
[89] M.-T. Rieder, P. W. Brouwer, and I. Adagideli, Physical Review B **88**, 060509 (2013).
[90] İ. Adagideli, M. Wimmer, and A. Teker, Physical Review B **89**, 144506 (2014).
[91] B. Pekerten, A. Teker, Ö. Bozat, M. Wimmer, and İ. Adagideli, Physical Review B **95**, 064507 (2017).
[92] T. D. Stanescu, R. M. Lutchyn, and S. D. Sarma, Physical Review B **84**, 144522 (2011).
[93] T. D. Stanescu and S. Tewari, Journal of Physics: Condensed Matter **25**, 233201 (2013).
[94] B. Pekerten, A. M. Bozkurt, and İ. Adagideli, Physical Review B **100**, 235455 (2019).
[95] A. Daido and Y. Yanase, Phys. Rev. B **95**, 134507 (2017).
[96] C. W. Groth, M. Wimmer, A. R. Akhmerov, and X. Waintal, New Journal of Physics **16**, 063065 (2014).

Chapter 5

Conclusions

This thesis contributes to the theoretical understanding and identification of robust signatures of Majorana Zero Modes (MZMs), a key pursuit in the advancement of topological quantum computing. Through three independent yet thematically connected investigations, we explored novel quantum transport and localization phenomena in systems involving topological superconductors.

In the first study, we demonstrated that the interplay between MZMs and Bound States in the Continuum (BICs) in a double quantum dot (DQD) system leads to tunable interference effects, with the magnetic flux acting as a control parameter. The appearance of conductance suppression and leakage of MZMs into the quantum dots highlights the potential for manipulating such states with external magnetic fields.

In the second work, we showed that thermoelectric properties of systems hosting MZMs can be significantly enhanced by exploiting the BIC to quasi-BIC transition driven by magnetic flux. The modulation of the Seebeck coefficient and figure of merit points to a promising route for detecting MZMs.

In the final study, we introduced a quantitative descriptor—the topological gap character—for distinguishing between edge-like and end-like Majorana states in planar Josephson junctions. By analyzing its dependence on physical parameters such as magnetic field and superconducting phase difference, we identified strategies to induce controlled transitions between different localization regimes. This provides valuable insights for improving the stability and manipulation of MZMs, with direct implications for scalable braiding operations.

Altogether, these results offer new pathways for engineering and controlling MZMs via interference, and external parameters, and may serve as theoretical foundations for future experimental realizations and topological qubit design.

Appendix A

Numerical methods for TS in JJs

Solving the BdG-Hamiltonian for JJs requires numerical methods. While semi-analytical solutions exist in limited cases (such as under the Dirac-delta approximation for infinitely narrow junctions) these approaches are restrictive and fail to capture general physical effects. We therefore employ numerical techniques to compute the eigenvalues and eigenstates of the BdG Hamiltonian.

A.1 Finite-Difference Method

Our numerical approach uses the finite-difference method, where the system is discretized on a square lattice. In this framework, derivatives are approximated as,

$$\frac{df(x)}{dx} \approx \frac{f(x+a)-f(x-a)}{2a}, \tag{A.1}$$

$$\frac{d^2f(x)}{dx^2} \approx \frac{f(x+a)+f(x-a)-2f(x)}{a^2}, \tag{A.2}$$

where $f(x)$ is an arbitrary function and a is the lattice spacing. These approximations converge to the true derivatives as $a \to 0$, allowing us to transform differential equations into algebraic systems.

A.2 Tight-Binding Approximation

We represent the system using discretized position states $|x,y\rangle = |a_i, a_j\rangle$, where i, j are index lattice sites and a is the lattice constant. Within the tight-binding approximation, the momentum operator and kinetic energy take the form:

$$\hat{p}_x|x,y\rangle = -i\frac{\partial}{\partial x}|x,y\rangle \approx -i\frac{|x+a,y\rangle - |x-a,y\rangle}{2a}, \tag{A.3}$$

$$\hat{p}_x^2|x,y\rangle = -\frac{\partial^2}{\partial x^2}|x,y\rangle \approx \frac{-|x+a,y\rangle - |x-a,y\rangle + 2|x,y\rangle}{a^2}. \tag{A.4}$$

The corresponding y-components $\hat{p}_y$ and $\hat{p}_y^2$ follow analogously from Eqs. (A.3) and (A.4). These relations enable construction of a tight-binding representation of the BdG Hamiltonian, which we diagonalize numerically. The resulting matrix Hamiltonian has dimension $4N$, accounting for four orbitals per site (electron spin up/down and hole spin up/down).

For implementation, we use the Python package Kwant [80], which provides efficient tools for building and diagonalizing tight-binding models in quantum transport calculations.

References

[1] P. Zhou, "Research: Topological quantum computing, https://www.zhouphy.com/index.php/research/," (2023).

[2] V. Mourik, K. Zuo, S. M. Frolov, S. Plissard, E. P. Bakkers, and L. P. Kouwenhoven, Science **336**, 1003 (2012).

[3] H. Ren, F. Pientka, S. Hart, A. T. Pierce, M. Kosowsky, L. Lunczer, R. Schlereth, B. Scharf, E. M. Hankiewicz, L. W. Molenkamp, *et al.*, Nature **569**, 93 (2019).

[4] Advanced Science News, "Topological phase transitions and the 2016 Nobel Prize in Physics," (2016).

[5] R. Aguado, La Rivista del Nuovo Cimento **40**, 523 (2017).

[6] C. W. Hsu, B. Zhen, A. D. Stone, J. D. Joannopoulos, and M. Soljačić, Nat. Rev. Mater. **1**, 1 (2016).

[7] B. Kubala and J. König, Phys. Rev. B **65**, 245301 (2002).

[8] C.-K. Chiu, J. C. Y. Teo, A. P. Schnyder, and S. Ryu, Rev. Mod. Phys. **88**, 035005 (2016).

[9] A. Y. Kitaev, Phys.-Usp. **44**, 131 (2001).

[10] J. Alicea, Rep. Prog. Phys. **75**, 076501 (2012).

[11] M. Leijnse and K. Flensberg, Semiconductor Science and Technology **27**, 124003 (2012).

[12] C. W. J. Beenakker, Annu. Rev. Condens. Matter Phys. **4**, 113 (2013).

[13] D. A. Ivanov, Phys. Rev. Lett. **86**, 268 (2001).

[14] J. Alicea, Physical Review B—Condensed Matter and Materials Physics **81**, 125318 (2010).

[15] T. D. Stanescu, R. M. Lutchyn, and S. D. Sarma, Phys. Rev. B **84**, 144522 (2011).

[16] M. Aghaee, A. Akkala, Z. Alam, R. Ali, A. Alcaraz Ramirez, M. Andrzejczuk, A. E. Antipov, P. Aseev, M. Astafev, B. Bauer, *et al.*, Physical Review B **107**, 245423 (2023).

[17] E. Stoudenmire, J. Alicea, O. A. Starykh, and M. P. Fisher, Physical Review B—Condensed Matter and Materials Physics **84**, 014503 (2011).

[18] J. Alicea, Y. Oreg, G. Refael, F. Von Oppen, and M. Fisher, Nat. Phys. **7**, 412 (2011).

[19] B. I. Halperin, Y. Oreg, A. Stern, G. Refael, J. Alicea, and F. von Oppen, Physical Review B—Condensed Matter and Materials Physics **85**, 144501 (2012).

[20] D. Aasen, M. Aghaee, Z. Alam, M. Andrzejczuk, A. Antipov, M. Astafev, L. Avilovas, A. Barzegar, B. Bauer, J. Becker, *et al.*, arXiv preprint arXiv:2502.12252 (2025).

[21] L. Fu and C. L. Kane, Phys. Rev. Lett. **100**, 096407 (2008).

[22] J. D. Sau, R. M. Lutchyn, S. Tewari, and S. Das Sarma, Phys. Rev. Lett. **104**, 040502 (2010).

[23] F. Pientka, A. Keselman, E. Berg, A. Yacoby, A. Stern, and B. I. Halperin, Phys. Rev. X **7**, 021032 (2017).

[24] G. L. Fatin, A. Matos-Abiague, B. Scharf, and I. Žutić, Phys. Rev. Lett. **117**, 077002 (2016).

[25] A. Matos-Abiague, J. Shabani, A. D. Kent, G. L. Fatin, B. Scharf, and I. Žutić, Solid State Communications **262**, 1 (2017).

[26] T. Zhou, N. Mohanta, J. E. Han, A. Matos-Abiague, and I. Žutić, Phys. Rev. B **99**, 134505 (2019).

[27] M. Hell, M. Leijnse, and K. Flensberg, Phys. Rev. Lett. **118**, 107701 (2017).

[28] T. Zhou, M. C. Dartiailh, W. Mayer, J. E. Han, A. Matos-Abiague, J. Shabani, and I. Žutić, Phys. Rev. Lett. **124**, 137001 (2020).

[29] M. C. Dartiailh, W. Mayer, J. Yuan, K. S. Wickramasinghe, A. Matos-Abiague, I. Žutić, and J. Shabani, Phys. Rev. Lett. **126**, 036802 (2021).

[30] L. W. Molenkamp, T. Gravier, H. van Houten, O. J. A. Buijk, M. A. A. Mabesoone, and C. T. Foxon, Phys. Rev. Lett. **68**, 3765 (1992).

[31] H. van Houten, L. W. Molenkamp, C. W. J. Beenakker, and C. T. Foxon, Semiconductor Science and Technology **7**, B215 (1992).

[32] A. G. Bauer, B. Scharf, L. W. Molenkamp, E. M. Hankiewicz, and B. Sothmann, Phys. Rev. B **104**, L201410 (2021).

[33] P. E. Dolgirev, M. S. Kalenkov, and A. D. Zaikin, physica status solidi (RRL)–Rapid Research Letters **13**, 1800252 (2019).

[34] C.-Y. Hou, K. Shtengel, and G. Refael, Phys. Rev. B **88**, 075304 (2013).

[35] E. Sela, Y. Oreg, S. Plugge, N. Hartman, S. Lüscher, and J. Folk, Phys. Rev. Lett. **123**, 147702 (2019).

[36] D. Giuliano, A. Nava, R. Egger, P. Sodano, and F. Buccheri, Phys. Rev. B **105**, 035419 (2022).

[37] F. Buccheri, A. Nava, R. Egger, P. Sodano, and D. Giuliano, Phys. Rev. B **105**, L081403 (2022).

[38] C. Benjamin and R. Das, Europhysics Letters **146**, 16006 (2024).

[39] K. Von Klitzing, Reviews of Modern Physics **58**, 519 (1986).

[40] J. von Neumann and E. P. Wigner, Z. Phys. **30**, 465 (1929).

[41] J. P. Ramos and P. A. Orellana, Phys. B: Condens. Matter **455**, 66 (2014).

[42] B. Grez, J. Ramos-Andrade, V. Juričić, and P. Orellana, Phys. Rev. A **106**, 013719 (2022).

[43] W. G. Van der Wiel, S. De Franceschi, J. M. Elzerman, T. Fujisawa, S. Tarucha, and L. P. Kouwenhoven, Rev. Mod. Phys. **75**, 1 (2002).

[44] R. Hanson, L. P. Kouwenhoven, J. R. Petta, S. Tarucha, and L. M. Vandersypen, Rev. Mod. Phys. **79**, 1217 (2007).

[45] A. Holleitner, C. Decker, H. Qin, K. Eberl, and R. Blick, Phys. Rev. Lett. **87**, 256802 (2001).

[46] A. W. Holleitner, R. H. Blick, A. K. Huttel, K. Eberl, and J. P. Kotthaus, Science **297**, 70 (2002).

[47] W. Z. Shangguan, T. C. A. Yeung, Y. B. Yu, and C. H. Kam, Phys. Rev. B **63**, 235323 (2001).

[48] P. A. Orellana, F. Dominguez-Adame, I. Gómez, and M. L. L. De Guevara, Phys. Rev. B **67**, 085321 (2003).

[49] A. Das, Y. Ronen, Y. Most, Y. Oreg, M. Heiblum, and H. Shtrikman, Nat. Phys. **8**, 887 (2012).

[50] W. Hofstetter, J. König, and H. Schoeller, Phys. Rev. Lett. **87**, 156803 (2001).

[51] G. Górski and K. Kucab, Phys. Status Solidi B **256**, 1800492 (2019).

[52] F. Chi, J.-L. Liu, and L.-L. Sun, J. Appl. Phys **101**, 093704 (2007).

[53] U. Fano, Phys. Rev. **124**, 1866 (1961).

[54] A. E. Miroshnichenko, S. Flach, and Y. S. Kivshar, Rev. Mod. Phys. **82**, 2257 (2010).

[55] M. L. Ladrón de Guevara, F. Claro, and P. A. Orellana, Phys. Rev. B **67**, 195335 (2003).

[56] F. Chi, J. Wang, T.-Y. He, Z.-G. Fu, P. Zhang, X.-W. Zhang, L. Wang, and Z. Lu, Front. Phys. **8**, 631031 (2021).

[57] T. Kontos, M. Aprili, J. Lesueur, F. Genêt, B. Stephanidis, and R. Boursier, Phys. Rev. Lett. **89**, 137007 (2002).

[58] D. Pekker, C.-Y. Hou, V. E. Manucharyan, and E. Demler, Phys. Rev. Lett. **111**, 107007 (2013).

[59] F. Setiawan, A. Stern, and E. Berg, Phys. Rev. B **99**, 220506 (2019).

[60] F. Setiawan, C.-T. Wu, and K. Levin, Phys. Rev. B **99**, 174511 (2019).

[61] T. Yokoyama, M. Eto, and Y. V. Nazarov, Phys. Rev. B **89**, 195407 (2014).

[62] A. Fornieri, A. M. Whiticar, F. Setiawan, E. Portolés, A. C. Drachmann, A. Keselman, S. Gronin, C. Thomas, T. Wang, R. Kallaher, *et al.*, Nature **569**, 89 (2019).

[63] S. Hart, H. Ren, T. Wagner, P. Leubner, M. Mühlbauer, C. Brüne, H. Buhmann, L. W. Molenkamp, and A. Yacoby, Nature Physics **10**, 638 (2014).

[64] T. Laeven, B. Nijholt, M. Wimmer, and A. R. Akhmerov, Phys. Rev. Lett. **125**, 086802 (2020).

[65] A. E. Svetogorov, D. Loss, and J. Klinovaja, Phys. Rev. B **103**, L180505 (2021).

[66] O. Lesser, A. Saydjari, M. Wesson, A. Yacoby, and Y. Oreg, Proceedings of the National Academy of Sciences **118**, e2107377118 (2021).

[67] T. Zhou, M. C. Dartiailh, K. Sardashti, J. E. Han, A. Matos-Abiague, J. Shabani, and I. Žutić, Nature Communications **13**, 1738 (2022).

[68] J. P. T. Stenger, M. Hatridge, S. M. Frolov, and D. Pekker, Phys. Rev. B **99**, 035307 (2019).

[69] J. Cayao, P. San-Jose, A. M. Black-Schaffer, R. Aguado, and E. Prada, Phys. Rev. B **96**, 205425 (2017).

[70] B. Scharf, F. Pientka, H. Ren, A. Yacoby, and E. M. Hankiewicz, Phys. Rev. B **99**, 214503 (2019).

[71] Y. Zhang, K. Guo, and J. Liu, Phys. Rev. B **102**, 245403 (2020).

[72] B. D. Woods and T. D. Stanescu, Phys. Rev. B **101**, 195435 (2020).

[73] P. P. Paudel, T. Cole, B. D. Woods, and T. D. Stanescu, Phys. Rev. B **104**, 155428 (2021).

[74] S. Salimian, M. Carrega, I. Verma, V. Zannier, M. P. Nowak, F. Beltram, L. Sorba, and S. Heun, Applied Physics Letters **119** (2021).

[75] F. Setiawan, W. S. Cole, J. D. Sau, and S. Das Sarma, Phys. Rev. B **95**, 174515 (2017).

[76] F. Setiawan and J. Hofmann, Phys. Rev. Res. **4**, 043087 (2022).

[77] A. Banerjee, O. Lesser, M. A. Rahman, H.-R. Wang, M.-R. Li, A. Kringhøj, A. M. Whiticar, A. C. C. Drachmann, C. Thomas, T. Wang, M. J. Manfra, E. Berg, Y. Oreg, A. Stern, and C. M. Marcus, Phys. Rev. B **107**, 245304 (2023).

[78] B. Pekerten, D. Brandão, B. H. Elfeky, T. Zhou, J. E. Han, J. Shabani, and I. Žutić, Phys. Rev. B **110**, L060513 (2024).

[79] B. Pekerten, D. S. Brandão, B. Bussiere, D. Monroe, T. Zhou, J. E. Han, J. Shabani, A. Matos-Abiague, and I. Žutić, Appl. Phys. Lett. **124**, 252602 (2024).

[80] C. W. Groth, M. Wimmer, A. R. Akhmerov, and X. Waintal, New Journal of Physics **16**, 063065 (2014).